Rochester Institute of Technology

## RIT Digital Institutional Repository

5-2015

# Aluminum Nitride Contour Mode Resonators

Joshua Robert Melnick

Aluminum Nitride Contour Mode Resonators
by
Joshua Robert Melnick


A Thesis Submitted

in

Partial Fulfillment

of the

Requirements for the Degree of

MASTER OF SCIENCE

in Microelectronic Engineering


DEPARTMENT OF ELECTRICAL AND MICROELECTRONIC ENGINEERING
KATE GLEASON COLLEGE OF ENGINEERING
ROCHESTER INSTITUTE OF TECHNOLOGY
ROCHESTER, NEW YORK
MAY, 2015

# Aluminum Nitride Contour Mode Resonators

by

Joshua Robert Melnick

A Thesis Submitted
in
Partial Fulfillment
of the
Requirements for the Degree of
MASTER OF SCIENCE
in Microelectronic Engineering
Approved by:

PROF: _____
      Dr. Ivan Puchades (Thesis Advisor)


PROF: _____
      Dr. Lynn Fuller (Thesis Committee Member)


PROF: _____
      Dr. Michael Jackson (Thesis Committee Member)


PROF: _____
      Dr. Robert Pearson
(Microelectronic Engineering Program Director)


PROF: _____
      Dr. Sohail Dianat (Department Head)


DEPARTMENT OF ELECTRICAL AND MICROELECTRONIC ENGINEERING
COLLEGE OF ENGINEERING
ROCHESTER INSTITUTE OF TECHNOLOGY
ROCHESTER, NEW YORK
MAY, 2015

**Abstract**

Resonators are a major component in RF electronic products. They are used in a host of ways to filter radio signals.Modern and Future RF communications have placed high demands on the industry; requiring low power usage, wide array of applications and resistance to noise.

In this thesis, a discussion of the motivation for RF MEMS filters and basic theory is given with an explanation of the concepts of Q factor, piezoelectricity, acoustics theory, the major types of resonators (SAW, BAW, CMR or LAMB), apodization theory and techniques as well as design, simulation of CMR and BAW devices, testing and process development of aluminum nitride by RF reactive sputtering at RIT.

Finite element analysis was performed on a number of factors of aluminum nitride contour mode resonators (CMR) from piezoelectric film thickness, to electrode pitch, electrode thickness and electrode configuration; to understand the effects. First order and second order vibration modes were seen including symmetric $S_0$, $S_1$ and antisymmetric $A_0$, $A_1$ resonant modes in the pizeoacoustic devices and higher. A series of time dependent video simulations of SAW, BAW and LAMB wave resonators were also performed, perhaps the first of their kind.

The RF reactive sputtering deposition for aluminum nitride was developed at RIT by a fractional factorial experiment with the factors being RF power, nitrogen to argon flow rate ratios, changing the distance of the wafer to the platen from 5 to 4 cm, use of a aluminum, molybdenum or virgin silicon seed layer and chamber pressure. In nearly all cases it was found that an RF power of 1000W is the most important factor contributing to the $\langle 002 \rangle$ orientation. The decreasing of the target distance may inhibit a reaction mechanisms in the plasma resulting in a more amorphous deposition. It may be due to the increase in temperature resulting from the higher RF power that promotes the growth of $\langle 002 \rangle$ oriented aluminum nitride. A molybdenum seed layer tends to have a stronger $\langle 002 \rangle$ peak relative to aluminum and a chamber pressure of 3mT was found to exhibit a deposition that most favors the $\langle 002 \rangle$ oriented aluminum nitride.

It was found that molybdenum is not consumed in a wet etch of KOH. Molybdenum is oxidized during photo resist ashing. The Contact Vias were necessarily over retched in order to ensure complete removal of Al-N over the Bottom Electrode.

C-V measurements were done on the aluminum nitride to determine its quality, the measured extensional piezoelectric coefficient $d_{33}$ is -0.000108716 $\frac{nm}{V}$, which is -0.108716 $\frac{pm}{V}$ lower than 8pm/V typically reported. The lower piezo electric coefficient measured as compared with typical values, may be due to low film density a result of the high power used in the RF reactive sputtering that was used to heat the platen to a high enough temperature to promote the $\langle 002 \rangle$ oriented growth of AlN.

A series of iterations were designed and S11 frequency response measured. The electrode overlap from 25 to 50 to 75 $\mu$m,it does not appear to have an effect on the resonant frequency, but does increase the amplitude of the response at that die's given frequency. Increasing the anchor width from 5$\mu$m to 10$\mu$m to 20$\mu$m lowers the relative amplitude of the response therefore lowering the Q of the resonator. It may be that the increasingly wide anchor, increases the mechanical resistances within the device and thereby lowers the Q factor of the resonator. Increasing the number of electrodes increases the relative amplitude of the response. Increasing pitch from 5$\mu$m to 6$\mu$m seems to have a small effect on the resonant frequency of the devices, shifting them from 4.57 to 4.59 GHz. A quality factor was measured, with an anchor width of 5$\mu$m, pitch of 5$\mu$m, 24 electrodes and an electrode overlap of 75$\mu$m had a measured Q value of 98.8.

Dedicated To My Father:
Robert Russell Melnick
May 5, 1956 - October 19, 2014

# Acknowledgments

Above all I would like to thank my advisor Dr. Ivan Puchades, for all of his help and limitless patience.

<div align="center">

Advising Committee
Dr. Ivan Puchades
Dr. Michael Jackson
Dr. Lynn Fuller

---

Dr. Surendra K Gupta
Mr. Mustafa Koz
Dr. Stefan Preble
Dr. Abdelsalam Aboketaf
SMFL Staff

</div>

# Contents

# List of Figures

# List of Tables

# Chapter 1

# Introduction

The general secular trend of Western Civilization is the tendency towards increasing interconnectivity of all forms of transportation, electronics and dwellings into a single gigantic, technological colossus, as illustrated in Figure 1. The total mobilization of information and communication throughout life [11–13] where everything, connects with everything; anywhere and at anytime.
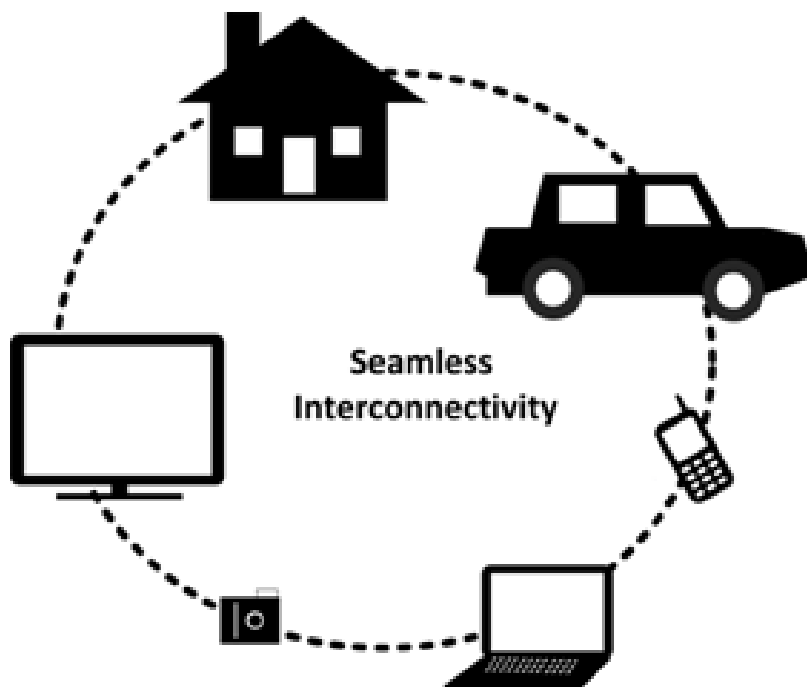


Figure 1.1: **Omni-present interconnectivity**

The tendency towards interconnectivity presents new challenges that must be overcome in order for the trend to be fulfilled. The dilemma of increasing interconnectivity is that the number of devices being used is tending upwards where as the usable Radio Frequency Spectrum available is finite [1,14,15] (Figure 1.2).

This trend calls for ever more refined and delicate means of using the limited space of the electromagnetic spectrum (1) as well as reducing the size, weight, cost and energy consumption of those very devices [3],where on the one hand the filters must be more selective and yet on the other should also be reduced in size, weight, cost, etc (Figure 1). This forces modernity to use new and creative solutions to achieve the contradictory goal.
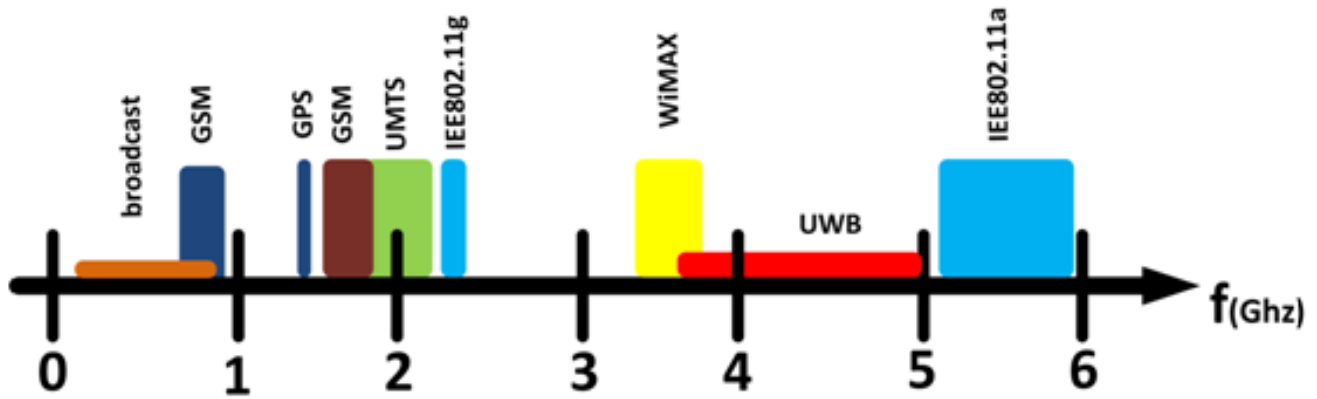
Figure 1.2: **Crowded RF Spectrum**
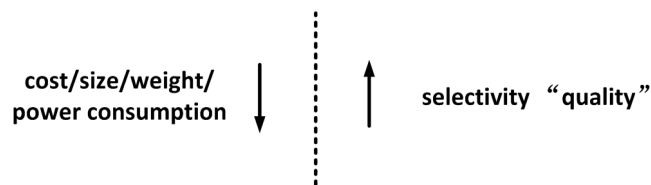


Figure 1.3: **Future needs of wireless technology**

It is the intention of this paper to be a contribution to solving the aforementioned problem. The paper will begin with basic theory of filtering, its means and methods, the design and fabrication of RF MEMS piezo-acoustic devices and a technique called "apodization" that reduces unwanted spurious modes in the resonators.The devices in the following thesis were designed based on acoustic theory, that will be discussed in this thesis as well as the critically important aluminum nitride deposition and thickness, along with the process flow for the resonators, fabrication and measurement.

According to Yole Development [1] Figure 1.4, interest in RF MEMS is increasing and is set to expand rapidly as the number of wireless devices and sensors becomes more ubiquitous. The market for home automation, high speed wireless internet and other telecom solutions can only lead to a greater demand for these devices.

**2011-2017 Yole MEMS Markets Forecast**

March 2012 Update

US$M

| | 2010 | 2011 | 2012 | 2013 | 2014 | 2015 | 2016 | 2017 |
|---|---|---|---|---|---|---|---|---|
| Others (microstructures, micro tips, flow meter ...) | $198 | $247 | $306 | $379 | $474 | $641 | $782 | $991 |
| Oscillators | $12 | $24 | $48 | $88 | $168 | $272 | $367 | $463 |
| RF MEMS | $359 | $419 | $469 | $527 | $627 | $762 | $887 | $1 028 |
| Microfluidics | $1 154 | $1 444 | $1 818 | $2 005 | $2 513 | $3 118 | $3 893 | $4 794 |
| Optical MEMS | $965 | $1 061 | $1 161 | $1 319 | $1 503 | $1 757 | $2 094 | $2 555 |
| Micro displays | $0 | $5 | $12 | $27 | $63 | $108 | $162 | $261 |
| Uncooled IR | $303 | $351 | $379 | $405 | $465 | $542 | $645 | $652 |
| Combos | $36 | $77 | $235 | $461 | $743 | $1 092 | $1 350 | $1 693 |
| Compasses | $239 | $364 | $448 | $498 | $502 | $485 | $458 | $448 |
| Gyroscopes | $1 006 | $1 287 | $1 499 | $1 634 | $1 708 | $1 615 | $1 545 | $1 468 |
| Accelerometers | $1 411 | $1 520 | $1 571 | $1 600 | $1 621 | $1 609 | $1 593 | $1 564 |
| Microphones | $322 | $436 | $509 | $589 | $659 | $704 | $752 | $835 |
| Pressure Sensors | $1 355 | $1 406 | $1 505 | $1 642 | $1 761 | $1 848 | $2 015 | $2 240 |
| InkJet Heads | $1 567 | $1 477 | $1 449 | $1 514 | $1 740 | $1 799 | $1 862 | $1 939 |

Figure 1.4: **Market Trends as predicted by Yole in their press release** [1]

# Chapter 2

# Theory

Modern technology is increasingly using electromagnetic waves to intercommunicate. In the world around us however, there are random waves (noise) as well as other frequencies being used for communication. This creates a need for a managed use of the electromagnetic spectrum for greater exploitation, which necessitates the use of filters (Figure 2.1) [16,17], to filter the electromagnetic waves so that only the ones selected for transmission of information are amplified and used.

To understand filters, we must first understand the concept of resonance. Nearly all objects when struck, hit, plucked, or otherwise excited will vibrate at their Natural Frequency. When a ruler is dropped, it will oscillate at its natural frequency. When a guitar string is plucked that string will oscillate at its natural frequency. When a pendulum is pulled to one side and released it will tend to oscillate at its resonant frequency or frequencies, this is useful, because some types of resonators will oscillate more strongly at a particular frequency, or range of frequencies over others, this can be used to filter signals. In the case of RF MEMS, electrical signals are used as the input signal, transduced into acoustic, or mechanical waves and then transduced back into electrical waves or signals, some frequencies experience much less attenuation than others.



**RF Filter**

$f_o =$

**RF Signal**

**Filtered RF Signal**
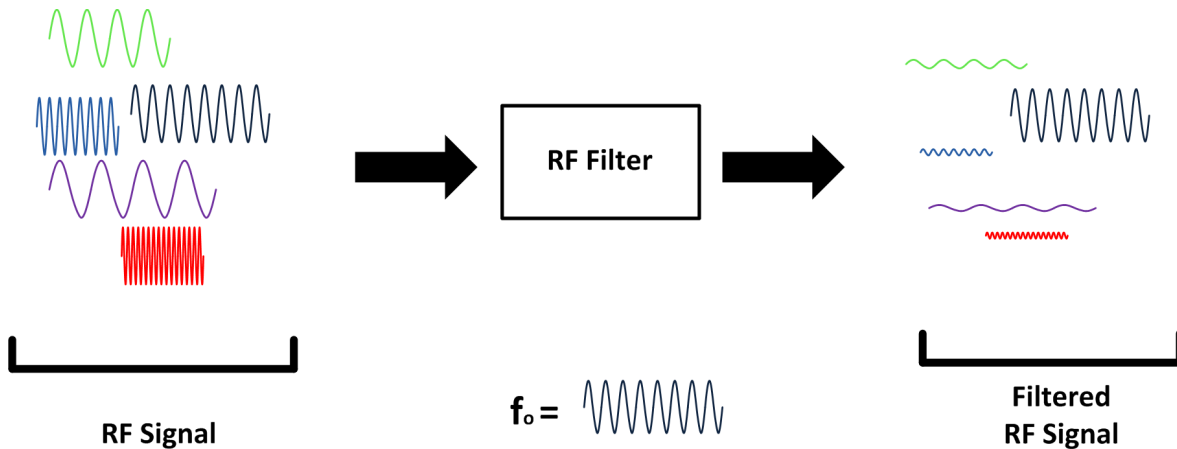
Figure 2.1:  **diagram of RF filter concept**

## 2.1   Pendulums and Oscillators

When a system like a pendulum is excited it will start to oscillate, now imagine if that force is periodic as in Figure 5. The frequency of the periodic force doesn't have to be the same as the natural frequency of the system. If the frequency of the force is not the same as the system the external force

will try to force the system to oscillate at its frequency, but this will cause an uneven pattern of vibration with the canceling out of some of the motion [4-5]. Some of the energy is absorbed by the system. In the case of a periodic force with a frequency equal to the natural frequency of the system, resonance will be achieved, thus the system will freely swing with a maximum amplitude.

## At Rest
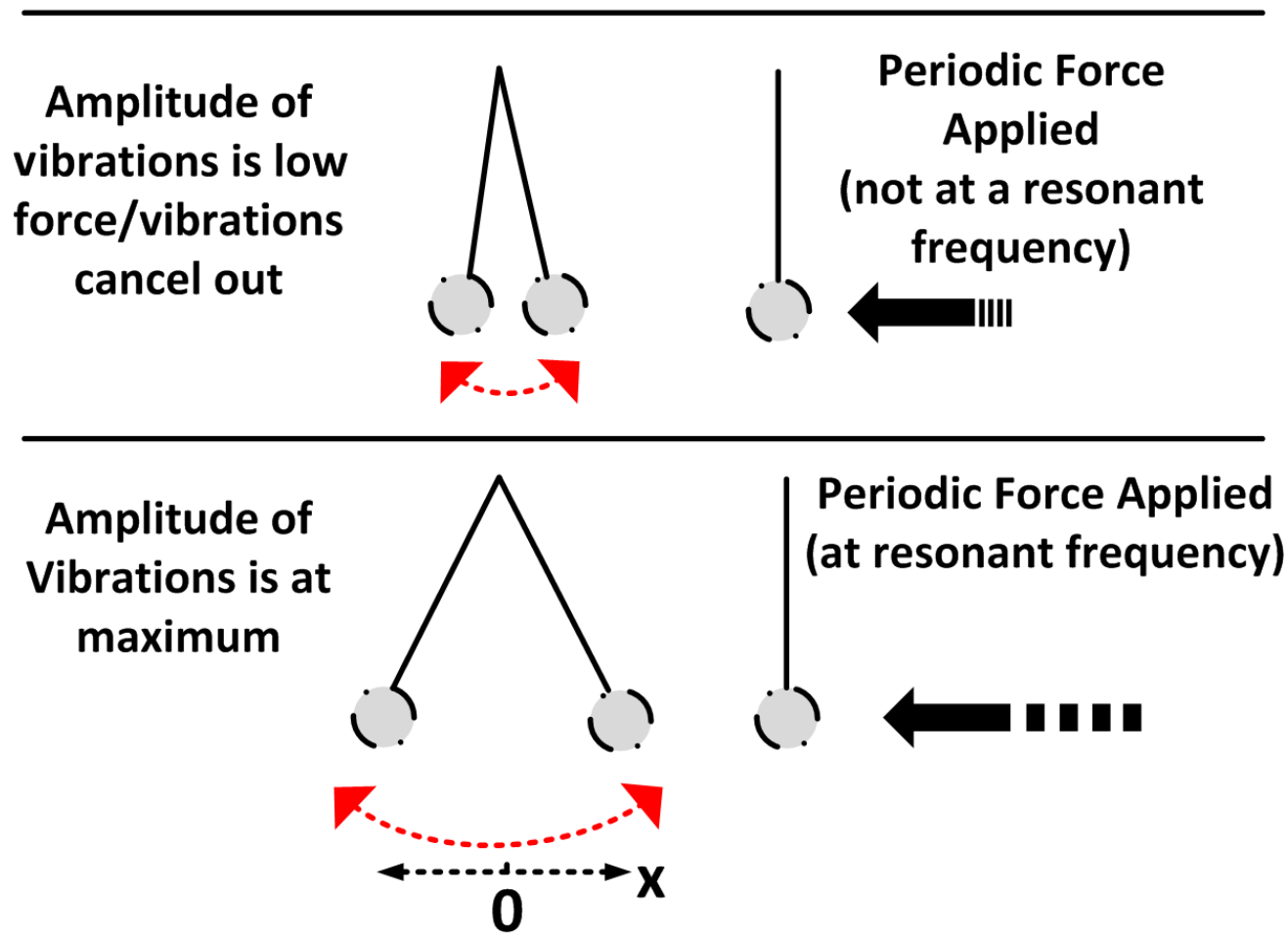


Figure 2.2: **Principles of Resonance, Q and oscillators**

## 2.2 Q and Oscillators

Oscillators can be described in terms of their quality. A quality factor Q, is a figure of merit for comparing oscillators. Q is a measure of the decay time (i.e. ring time) in radians. The quality factor, Q is proportional to the decay time of the oscillations before the system energy is reduced by a large amount,for example in Figure 2.3 a pendulum with a Q of 1000 would take as many cycles to lose $e^{2\pi}$ (Euler's number) amount of energy in the system. The time in which a resonator loses its energy is dependent on something called drag, or in other systems may be called resistance. In extremely
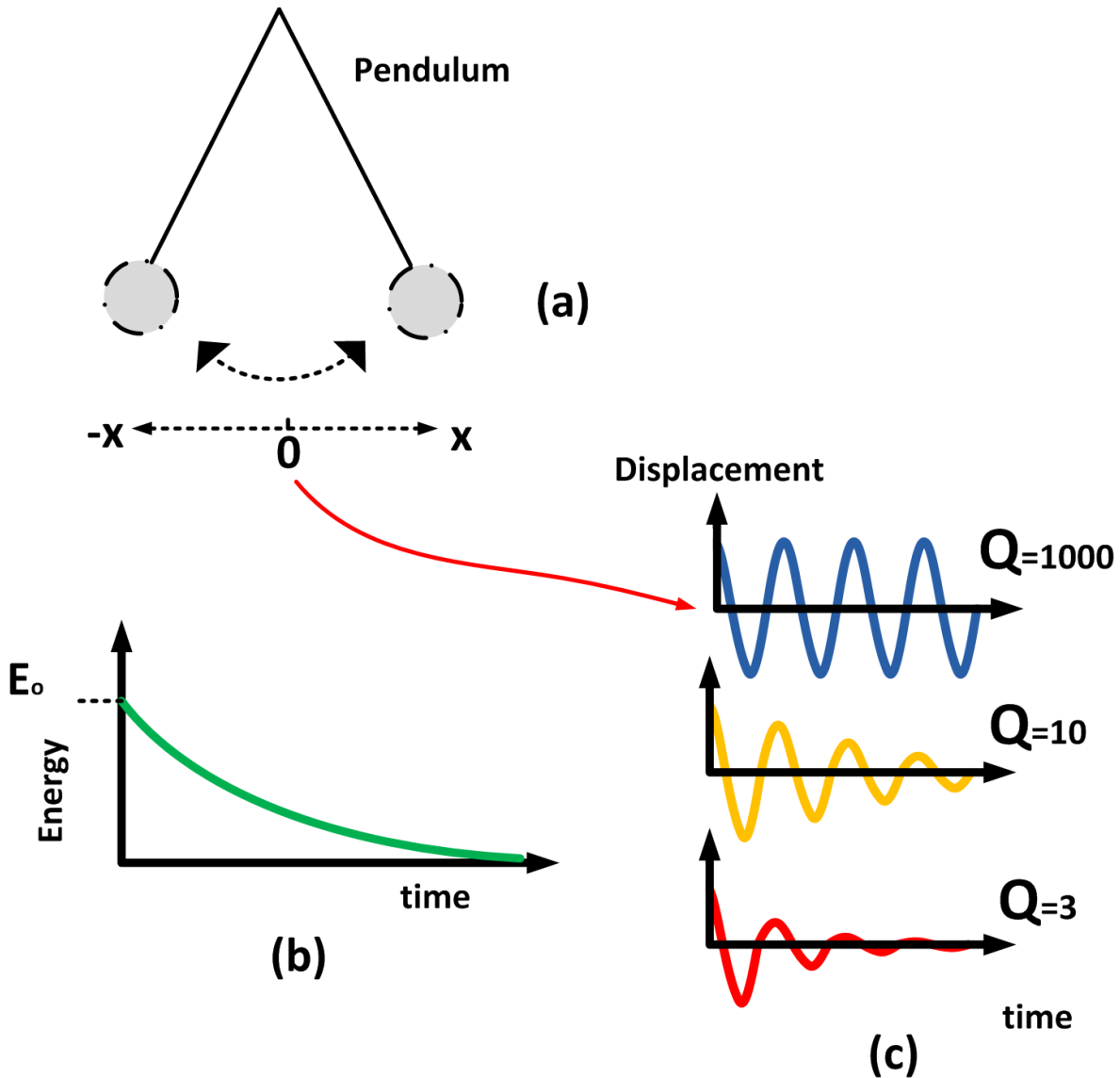


Figure 2.3: **Quality Factor in Resonant Systems**

demanding environments where the space for using frequencies is critical this becomes very important. Resonators can be used to filter incoming RF signals, the higher the quality of a filter, the more selective it is in terms of the frequencies that will excite it into its resonant state. The higher the Q, the smaller is the bandwidth. The bandwidth of a resonator determines what range of frequencies will energize it. The smaller the bandwidth, the more devices that can be squeezed into the same amount of RF spectrum real-estate, this decrease in range can be seen in Figure 2.4. In signal processing, which is
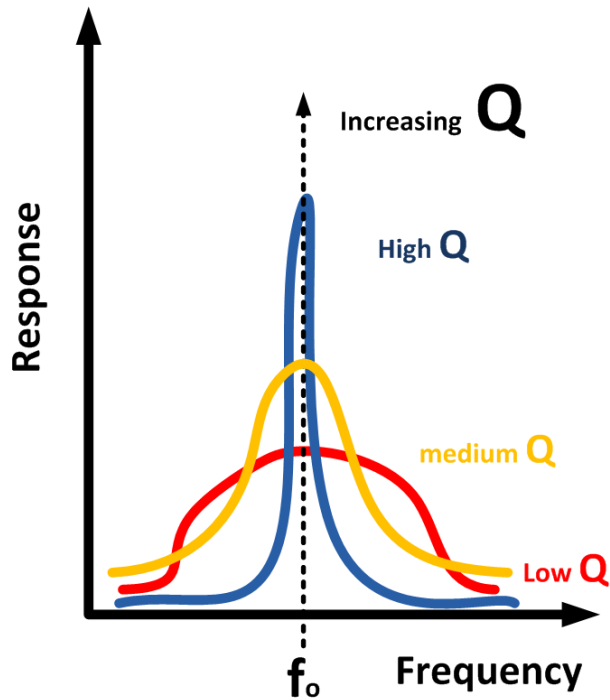
Figure 2.4: **Comparison of Different Q's**

what we are concerned with, the bandwidth is the boundary of a system's frequency response. The cutoff frequency, in electronics, is the frequency above or below the central passband frequency that is one half of the power.

In deciBels this is equivalent to -3dB and is depicted in Figure 2.5. The purpose of the RF MEMS devices is to filter radio waves, to attenuate frequencies of light that we do not need relative to the target frequencies that are being used to send some intelligent signal across the RF spectrum. All around us, as shown in Figure 2.1 is an endless number of frequency of light, we must filter the signals that hit the antenna of a cell phone, radio or WiFi system so that the information can be used.
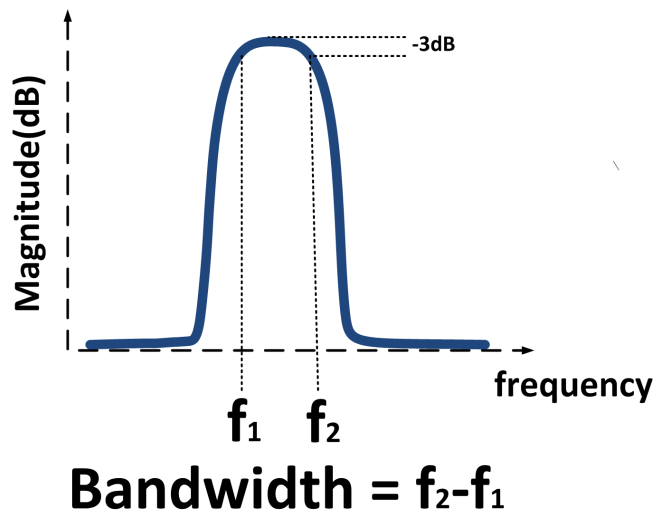


Figure 2.5: **Bandwith Explanation**

In the context of electronics, RF MEMS has the best range of attributes for future electronics devel-

opment (Figure 2.6).The table shows a progression in size and Q factor with differing technologies.The type of resonator, Q value, size and power consumption are compared. With the advent of hand held devices and increasing demand for ever smaller sizes RF MEMS has the best grouping of attributes. When filtering with RLC filters, the off chip inductors will consume a large amount of power, which is unacceptable as well as take up a large amount of room inside the device. On chip spiral inductors, which are made via micro-electronic techniques on the chip itself are not capable of producing large inductance values. RF MEMS using piezo-acoustic techniques have the best possible grouping of attributes for future technological development as well as the possibility of being fabricated on chip in a CMOS compatible process.

| Type of Resonator | Q value range | Size | Power Consumption |
|---|---|---|---|
| On-Chip Spiral Inductors | 10's | Small | Small |
| Off-Chip Inductors | 100's | Large | Large |
| MEMS | 10,000's | Small | Very little ✓ |

Figure 2.6: **Picture of table comparing different Solutions for Resonators in RF [2, 3]**

The demand for high performance, single-chip and multi-band solutions for RF technology for the coming generation of wireless technology will only grow. High Q passives are under increasing strain to be reduced as much as possible due to power consumption and size constraints. This includes quartz, ceramic, Film Bulk Acoustic Wave (FBAR), Surface Acoustic Wave (SAW) and any other off-chip IF filter for RF communications that must be interfaced to the integrated circuit logic. The motivation for this is quite simple: cost and size. When advantageous, handset design houses have resorted to direct conversion or on-chip inductor solutions. These solutions, however, often come at the cost of greater logic complexity at the integrated circuit level or higher requirements for circuit performance, which usually leads to an increase in power consumption of the overall design and design costs. This perilous situation is not assuaged by the future demands of multi-band devices that will require a high Q RF filter possibly for each wireless standard. Surface Acoustic Wave (SAW), Bulk Acoustic Wave (BAW) and Countor Mode Resonators (CMR) use the principle of electro-mechanical coupling for their operation. They are all a type of Micro-Electromechanical Systems (MEMS) device use the properties of the piezoelectric effect for operation. The relative simplicity and reliability have motivated a strong development over the last 30 years. SAW devices have been used as filters in televisions and VCRs since the late 70s, as well as in Radar [18], wireless headsets and mobile phones. Not only are they used for RF filtering techniques, but also as sensors in a vast swath of industries such as in gas detection, pressure sensors, biosensors and viscosity [19–21]. In order for an understanding of the operation of SAW, BAW and Lamb wave mode devices an understanding of piezoelectric film properties and waves is necessary and will be discussed in the next chapters.

# Chapter 3

# Elasticity, Piezoelectricity and Tensors

## 3.1 Aluminum Nitride

Aluminum nitride has seen extensive attention in recent years due to its possibilities not only in piezo-acoustic devices, but also in light emitting diodes and high temperature transistors. Group-III nitrides can be of three crystalline structures wurtzite, zinc blend and rock salt Figure 3.1 [4,22]. AlN has the largest band gap (6.2eV) of the Nitride family, a large Young's Modulus, high acoustic wave speed, high thermal conductivity and fairly moderate piezoelectric coupling coefficient. It is also compatible with contemporary CMOS processes making It viable for future on-chip integration [23].
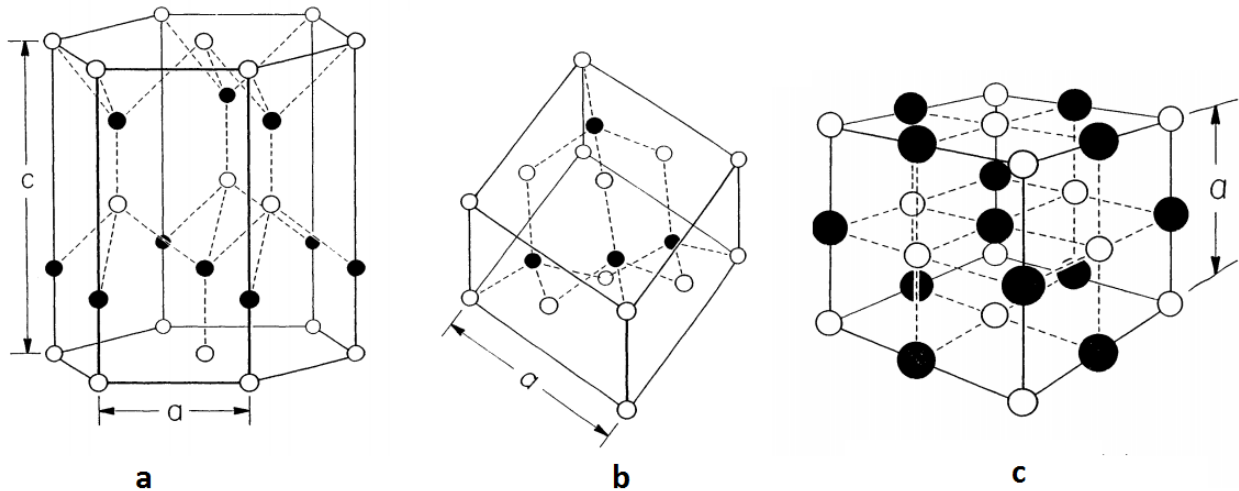


Figure 3.1: **Nitride Crystal Structures (a) Wurtzite, (b) Zinc Blend (c) Rock Salt** [4]

In ambient conditions AlN is most thermodynamically stable in the Wurtzite form, although a pressure induced rock salt phase has been induced experimentally around 46 GPa [24–26].

## 3.2 Elasticity and Tensors

### 3.2.1 Tensors

A tensor is an array of numbers that indicates magnitude and direction of, in this case, physical material in several dimensions, in the context of elasticity, we will be using the stress tensor $\sigma_{ij}$, a 3X3

matrix. The starting point for understanding elastic materials and tensors is best done with a simple cube. If a force is applied to a cube as depicted below in Figure 3.2 it will deform. If that deformation is non-permanent, that is if the material returns to its original shape after remove an applied stress than the material is defined as elastic. The original state of a material when it is not undergoing an external stress is termed its natural state.
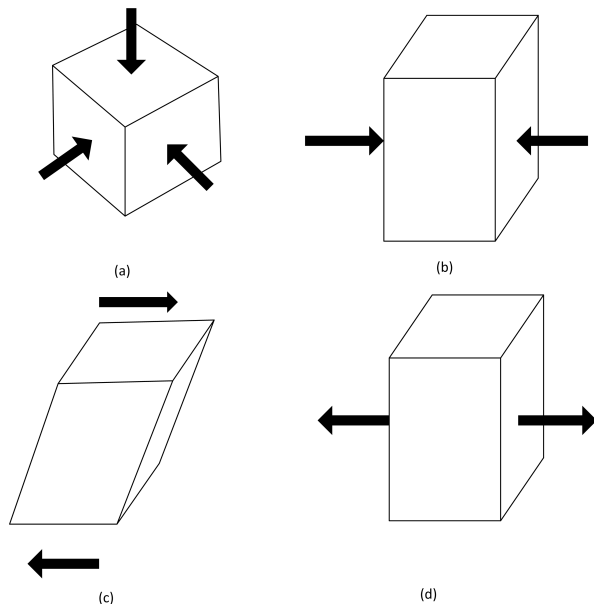


Figure 3.2: **Different types of applied stress**
(a) equal stress (b) compressive (c) shear stress (d) tensile

### 3.2.2 Elasticity

A stress is defined as a force that acts on a material to produce a strain. A stress is a force over an area and is given in units of pressure (Pascals $\frac{N}{m^2}$). In (a) the stress is equal in all directions, in (b) the stress is uniaxial which causes a compressional stress. A tensile strain as in (d) or a shear stress (c) which results in a translation of the material.

In the 17th century Robert Hooke described a large group of materials that exhibit a linear relationship between stress and strain. These are termed linear elastic materials [27, 28].
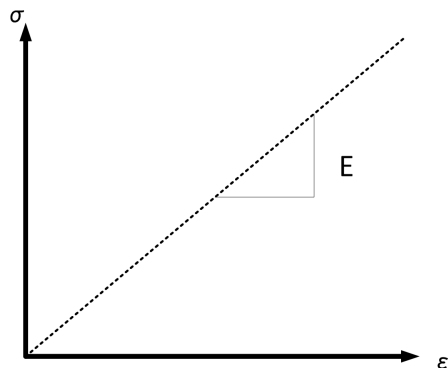


Figure 3.3: **General Plot for Linear Elastic Materials**
where $\sigma$ is stress, $\epsilon$ is strain and E is young's modulus
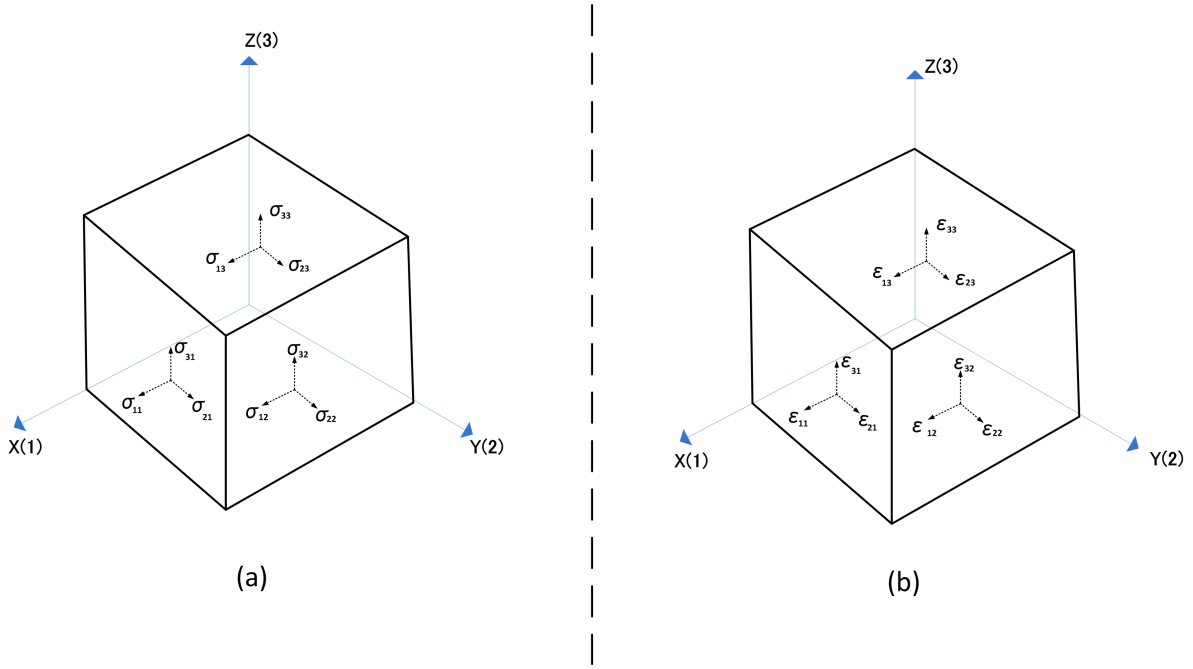
Figure 3.4: **Different types of applied stress $\sigma_{ij}$ and strain $\epsilon_{kl}$**

To understand how material properties are represented, consider a cube of material. In this cube the normal to each cube face is parallel to the cube edges, it is an orthogonal system. The stresses in the cube are represented by $\sigma_{ij}$ where the two subscripts i and j represents the direction of the force applied to the cube face i and j represents the direction of the normal to the cube face of the force being applied. Consider also, $\epsilon_{kl}$ where k and l are equivalent to i and j respectively, these directions are represented with the number 1, 2, 3 as numbered in Figure 3.4 above for the respective Cartesian Axes, if the medium is in static equilibrium the sum of all the stress components in the 1, 2, 3 directions is zero. This can be represented as:

$$\sigma_{ij} = \sigma_{ji} \tag{3.1}$$

The stress tensor can be used to describe the state of stress at any point within the medium.Stress with positive values are torsional stresses and stresses with negative values are compressional stresses. Stresses can be though of as a kind of pressure:

$$P = -\sigma_{ii} \tag{3.2}$$

$$\sigma_{ij} = \begin{pmatrix} \sigma_{11} & \sigma_{12} & \sigma_{13} \\ \sigma_{21} & \sigma_{22} & \sigma_{23} \\ \sigma_{31} & \sigma_{32} & \sigma_{33} \end{pmatrix} \quad with\ i, j = 1, 2, 3 \tag{3.3}$$

When an elastic material has a stress applied to it, it will deform. This deformation is termed strain. Strain is the fractional change in the dimensions of a material being subjected to a strain.

$$\epsilon_{kl} = \frac{1}{2} \left( \frac{\partial u_k}{\partial x_l} + \frac{\partial u_l}{\partial x_k} \right) = \begin{pmatrix} \epsilon_{11} & \epsilon_{12} & \epsilon_{13} \\ \epsilon_{21} & \epsilon_{22} & \epsilon_{23} \\ \epsilon_{31} & \epsilon_{32} & \epsilon_{33} \end{pmatrix} \quad with\ k, l = 1, 2, 3 \tag{3.4}$$

11

Just as with the stress tensor, the strain tensor has six independent variables.

$$\epsilon_{ij} = \epsilon_{ji} \tag{3.5}$$

Depending on the temperature, direction of stress and the material properties of the material its reaction will be different.



(a)    (b)
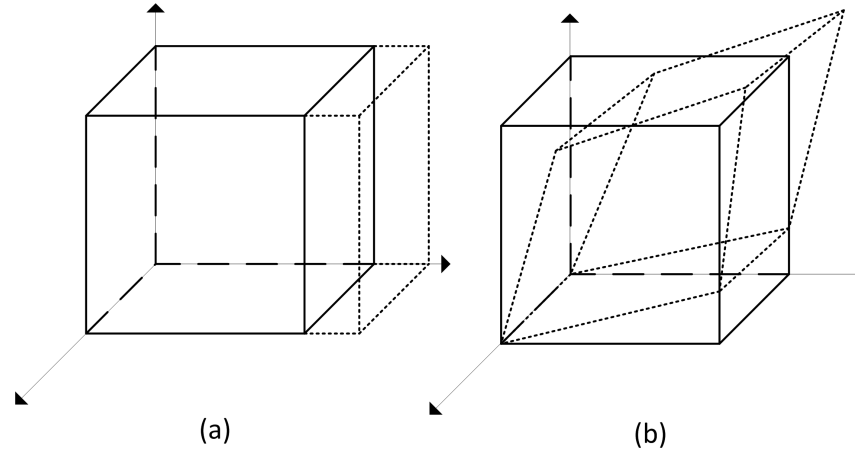
Figure 3.5: **(a) tensile strain (b) shear strain**

Shear strains are measured in radians in the case of this example a torque is applied in the direction of the Z axis a resulting strain of $\epsilon_{23}$ and $\epsilon_{32}$ .The resulting strain is measured in radians for the cube. $\epsilon_{23} + \epsilon_{32} = \gamma$, depicted in Figures 3.5 and 3.6.



(a)    (b)
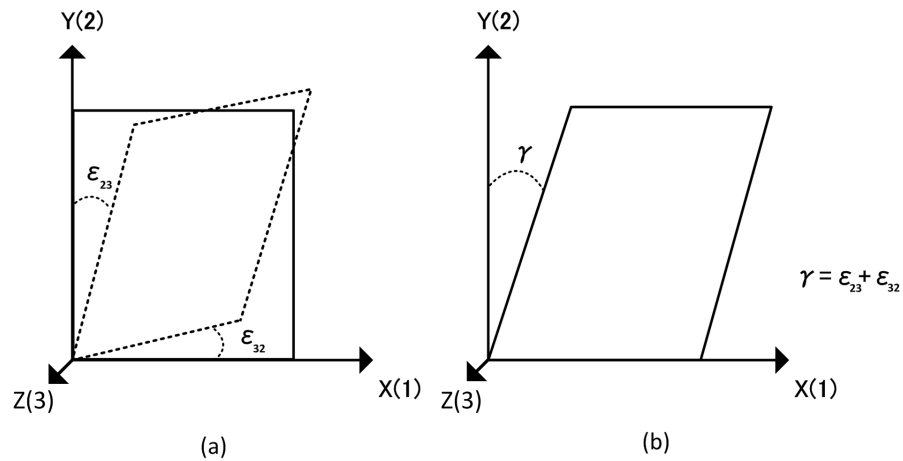
Figure 3.6: **(a) shear strain top view (b) shear strain translated to X axis**

Elastic materials have a proportional relationship between the an applied stress $\sigma$ resulting in a strain $\epsilon$. This relationship is known as Hooke's Law, the proportionality constant between the stress and resulting strain is known as Young's Modulus E [Pa], shown graphically in Figure 3.3.

$$\sigma = E \cdot \epsilon \tag{3.6}$$

The above Equation 3.6 describes a force applied in the direction of a single unaxial stress with the three resulting strains; one is elongating the material and the other two are lateral strains orthogonal to the applied stress. This relationship is usually described in terms of elasticity, which is the inverse of Young's Modulus $\frac{1}{E}$.
Compliance Tensor

$$\epsilon_{ij} = S_{ijkl} \cdot \sigma_{kl} \tag{3.7}$$

It is also typical to describe the stress situation where it is applied on three directions and results in a unidirectional strain with the proportionality constant called stiffness C.
Stiffness Tensor

$$\sigma_{ij} = C_{ijkl} \cdot \epsilon_{kl} \tag{3.8}$$

Further details of matrices of elasticity can be found in Appendix A.

### 3.2.3 Piezo electricity

The word "piezo" is a Greek word which means "to squeeze". The direct piezoelectric effect was first observed in 1880 by the Curie brothers [29]. The effect is understood as a linear electro-mechanical phenomenon between the mechanical and electrical state in crystals without a center of symmetry. The direct piezoelectric effect is defined as a mechanical deformation in a piezoelectric material when an electric field is applied to it. The converse piezoelectric effect is defined as when a mechanical deformation in a crystal causes a proportional electric field to be induced in the material. Figure 3.7 gives a pictorial view of aluminum nitride under compressive and tensile stress. In this case the aluminum atoms are in a tetrahedral coordination with nitrogen, due to the nature of the bonds, the bond angles can be stressed or strained in such a way that the electric dipole is not neutral and compounding this effect at a macro level leads to the observation of peizoelectric effect.

In Figure 3.8 the piezo electric coordinate systems is depicted, this is used to indicate which direction the piezoelectric material will actuate based on the direction of the voltage applied, where 3 represents the Z axis, 2 represents the Y axis and 1 the X axis respectively.
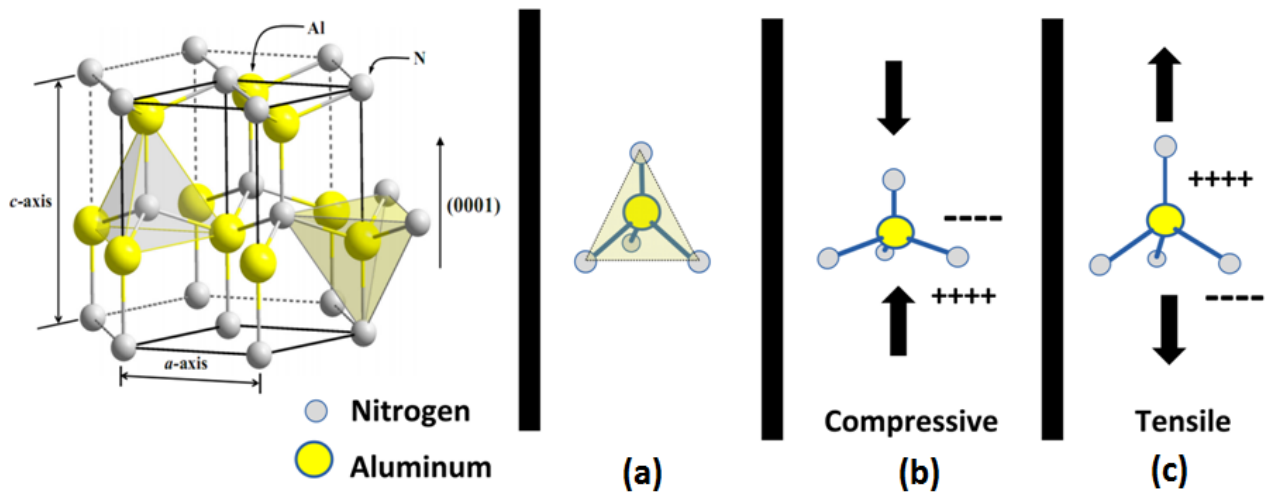
Figure 3.7: **Piezo-Electric Effect in Aluminum Nitride**
In (a) the AlN tetrahedral form is at rest without any stress, strain or agitation. The AlN bond is less compressible than the N-Al-N bond angle, in (b) the Al moves closer to the bottom 3 Nitrogen atoms and has a dipole. In (c) a tensile stress elongates the Al-N bond causing the opposite effect. Image modified from [30]
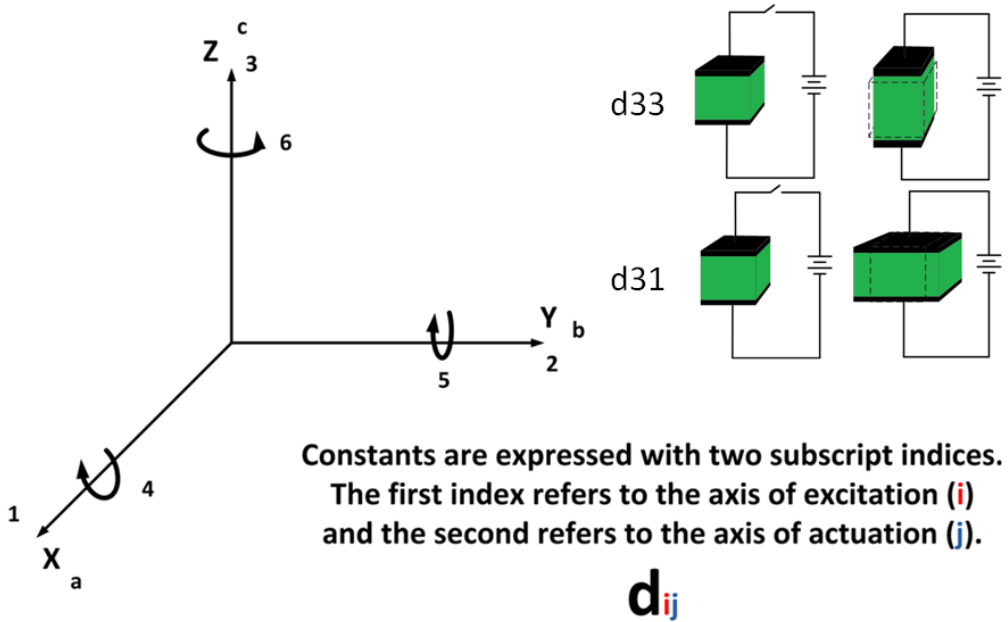


Figure 3.8: **Piezo-Acoustic Coordinate System**

### 3.2.4 Stress-Charge Form

Hook's Law as shown in Equation 3.6, along with the constitutive equation for dielectrics in Equations 3.9 and 3.10 are coupled together in the two coupled equations 3.10 and 3.11 [31–35].

$$S = s \cdot T \tag{3.9}$$

Where S is the strain, s compliance and T the stress of the material.

$$D = \epsilon \cdot E \tag{3.10}$$

Where D is the Dielectric Displacement, $\epsilon$ is the permittivity and E is the Electric Field.

$$S = s_E \cdot T + d^t \cdot E \tag{3.11}$$

$$D = d \cdot T + \epsilon_T \cdot E \tag{3.12}$$

Where both equations are related through the piezoelectric constant $\frac{C}{m^2}$. Where T is the transverse of e, and the superscript E and S indicate that those respective variables have been measured at constant electric field or constant strain respectively.

$$T_{ij} = c_{ijkl}^E \cdot S_{kl} - e_{kij}^T E_k \tag{3.13}$$

$$D_i = \epsilon_{ik}^S \cdot E_k + e_{ikl}^T S_k l \tag{3.14}$$

Futher information can be found in Appendix B, as well as the material properties of aluminum nitride that were used later in this thesis for device simulation .

## 3.3 Basic Acoustic Theory

Acoustics is an important topic in the field of piezo-acoustic devices. Acoustics is an interdisciplinary science that deals with the study of all mechanical waves in solids, liquids and gases. A wave is a disturbance in an elastic medium that travels through matter, or space and transfers energy. Mechanical waves travel via a displacement in the physical medium, but have no permanent effect on the position of the particles in that medium.

### 3.3.1 Motivation

The motivation for using acoustic waves is the major reduction in size, relative to traditional electronic components used to filter wafes, as well as an enormous increase in the quality factor. The wave velocity of an Electromagnetic wave $\nu_{\text{EM}}$ is far higher than that of an acoustic wave $\nu_{\text{SAW}}$.

$$\nu_{\text{EM}} \approx 3,000,000 \, \frac{m}{s}; \; \nu_{\text{SAW}} \approx 3,000 \, \frac{m}{s} \tag{3.15}$$

Lord Rayleigh discovered Surface Acoustic Waves (SAW) in solids. These kind of waves travel on the surface of a medium and propagate approximately 2 wavelengths into the solid [36]. Surface and Bulk acoustic waves are several thousand orders of magnitude slower than the propogation of electro-magnetic waves.

$$\frac{v_{\text{EM}}}{v_{\text{SAW}}} = \frac{3,000,000 \, \frac{m}{s}}{3,000 \, \frac{m}{s}} = 10^{-5} \tag{3.16}$$

The difference in wave speed is $10^{-5}$

$$c = \nu_{\text{EM}} \tag{3.17}$$

Table 3.1: **Wave Modes in Solids** [8]

| Medium | Wave Mode | Particle Vibrations |
|---|---|---|
| Bulk | Longitudinal | Parallel to wave direction |
| Bulk | Transverse (Shear) | Perpendicular to wave direction |
| Surface | Rayleigh | Elliptical orbit close to surface in the x-z plane |
| Plate | Lamb/Plate Wave | Elliptical orbit in x-z plane symmetrically, or anti-symmetrically throughout plate thickness |

### 3.3.2 Wave Characterization

Waves can be characterized in space by sinusoidal wave forms that exhibit a typical predictable pattern in space. Wave propagation type is referred to as wave modes. The two major types of wave modes are longitudinal and transverse (Shear). Refer to Table 3.1 for a summary of some of the most common modes of wave propagation in a solid.

The wave speed is governed by the wave equation. The wave propagation velocity $\nu$ is a product of the frequency f $[s^{-1}]$ and wavelength $\lambda$ [m].

$$\nu = \lambda \cdot f \tag{3.18}$$

The wave speed $\nu$ $[\frac{m}{s}]$ is different for different materials, it is the maximum speed with which a wave may propagate within a material. The speed with which a wave can travel through a material is dependent on it compressibility. The derivation of this was determined initially by Newton and corrected by Laplace [37]. It is determined Newton-Laplace equation by the density $\rho$ $[\frac{Kg}{m^3}]$ of the particles in the medium, and the spring constant $C_{ij}$ [GPa] of the material is governed by the general equation.

$$\nu = \sqrt{\frac{C_{ij}}{\rho}} \tag{3.19}$$

The above equation may take different forms depending on the type of wave traveling in the medium under consideration. For a more detailed derivation a detailed source can be found [38]. The i and j subscripts in $C_{ij}$ are a notation system used to elicit direction in a medium. In materials that have the same elastic spring constant in all directions it is referred to as isotropic material, for materials that have differing elastic spring constants in different directions the material is referred to as anisotropic. Because most materials have different elastic constants depending on the direction matrix notation must be used to describe a material in the Cartesian coordinate system.

It is important to understand the nature of waves as they propagate through a medium, emanating from a source. It is of prime importance that the equations governing the motion of waves are understood and modeled via mathematics. When a source of disturbance is located near or on an elastic medium, waves will be produced. If the oscillations are in the air and if the frequency of those waves are within 20 to 20,000 kHz it will be heard as a sound. Rarefaction is the reduction of an item's density, the opposite of compression.

If $P_o$ is the average pressure of the medium and the pressure of the medium at the highest point of compression $\delta p$ the pressure would be $P_o + \delta p$, the lowest point of rarefaction $P_o - \delta p$. As time goes forward the wave advances through the medium and the limits of the highest and lowest points of rarefaction change. This change in pressure can be modeled as a sine wave Figure 3.9. If the absolute value of the maximum difference in pressure in rarefaction or compression is called A than the equation would be written as follows,

$$y = A \cdot sin(\omega \cdot t - \frac{x}{\nu}) \tag{3.20}$$
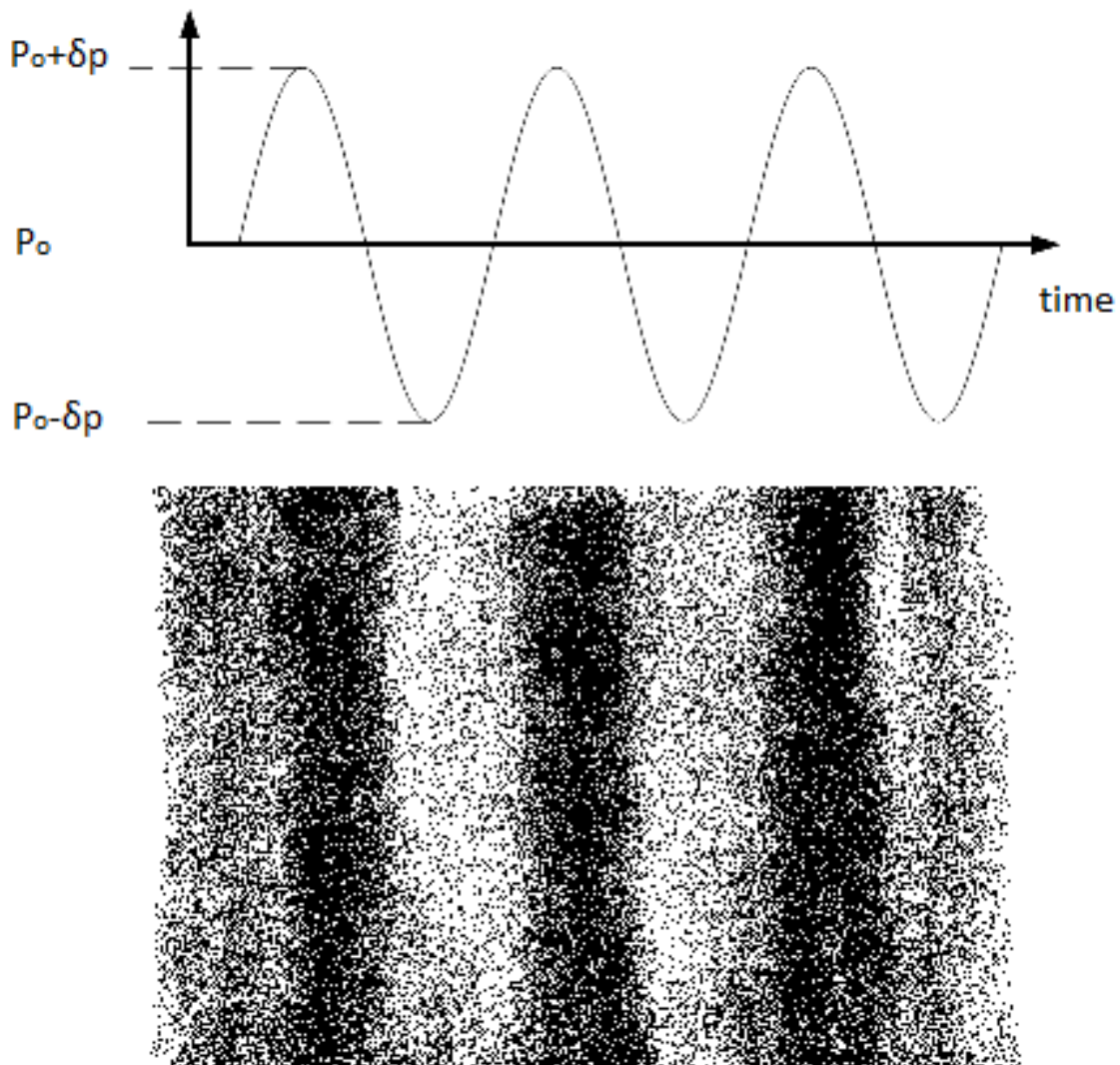
Figure 3.9: **Sine wave model of pressure in a longitudinal wave**

where $\omega$ is the angular frequency, t is time and A is the amplitude. The velocity of the waves produced is a constant velocity, this constant velocity is determined by the material properties of the medium: density, viscosity and the elasticity of the medium through which the waves propagate.Now let the speed of the waves propagation be $\nu$ and the pressure at any position be x.

$$y = Asin(\omega \cdot t) \tag{3.21}$$

where A is the amplitude of vibrations, $\omega$ is the angular frequency and $\theta$ is the phase and t is time.

$$y = A \cdot sin(\omega \cdot t - \theta) \tag{3.22}$$

For wavelength $\lambda$ the phase difference from peak to peak will be $2\pi$. x corresponds to $2\pi\frac{x}{\lambda}$.From this the phase difference $\theta$ can set to $2\pi\frac{x}{\lambda}$ and $\omega$ set to $\frac{2\pi}{T}$ where T is the period. From this we can take Equation 3.22.

$$y = A \cdot sin(\frac{2\pi}{T} \cdot t - 2\pi \frac{x}{\lambda}) \tag{3.23}$$

$$y = A \cdot sin(2\pi \cdot (f \cdot t - \frac{x}{\lambda}) \tag{3.24}$$

since $\nu = f \cdot \lambda$ it can be replaced.

$$y = A \cdot sin(2\pi \cdot (\frac{\nu}{\lambda} \cdot t - \frac{x}{\lambda}) \tag{3.25}$$

$$y = A \cdot sin(\frac{2\pi}{\lambda} \cdot (\nu \cdot t - x) \tag{3.26}$$

$$y = A \cdot sin(\omega \cdot (t - \frac{x}{\nu})) \tag{3.27}$$

velocity of a wave

$$y = \frac{dy}{dt} = v = A \cdot \omega \cdot cos\left(\omega \cdot (t - \frac{x}{\nu})\right) \tag{3.28}$$

acceleration of a wave

$$\frac{d^2 y}{dt^2} = a = -\omega^2 \cdot A \cdot sin\left(\omega \cdot (t - \frac{x}{\nu})\right) \tag{3.29}$$

$$\frac{d^2 y}{dt^2} = \nu^2 \cdot \frac{d^2 y}{dx^2} \tag{3.30}$$

The behavior of particles having now been derived, this can be used to understand the design premises used therein. For example, waves which travel on the surface travel in an elliptical pattern, waves that travel through the bulk of a material are longitudinal waves, and waves that travel in thick plates (that is plates where the wavelength of the waves is greater than the thickness of the plate) are Lamb waves, this is important in designing different types of devices, since the acoustic waves speed used will be different, depending on the targeted frequency.

### 3.3.3 Waves

There are four major modes of wave propagation in solids, Transverse waves, Longitudinal waves, Raleigh waves and Lamb waves refer to Table 3.1. These four major modes of wave propagation are illustrated below in Figures 3.10, 3.11, 3.12, 3.13.
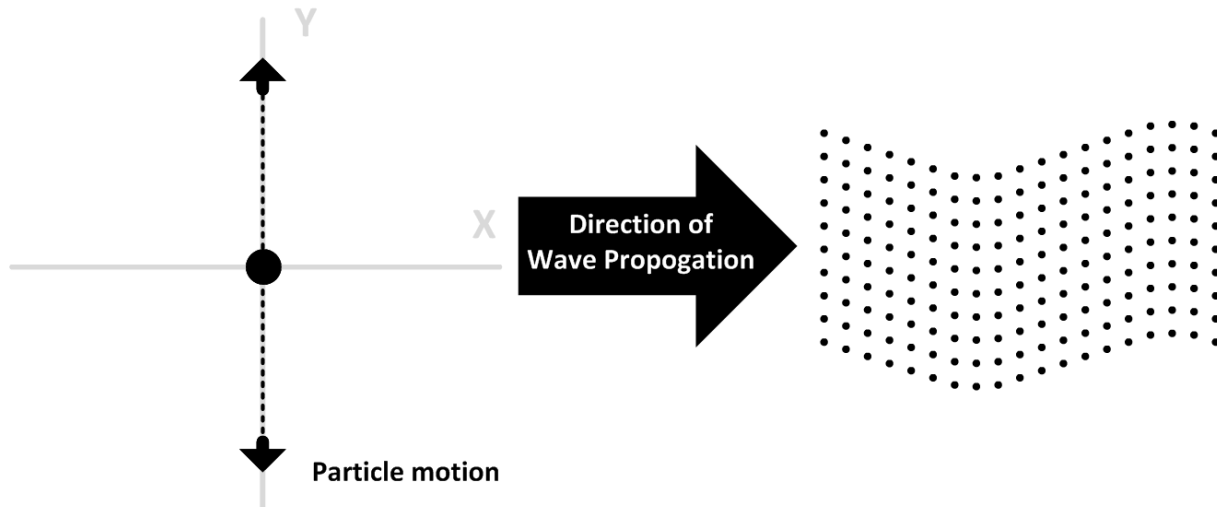


Figure 3.10: **Transverse Waves**

In transversal waves, (Figure 3.10) the medium is excited, or disturbed it transmits its energy to the next particle in a direction perpendicular to the direction of propagation of the wave.
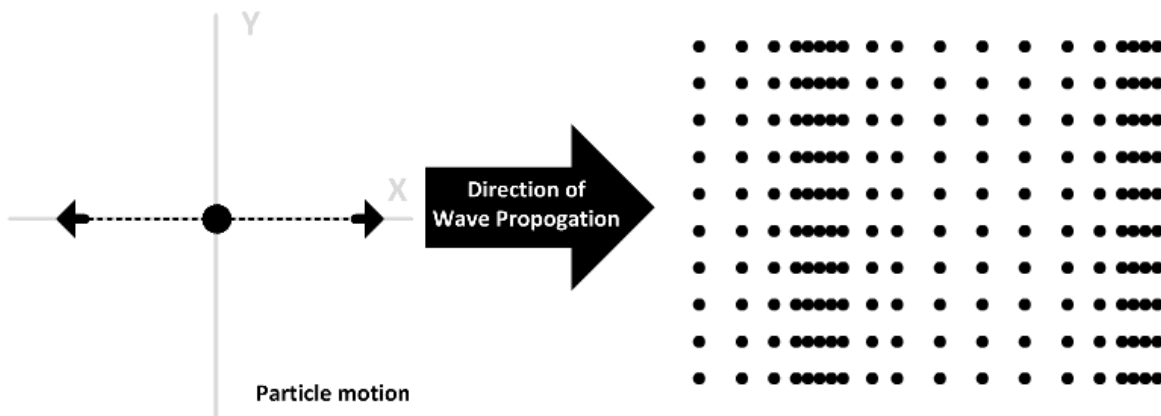


Figure 3.11: **Longitudinal**

In longitudinal waves (Figure 3.11) the medium is excited, or disturbed it transmits its energy to the next particle in a direction parallel to the direction of propogation of the wave.

Lord Rayleigh postulated Surface Acoustic Waves (SAW) in solids when trying to analyze the propagation of waves in Earthquakes in 1885 [39]. These kind of waves travel on the surface of a medium and propagate along the free surface of the material, while the amplitude of the waves decay exponentially into the solid [36]. Surface acoustic propogate via longitudinal and transverse motion. The particle's motion is in the form of an ellipse as depicted in the above Figure 3.12.
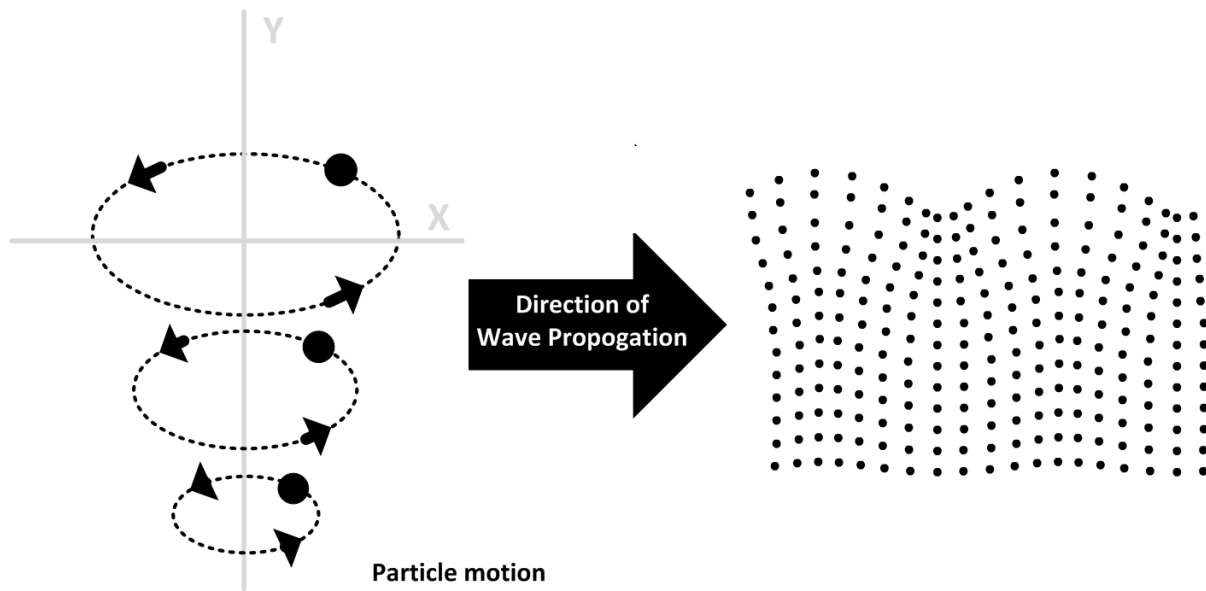
Figure 3.12: **Rayleigh Waves**



**Symmetric**                                    **Asymmetric**
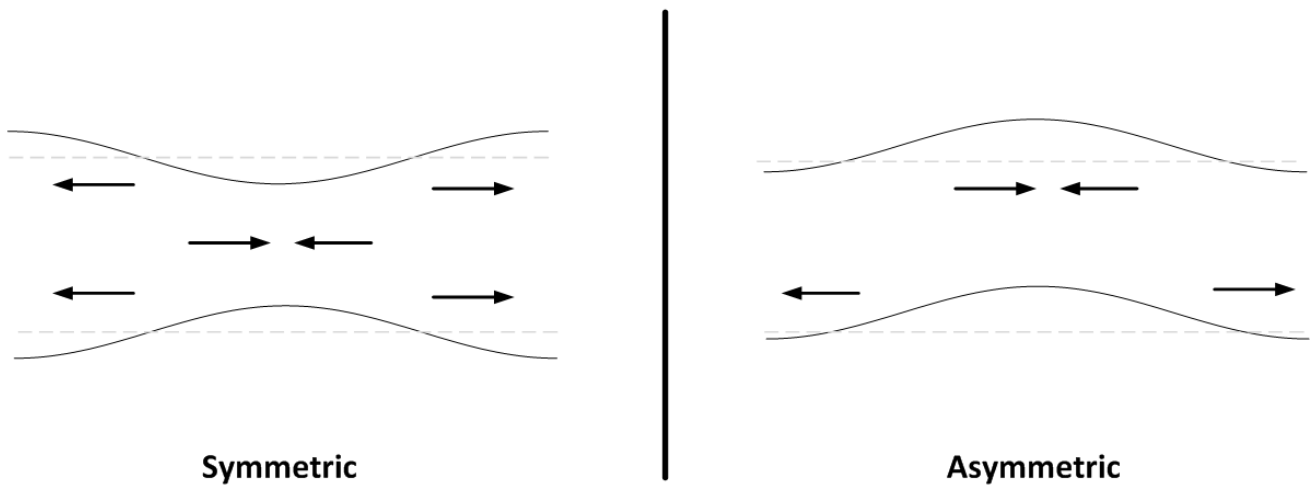
Figure 3.13: **Plate/Lamb Waves**

Plate Waves are waves that can be excited in an elastic medium that is only a few wavelengths thick. Plate Waves are also known as Lamb waves in Figure 3.13. There are two modes of Plate Waves or Lamb Waves called Symmetric $(S_0, S_1, ...)$ and Antisymmetric $(A_0, A_1, ...)$ modes. The Symmetric modes have a symettry about the center of the plate, whereas Antisymmetric the peak and trough of the waves are inverted on either side of the plate. The particles in this type of elastic medium also have an elliptical pattern of displacement about which they transfer energy. Lamb waves are also a combination of Transverse and Longitudinal Waves.

In Figure 3.14 a potential difference in applied voltage is shown to illustrate the way waves are formed in a RF MEMS acoustic device. As the alternating current is sent to the device it causes a periodic deformation of the piezo film, which can be thought of in terms of an acoustic wave, depending on the mode of vibration and type of device differing waves can be stimulated through the electro to mechanical transduction.

The type of waves being stimulated by the device is dependent on its design, where SAW resonators,
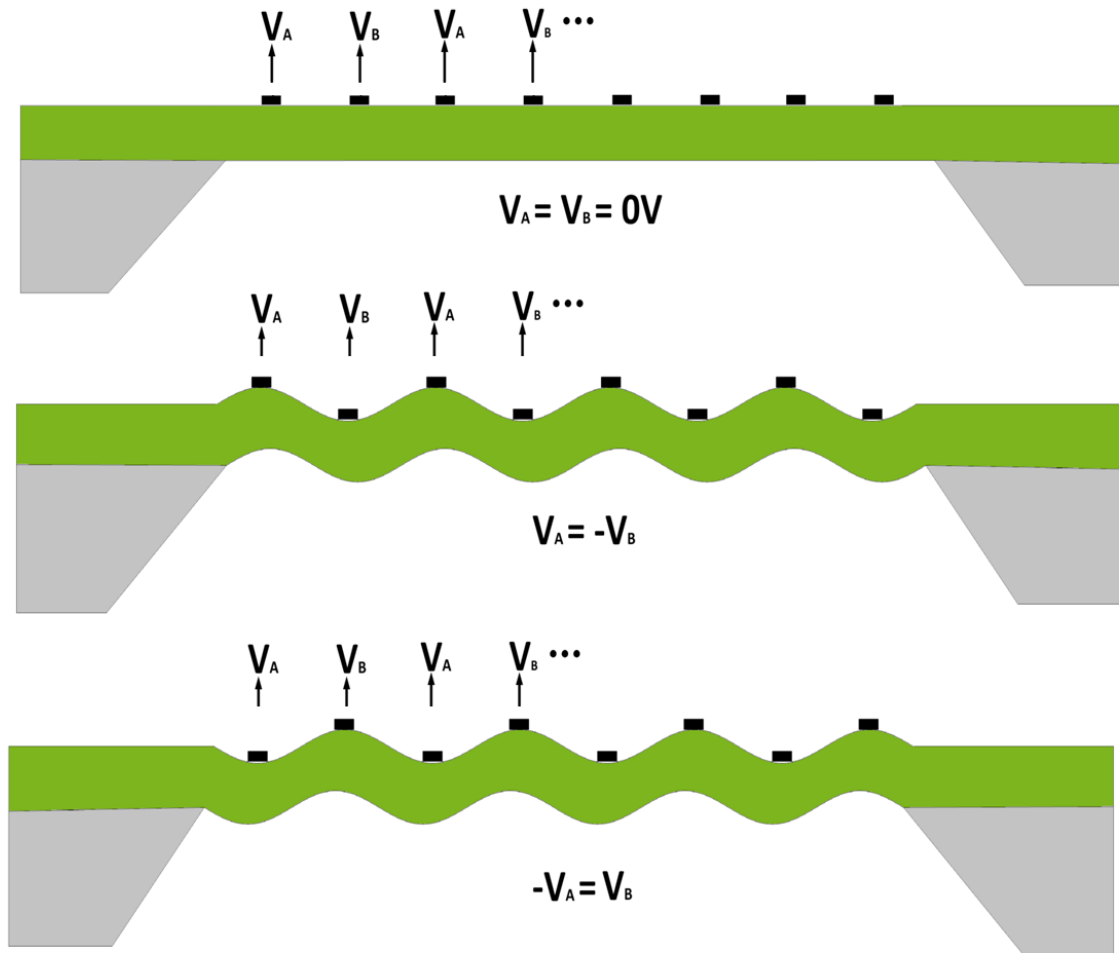
Figure 3.14: **Wave formation due to piezo-electric displacement**

use surface waves, BAW resonators use bulk acoustic waves and CMR resonators use Lamb waves to filter RF signals. The frequency of vibration depends on the devices used and their dimensions and practical implementation on the acoustic wave speed of the type of waves selected.

# Chapter 4

# Design

Piezo electric MEMS resonator design is a highly iterative process, with many possible degrees of freedom as shown in Figure 4.1. Device variables include the thickness of the material as in (a), the height of the metal electrode layers, the pitch of the electrodes, the use of a bottom electrode in floating or a grounded state (a and b), or the length and width of the anchor of tether that holds the resonators in places as they vibrate in plane( c and d), as well as the width and length of the resonator itself (d) [40–48].
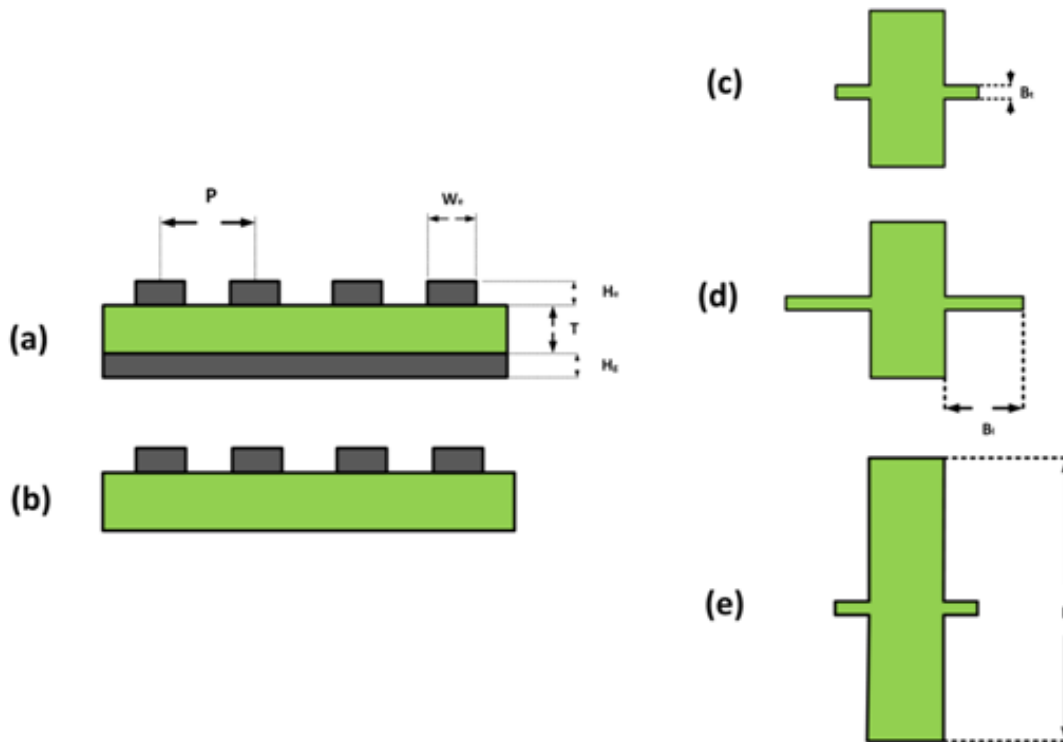


Figure 4.1: **Many Possible degrees of freedom in design**

The degrees of freedom available allow for a series of simulations which can be used to inform device design by targeting the most significant factors involved in influencing the target frequency.

## 4.1 Equations Governing Design
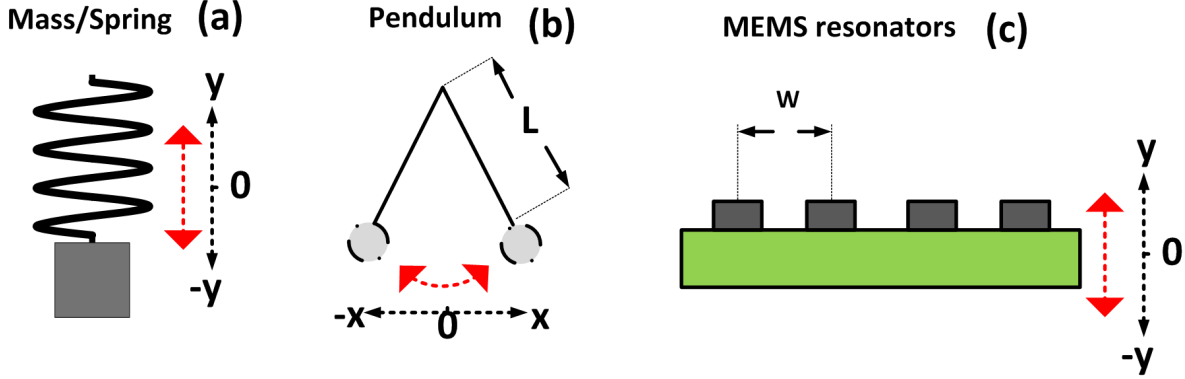


Figure 4.2: **Similar Oscillatory Systems**

The behavior of a resonator can be described by the model of mechanical damped harmonic oscillator [34, 49]

$$m_{eff}x'' + Dx' + kx = F_{ext}(x,t) = F_o \cdot sin(2\pi ft) \tag{4.1}$$

where x is the time varying harmonic displacement, $m_{eff}$ is the effective mass, D is the damping or drag constant, k is the spring constant, $F_{ext}$ is the external applied force to the resonant system, and $F_0$ is the amplitude of the harmonic force signal with frequency f. In Equation 4.1 the first term is the inertial force of the system, the second term is the damping and loss, and the third term is the restoring force.

$$f_n = \frac{1}{2\pi}\sqrt{\frac{k}{m^n_{eff}}} \tag{4.2}$$

Equation 4.3 gives the resonance frequency $f_n$, where n is the nth mode of resonance. The physical mass depends on the mass of the resonator, but also physical boundary conditions of the device itself including its geometry and resonance mode. This leads to some important information regarding the design of these devices:

1. Scaling down the physical dimensions of the device can increase the resonator's capacitance, which will decrease its impedance as the frequency increases

2. The effective mass is inversely proportional to the resonant mode; higher orders will have less energy than the fundamental frequency.

3. Scaling down the device leads to a reduction in the effective mass of the device, which also lowers the amplitude of vibrations.

This leads to the a need for different geometries for resonant devices based on the intended frequencies being targeted. This work has been shown in Figure 4.3 by Piazza et al where different plate and ring geometries were investigated [5], which lowers the motional resistance for a given frequency band thereby increasing the Q of the device.

In Equation 4.1 the damping or loss of the system D is given by:

$$D = \frac{2\pi f_n m^n_{eff}}{Q} \tag{4.3}$$
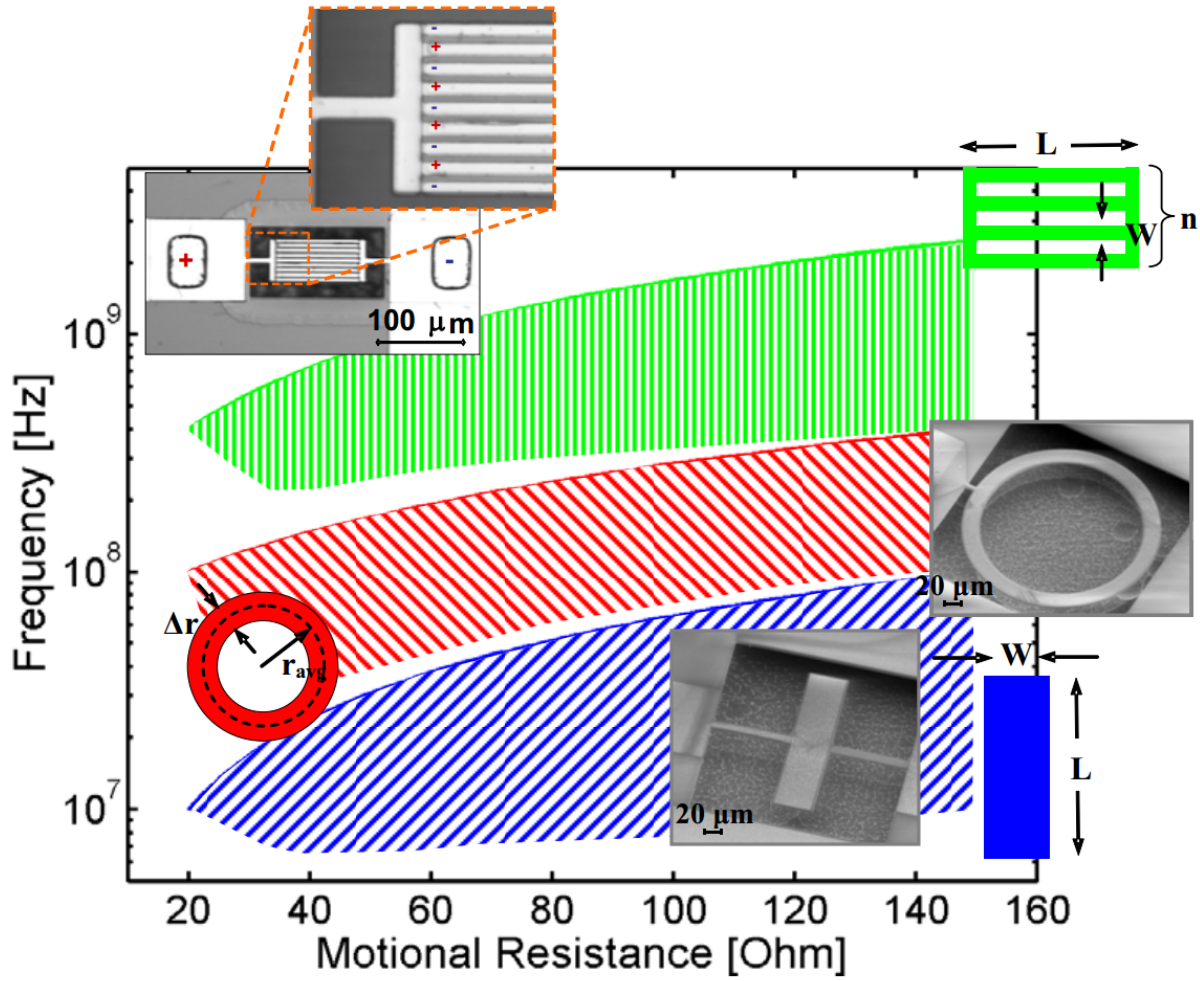
Figure 4.3: **Suitability of different geometries** [5]

where Q is the quality factor of the resonator, which was discussed already in the theory section. Q can also be determined by the drag or resistance of the system, and its effect on dissipating its energy per each period of oscillation, as shown in Equation 4.4.

$$Q = 2\pi \frac{Max\ Energy\ of\ One\ Period}{Energy\ Dissipated\ per\ Period} \tag{4.4}$$

## 4.2 Finite Element Analysis with COMSOL

The following simulations were done using COMSOL. COMSOL is a finite element analysis, solver and simulation software for physics and engineering applications. To explore the effects of different design configurations COMSEL FEA was done on a large number of iterations of an aluminum nitride contour mode resonator (CMR) to understand the effects that would result. In many cases second order effect were seen where a different mode of vibration was induced. This higher order modes can also be used in a bandpass filter and were modeled in COMSOL.
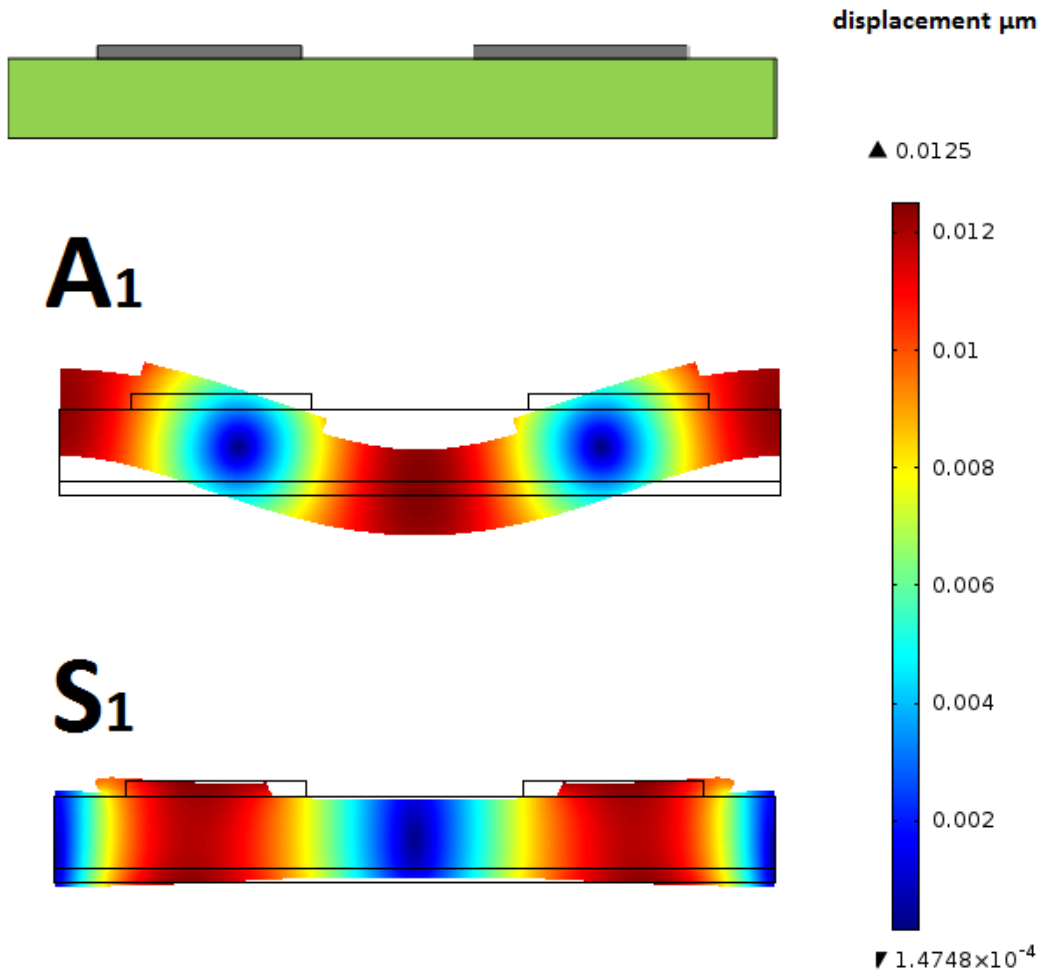


Figure 4.4: **General Plot for $S_1$ and $A_1$ modes for first configuration, the differences in displacement are painted different colors by COMSOL in order to emphasize the differences**

In Figure 4.2 the symmetric $S_1$ and antisymmetric $A_1$ modes of a 2D Lamb wave mode device is shown. This will be important in simulations following this one. The type of wave as well determines, the frequency of resonance for a particular mode, as well as giving several modes of resonance for a particular device.

**Piezo Film Thickness changes**
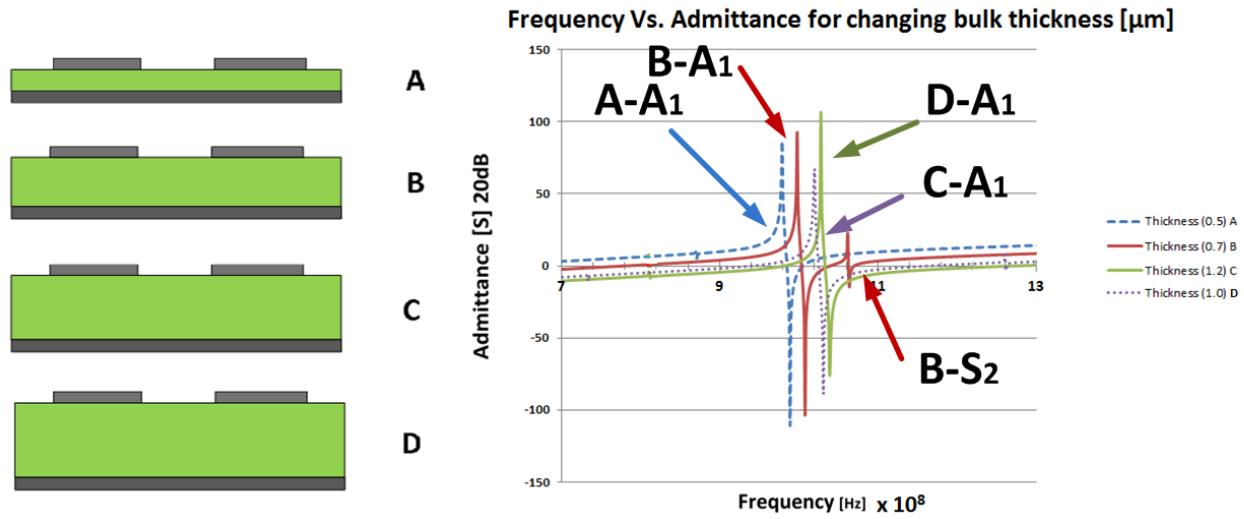


Figure 4.5: **Piezo Film Thickness changes**

In Figure 4.5 the piezo electric bulk thickness in A, B, C and D is altered from 0.5 $\mu$m to 0.7 $\mu$m to 1.0 $\mu$m and 1.2 $\mu$m respectively, the figure is a plot of $20 \cdot log(admittance)$ vs frequency, where admittance is the inverse of impedance. The simulated Lamb wave mode devices are swept with an RF frequency from .7 to 1.3GhZ. The result is the frequency response of the device for differing, peizo film thicknesses. The $A_1$ mode, resonant frequency of the device gradually increases, as well as giving a $S_2$ mode for the 0.7$\mu$m thick configuration.

**Electrode Height**
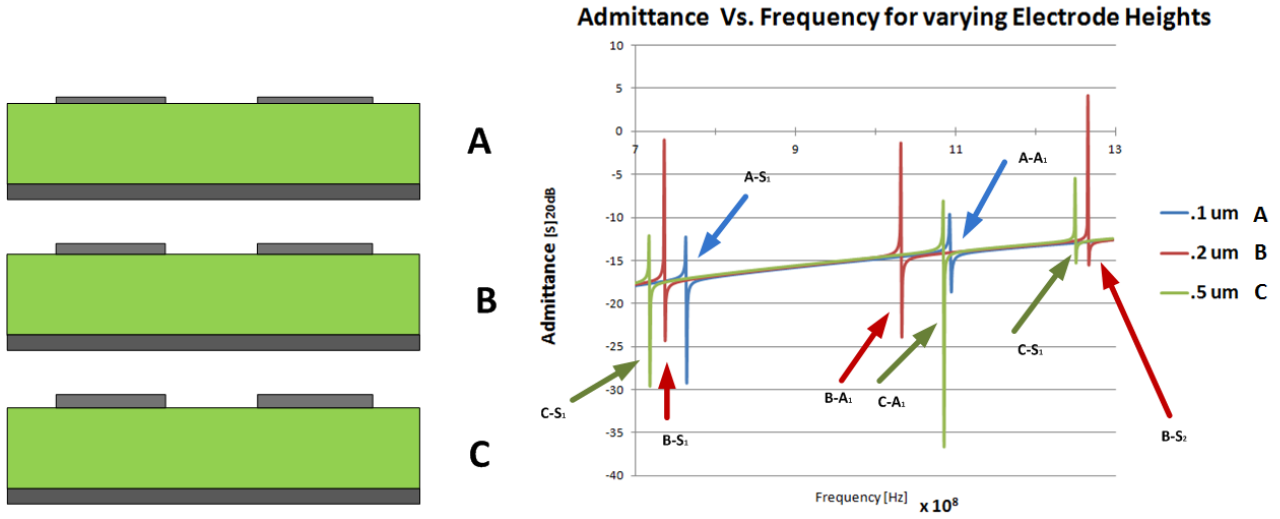


Figure 4.6:  **Electrode Height**

In Figure 4.6 the electrode thickness is altered from 0.1 $\mu$m to 0.5 $\mu$m, the $A_1$, $S_1$ and $S_2$ modes can be seen, the resonant frequencies of the device gradually increases, with a decrease in the thickness of the electrodes, this is due to mass damping effects in the overall device.

**Lateral Field Excitation**
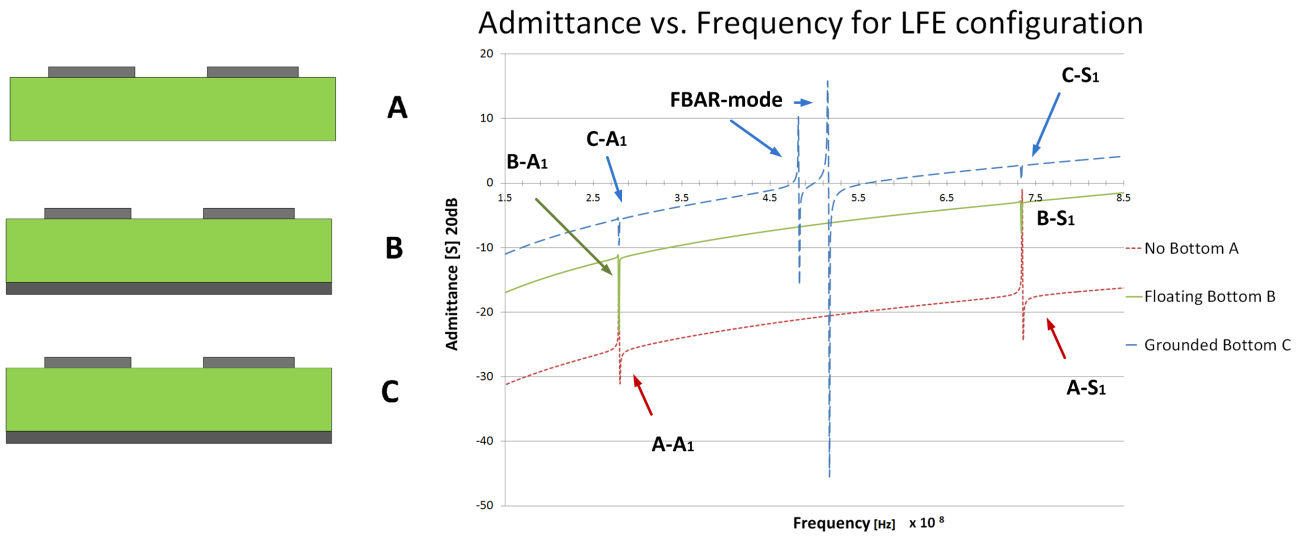


Figure 4.7: **Lateral Field Excitation**

In the Figure 4.7, a COMSOL simulation was done by altering the thickness of the piezosubstrate between the electrode, with the thickness reduced there is an overall increase of admittance of the device with a decreasing thickness. Due to the nature of capacitance, when the thickness of a dielectric between two plates declines it will increase the overall capacitance thereby increasing the admittance of high frequency signals. This effect leveled off between 1.0 $\mu$m and 1.2 $\mu$m.

**Thickness Field Excitation**
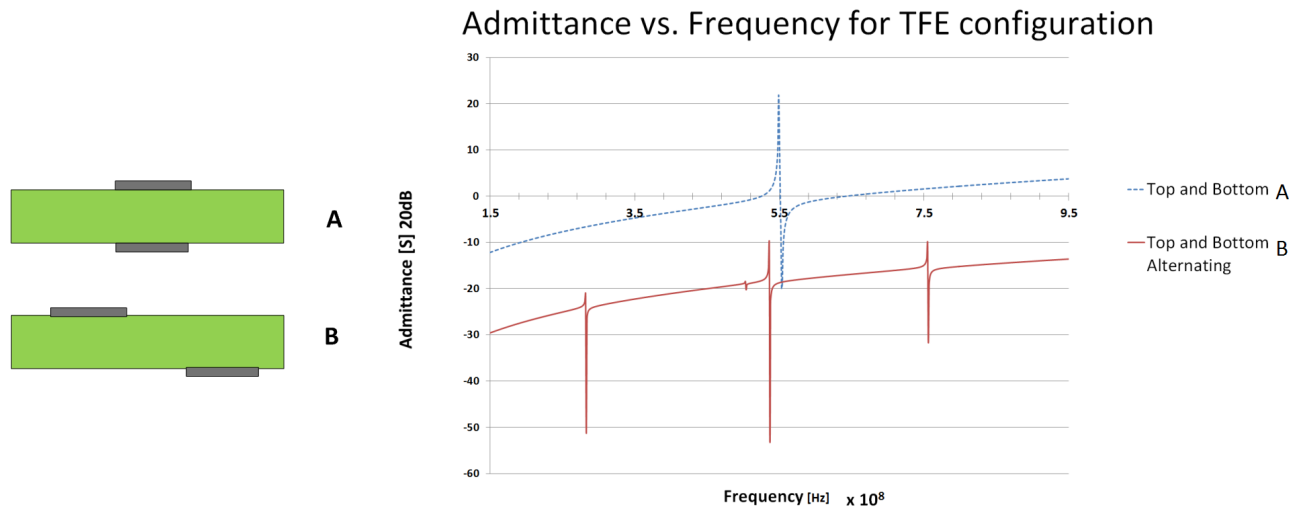


Figure 4.8: **Thickness Field Excitation**

In the Figure 4.8, a COMSOL simulation was done by altering the electrode configuration. In simulation (A) an FBAR, longitudinal mode is dominate, in configuration (B) there is also an FBAR mode as well as two Lamb wave modes induced to vibration, for grounded bottom (C), there is an additional resonant frequencies due to two new FBAR modes of vibration.

**Time Dependent Simulation**
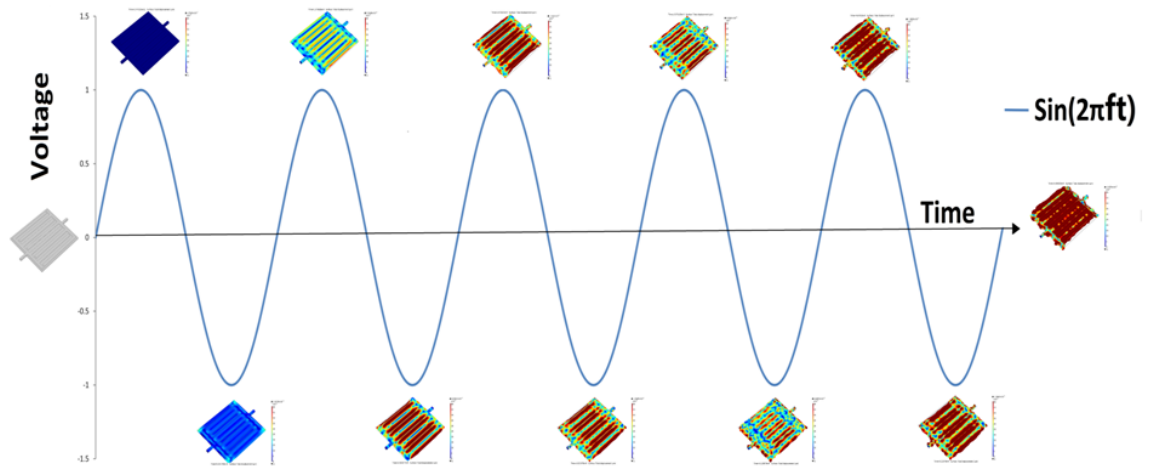


Figure 4.9: **Wave formation due to piezo-electric displacement**

The following simulations are time dependent, Figure 4.9 shows a Lamb wave resonator from t=0 to t=5$\pi$. The input signal is written below in equation 4.5, the resonator is given an sinusoidal input signal equal to its resonant frequency. The resonator's displacement gradually grows due to constructive interference before arriving at a steady state.

$$Input\ Signal = sin(2\pi f_0 t) \tag{4.5}$$

where t goes from 0 to 10$\pi$

Figure 4.10 is a SAW resonator at 0 and 10$\pi$ of its resonant frequency, with its accumulated interference pattern, as the waves reflect off of the edges of the device there is a clear grating pattern that develops, this is due to the mode of resonance which is based on Rayleigh waves and is determined by the pitch of the interdigitated fingers. Figure 4.11 is a LAMB resonator at 0 and 10$\pi$ of its resonant frequency, with its accumulated interference pattern, where the displacement pattern shows a "swinging of the resonator laterally as well as a secondary interference pattern from the input and output, the frequency of resonance is determined by the thickness of the device as well as the pitch of the interdigitated fingers. Figure 4.12 is a BAW resonator at 0 and 10$\pi$ of its resonant frequency, with its accumulated interference pattern, at steady state the BAW device shows strong displacement, the device's resonance is determined by the bulk thickness of the film and uses longitudinal waves for as the means for oscillation.

For a video of the following time dependent simulations refer to the hyperlink SAW BAW CMR Time Dependent Simulations, the URL is available in Appendix C, the simulations are strongly recommended as they show the wave pattern develop and reach steady state, which can greatly aid the reader in comprehension.
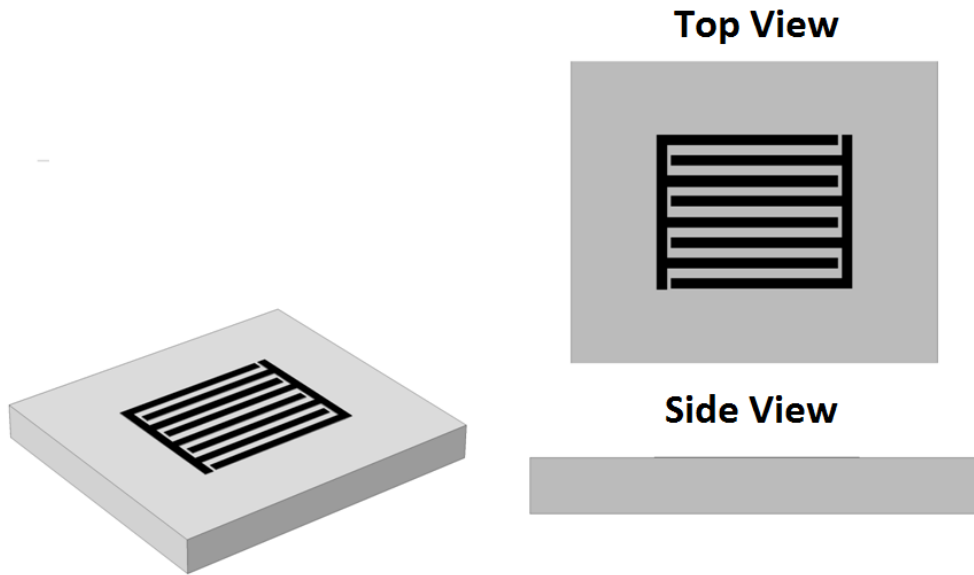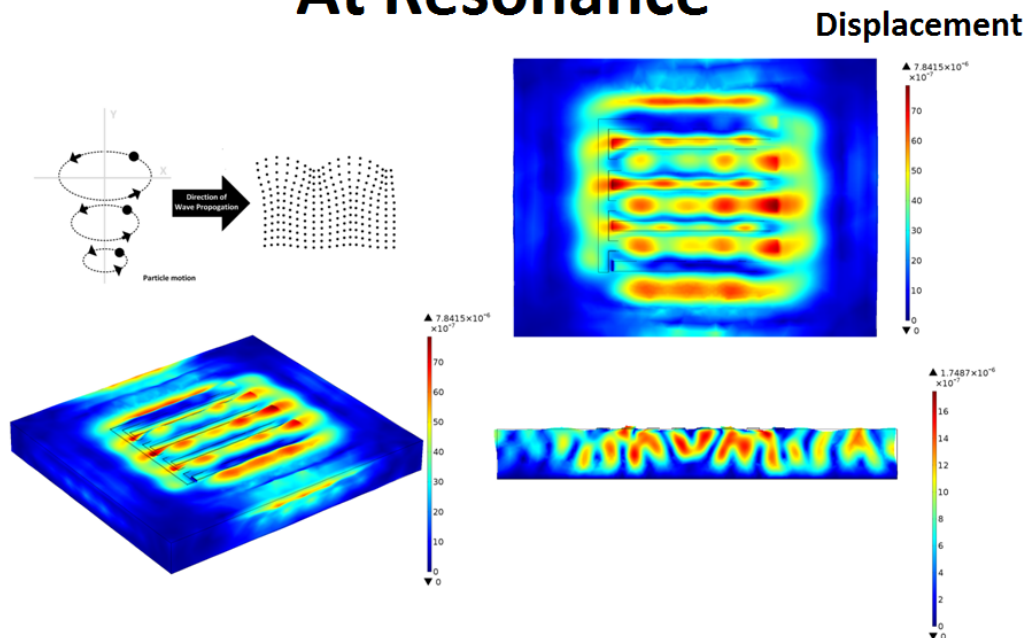
Figure 4.10: **Surface Acoustic Wave Device Simulation working principle**

# Lamb Wave-Contour Mode Resonators (CMR)
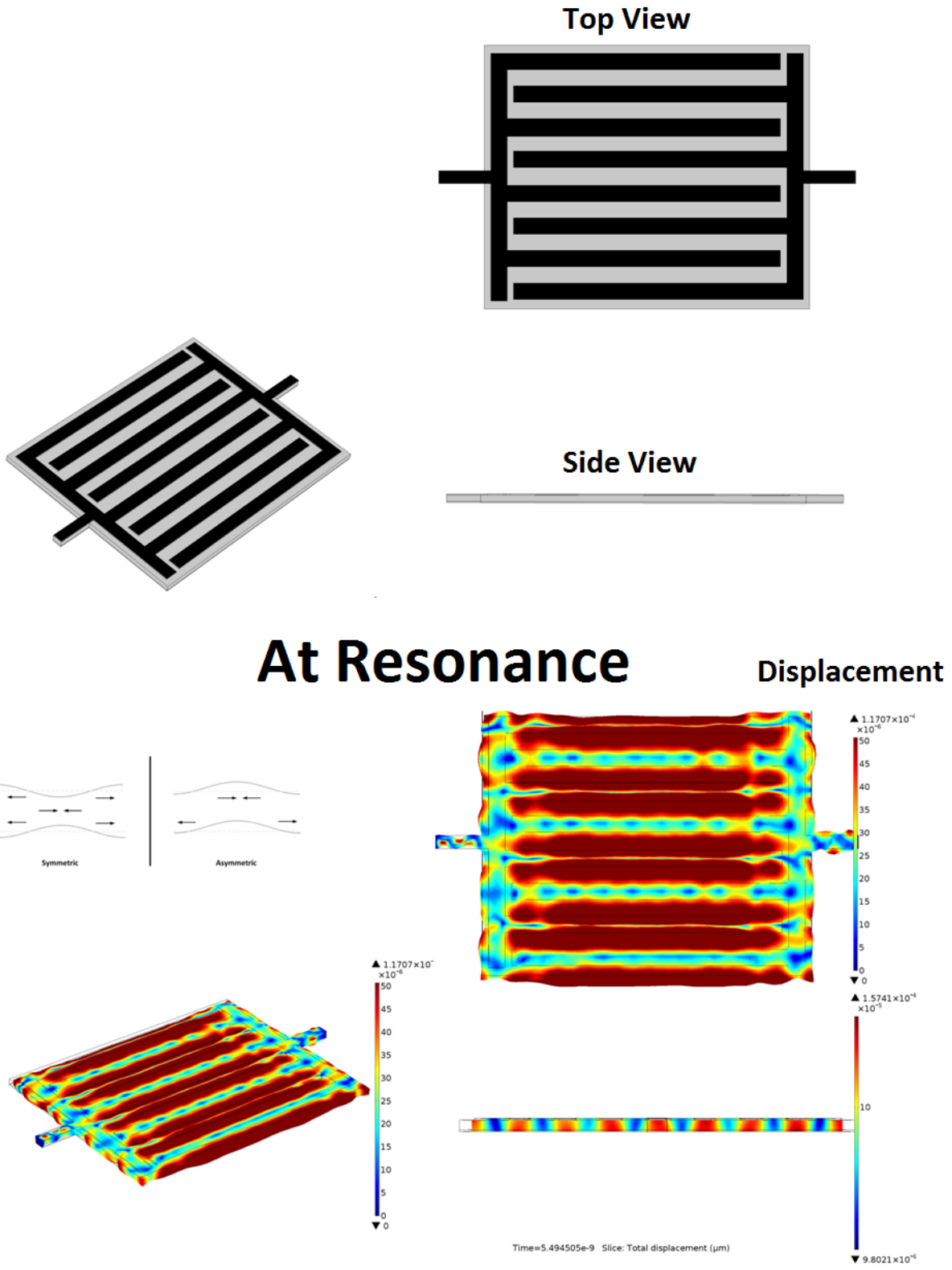


Figure 4.11: **LAMB Wave Device Simulation working principle**

# Bulk Acoustic Wave BAW



# At resonance

**Displacemenat**
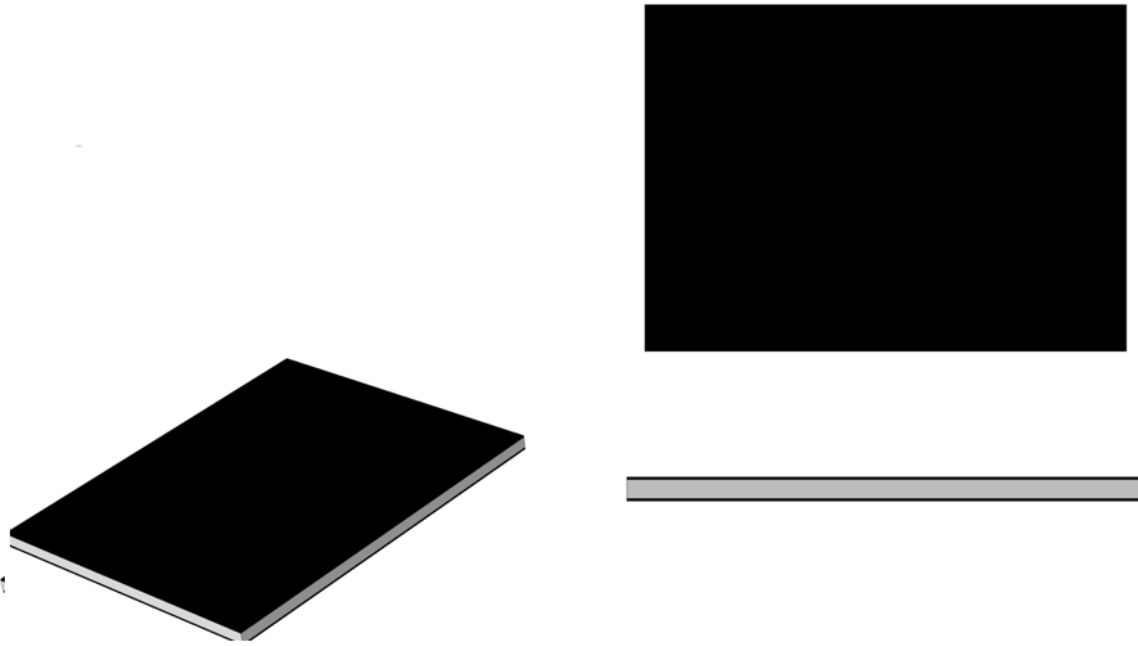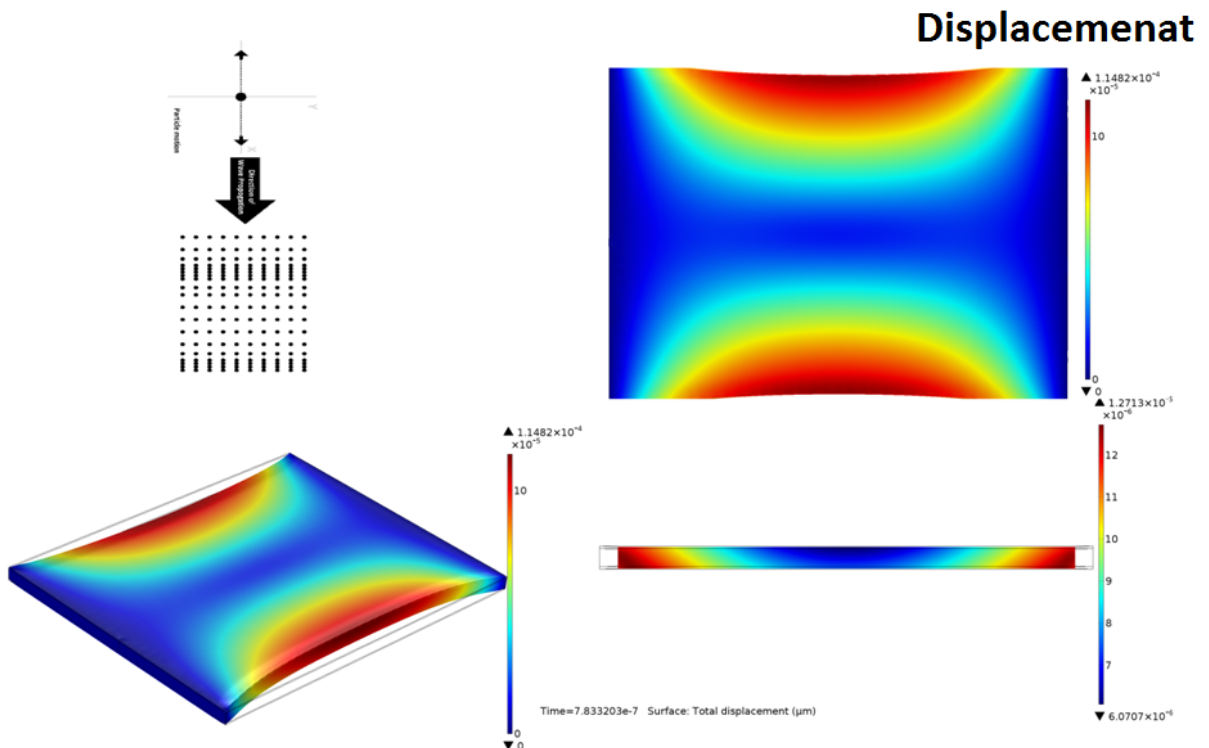


Figure 4.12:  **Bulk Acoustic Wave Device Simulation working principle**

## 4.3 Apodization

The design of piezo-acoustic devices like SAW, BAW or Lamb wave devices are quite similar to any other electronic filter. Since piezo acoustic filters are finite in their dimensions, unlike simulations, they exhibit a phenomenon known as Gibb's oscillations, which are ripples in the pass band and stop band [6, 50–54]. When a finite number of terms is used to approximate an infinite series, the signal exhibits oscillations, or ripples. The oscillations are compressed with an increase sampling value of N. A technique known as Apodization was developed to mitigate this.

Apodization means "without foot", it is a signal processing technique, also called a window function, where a mathematical function has a value of zero out of some chosen interval [52,55–57]. There are many types of window functions with differing results [58, 59]. Gibbs oscillations are a result of rectangular windows with its abrupt transition from high to low. The technique of apodization or windowing is used to mitigate this by using gradual transitions.

The relationship between the impulse response of a piezo-acoustic filter and it frequency response is given by the Fourier Transform pair

$$H(f) = \int_{-\infty}^{\infty} h(t)e^{-j2\pi ft}dt \tag{4.6}$$

$$h(t) = \int_{-\infty}^{\infty} H(f)e^{j2\pi ft}df \tag{4.7}$$

Where the impulse response h(t) and the frequency response H(f) are interchangeable. A series of common Fourier Transform pairs are given in Figure 4.14.
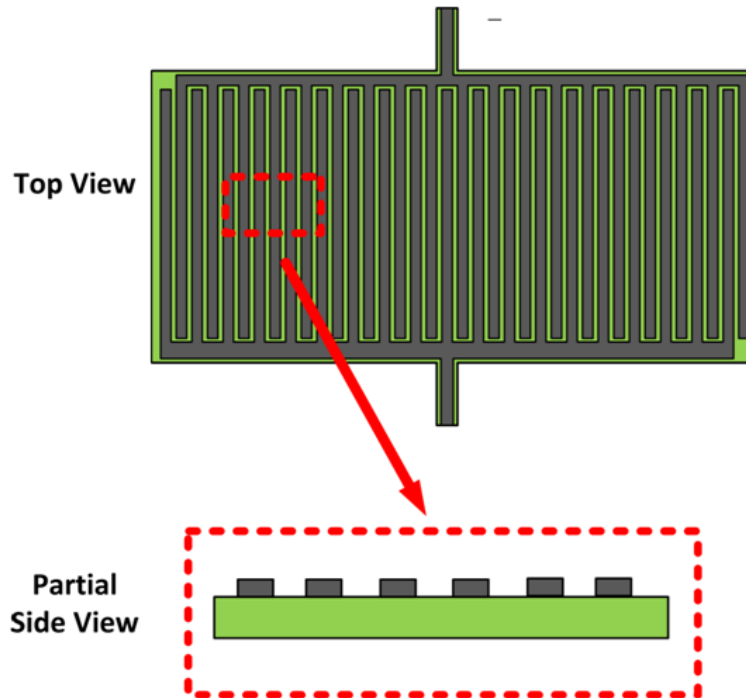


Figure 4.13: **Top And Side View of Piezo-Acoustic Resonator**

The electrodes in a acoustic-piezo devices can be designed by considering the fingers in terms of impulse decomposition as in digital signal processing. In impulse decomposition a signal of N samples is represented by a series of N sample impulses of N length with each impulse representing one point in that signal.
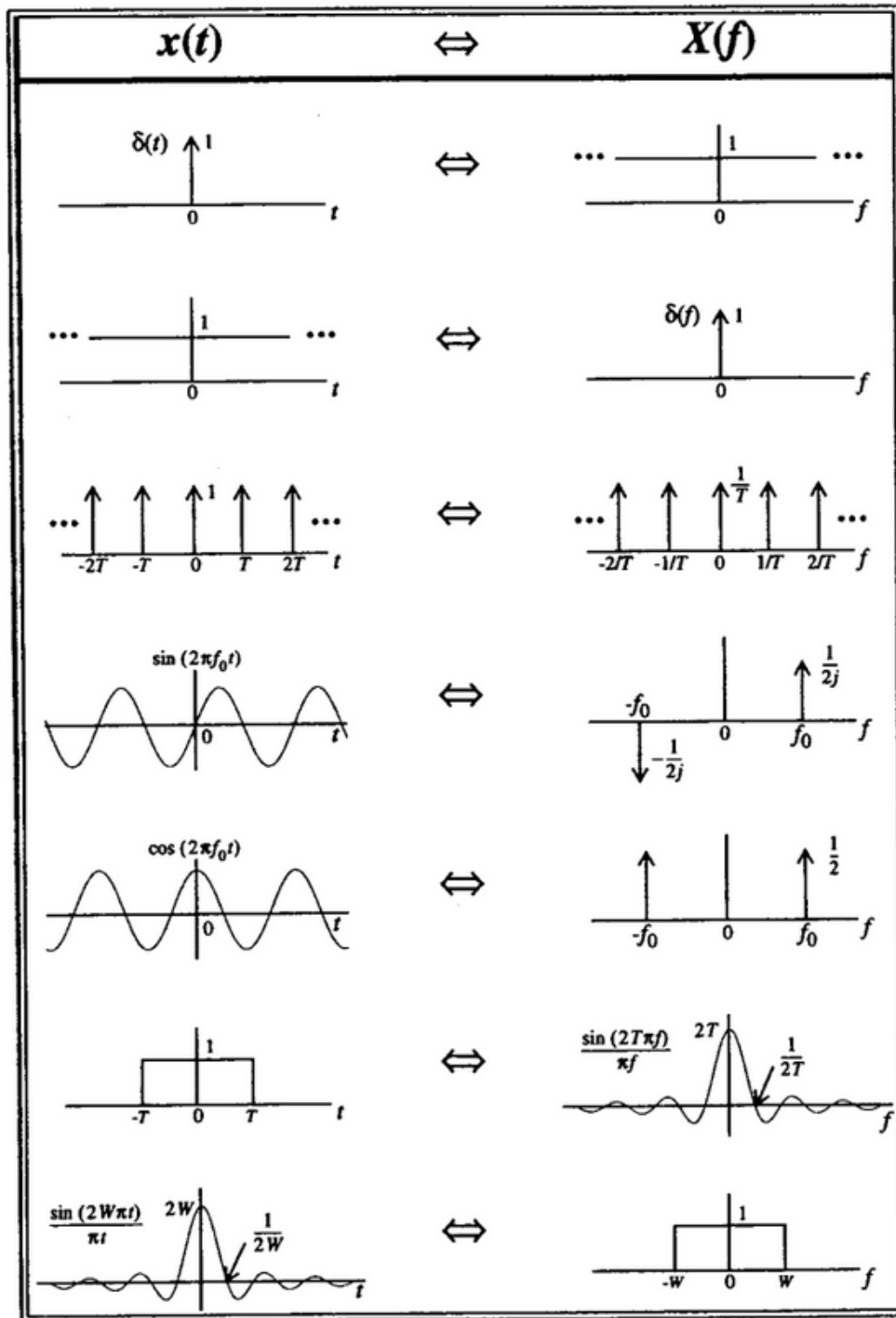
Figure 4.14: **Fourier Transform Pairs** [6]

To understand the process, take a portion of a typical piezo-acoustic resonator side-view as illustrated in Figure 4.13. It was realized by Tancrell, et al, in 1971 that the interdigitated fingers used to transduce a signal from electric to acoustic waves could be mapped in the form of an Impulse Response spatially in a geometric pattern with the overlap of the interdigitated fingers [60]. With the basic formula give as

$$h(t) = a(t)e^{j\phi t} \tag{4.8}$$

where a(t) is the time dependent amplitude response The interdigitated fingers can be represented as a series of dirac delta functions $\delta(t)$. If the physical sampling is done at the center of the device's finger overlap in a phase weighted condition, it will give the spatial location of the fingers, as shown in top and side views of two different interdigitated finger configurations Figure 4.15 and Figure 4.16.
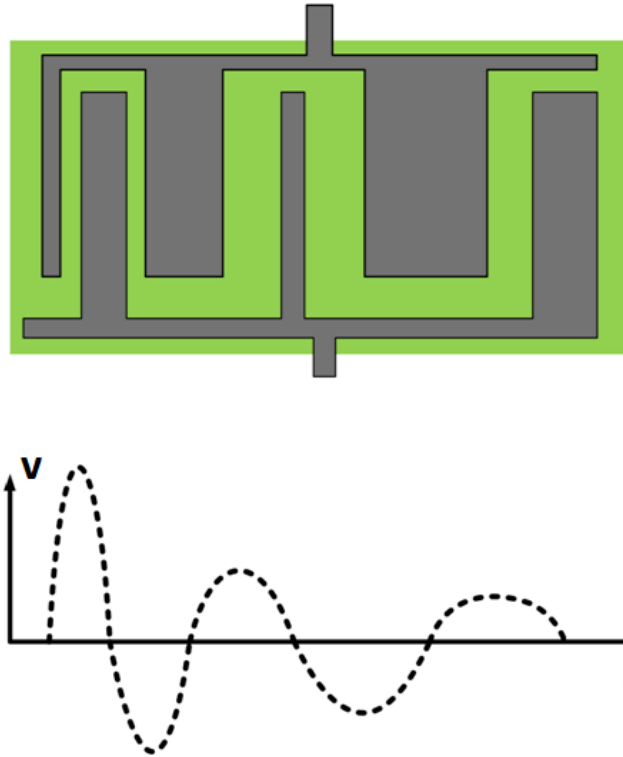


Figure 4.15: **Dirac Impulse Mapping Top View**
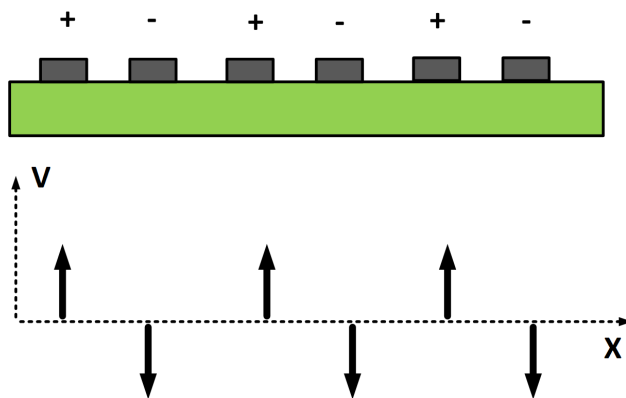


Figure 4.16: **Dirac Impulse Mapping Side View**

In an idealized model Figure 4.17 would be the frequency response of the IDT overlay; however this is based on Fourier Transforms which are assumed to extend into positive and negative infinity. In real

world applications the devices are bounded with time being position and frequency displacement, which results in Gibb's phenomenon of spurious oscillations. The technique of windowing is used to refine the response of the system.
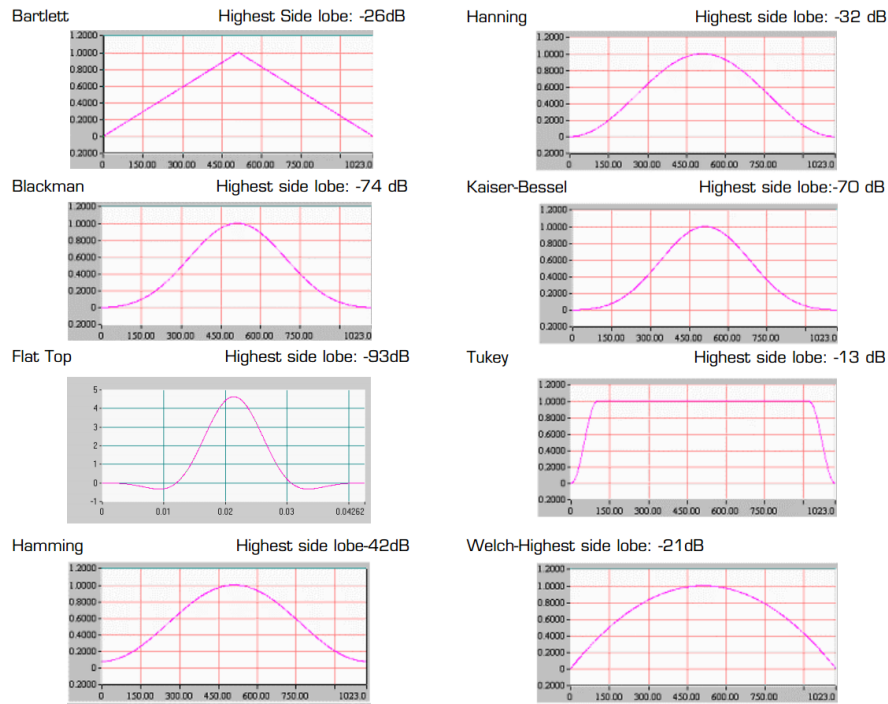


Figure 4.17: **Time Domain Window Shapes [7]**

Since the device, to exist, must have a finite dimension with truncated ends, it can be modeled as a Finite Impulse Response (FIR) system. In Figure 4.18 a convolution machine has been drawn to illustrate this conceptually.

To overcome the problem of Gibb's ripple phenomenon the impulse response h(n) is multiplied by a window function w(n) via a Fourier Series approach [61].

$$h_w(n) = w(n)h(n) \tag{4.9}$$

The Rectangular, Hanning window, and Hamming window can be expressed as such:

$$w(n) = \alpha + (1 - \alpha)cos\left(2\pi\frac{n}{N-1}\right) \ for \ 0 \le n \le N - 1; \ otherwise \ 0 \tag{4.10}$$

Where the coefficient $\alpha$ is 1, 0.5 amd 0.54 for the Rectangular, Hanning and Hamming windows respectively.

Window Functions have differing responses, depending on the desired roll off and bandwidth [62], refer to Table 4.1 and Figure 4.20 for a comparison of common window functions.
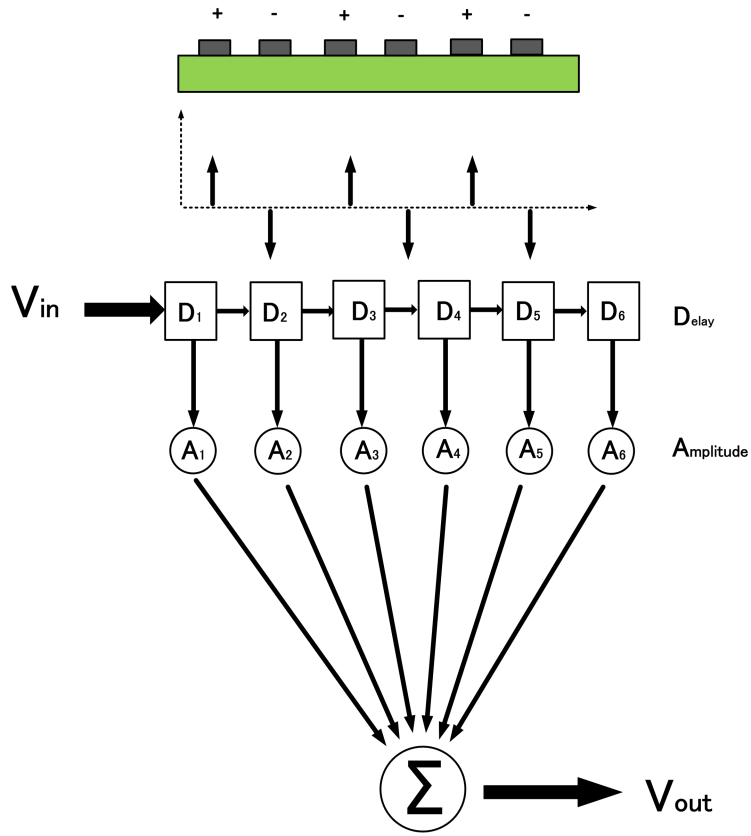
Figure 4.18: **convolution machine**

Table 4.1: **Window Functions Comparison**

| Window Function | Main lobe width | Side lobe height |
|---|---|---|
| Rectangular | 2/N | -14dB |
| Bartlett | 4/N | -25dB |
| Hanning | 4/N | -132dB |
| Hamming | 4/N | -44dB |

## Time domain

Leakage Factor: 9.14 %

## Frequency domain

| | |
|---|---|
| Rectangular | |
| Hamming | |
| Triangular | |
| Bartlett | |

**Main Lobe**

## Frequency domain

| | |
|---|---|
| Rectangular | |
| Hamming | |
| Triangular | |
| Bartlett | |

**Side Lobe**

39
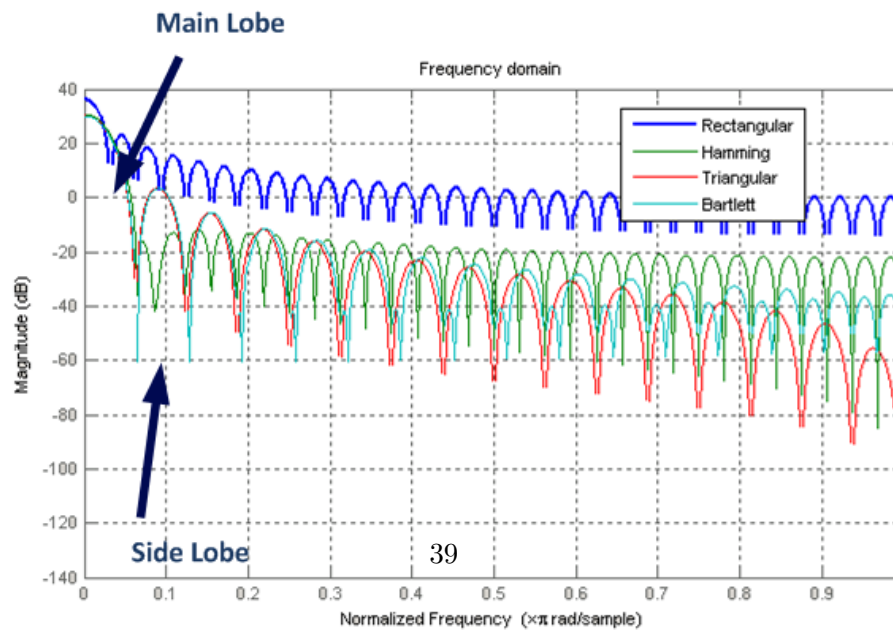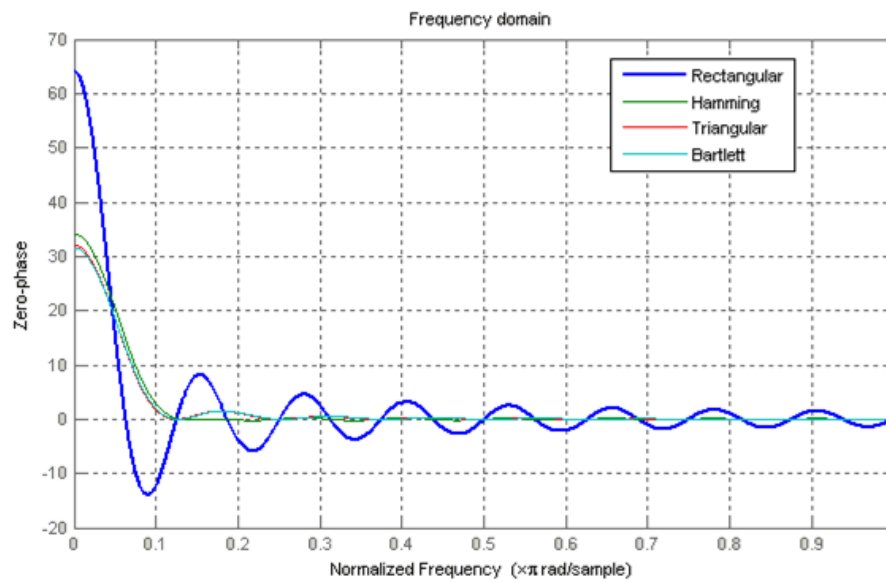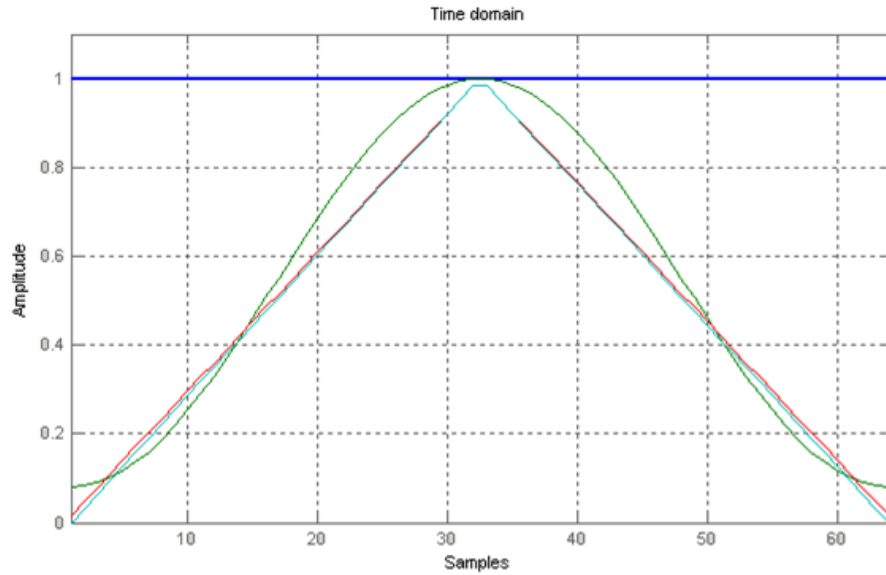
As shown in Figure 4.20 a uniform comb function h(t) is multiplied by a window function w(t) to reduce Gibb's oscillations. In Figure 4.21 a comparison of the uniform and Hamming window mode is given. There is a much lower second lobe in the frequency domain, however the width of the primary resonant frequency $f_0$ is wider. Different window functions will have differing effects on the expected output.



**Typical Comb configuration** • **Hamming Window** = **Hamming Window "Apodized" electrode**
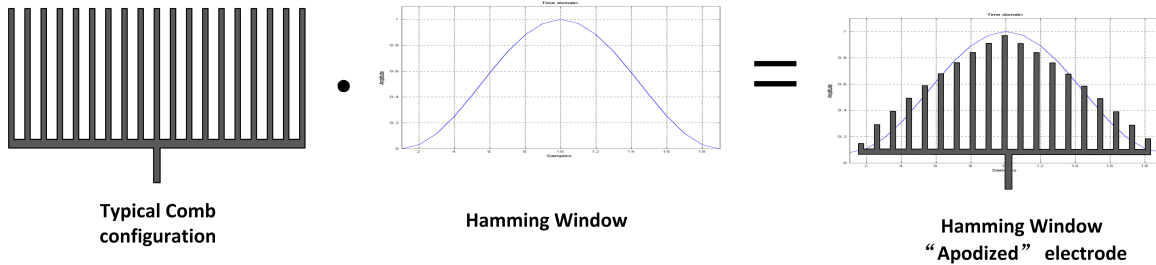
Figure 4.20: **Window Functions implementation**
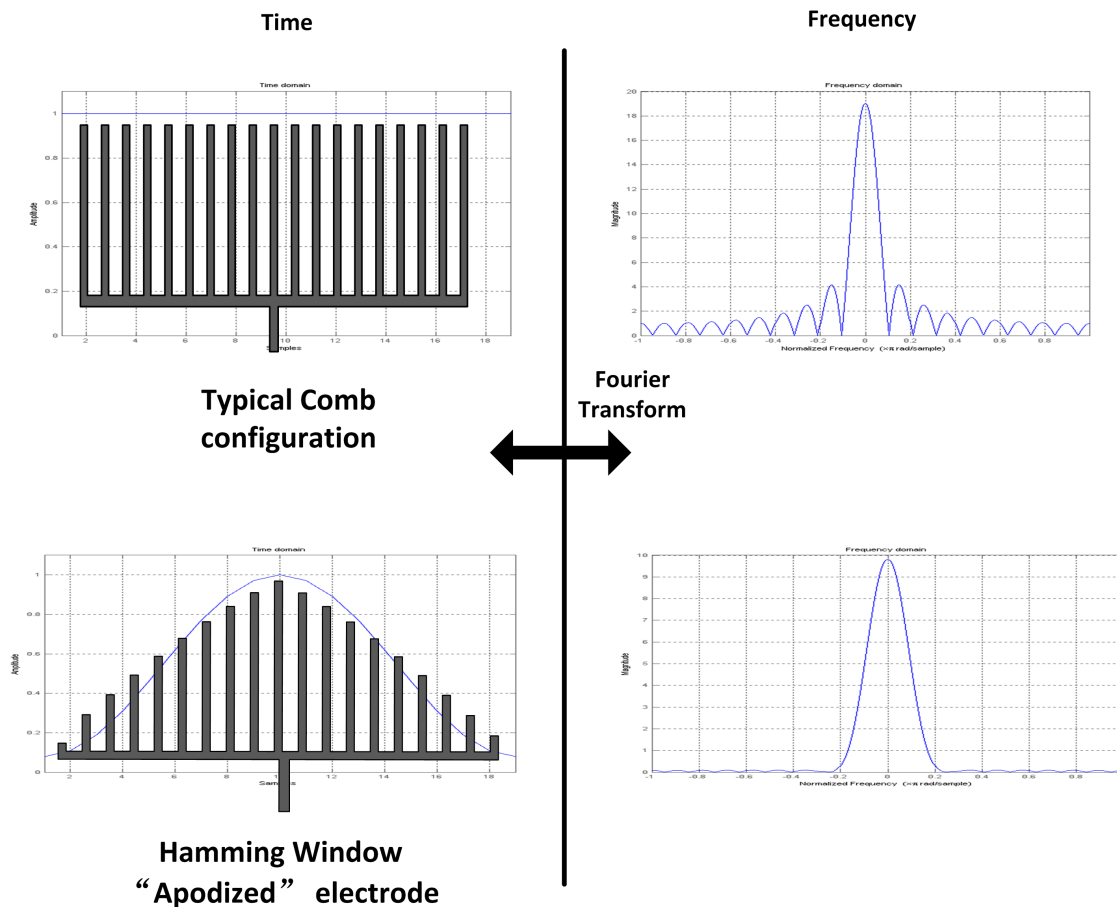


Figure 4.21: **Window Function Comparison**
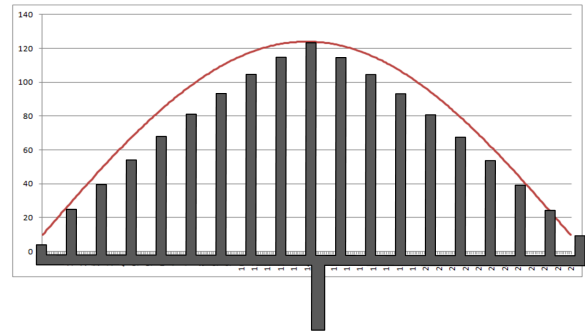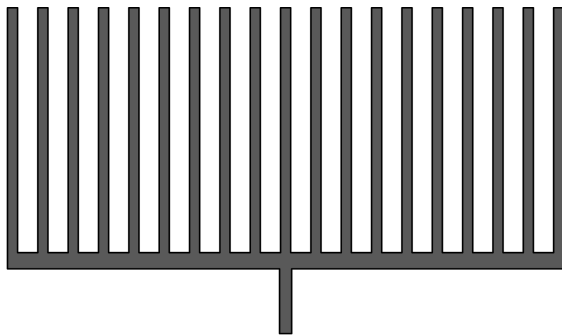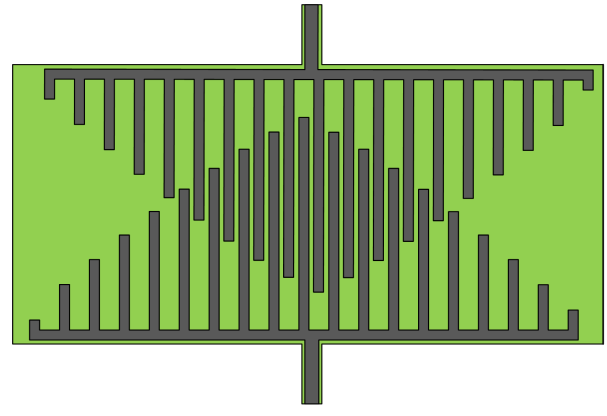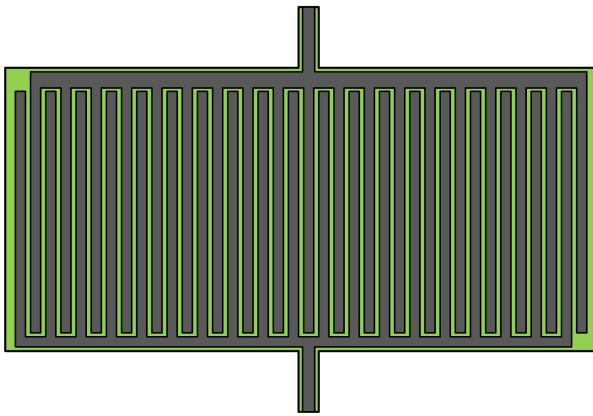
**Typical Comb
configuration**

**Apodized**

Figure 4.22: **Apodization**

Figure 4.22 is an illustration of apodization, this technique thus being used results in a change in the overall interference pattern created by the electrodes. The change in interference pattern has been simulated and is shown, at steady state displacement in Figure 4.23 and Figure 4.24, where A is the device at rest and B is the same device at its steady state displacement for that particular resonant frequency.
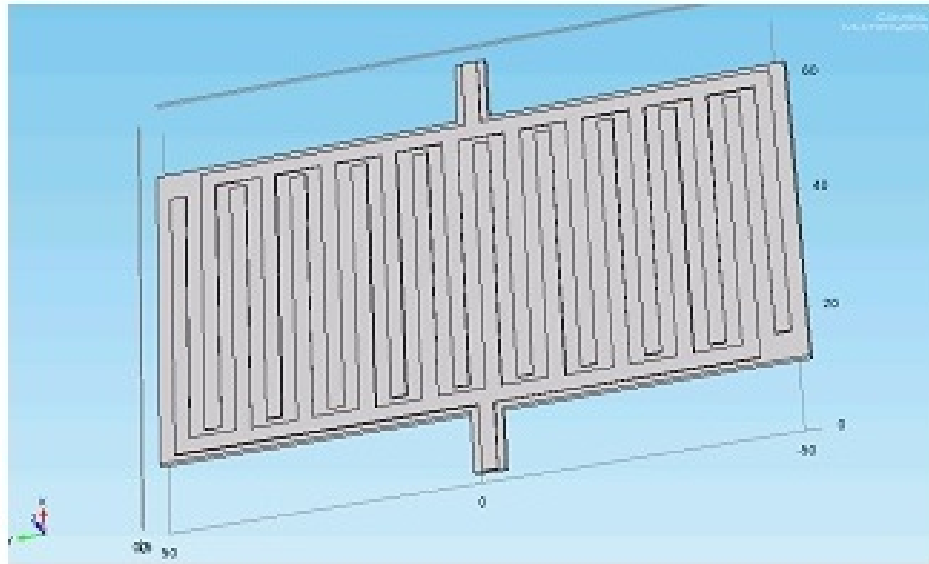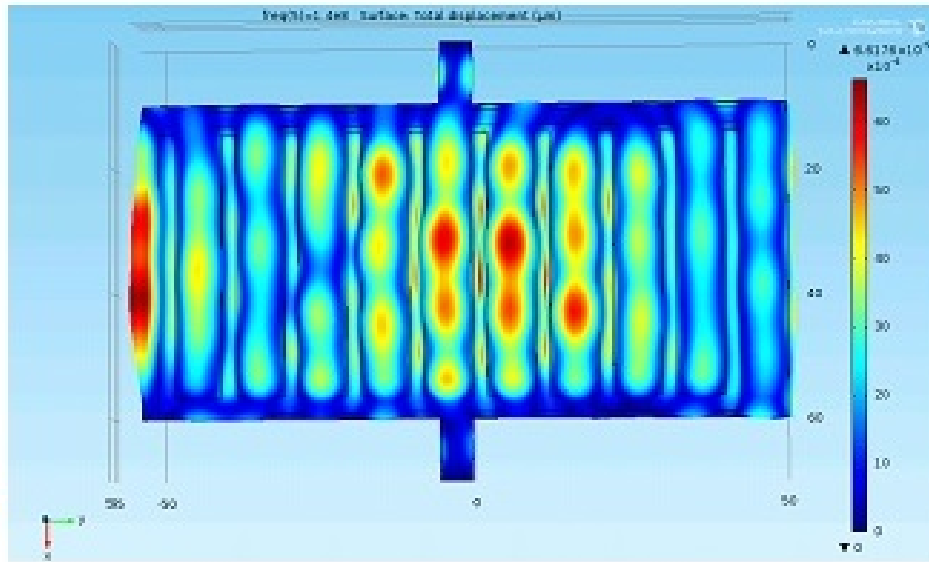
Figure 4.23: **Typical configuration**
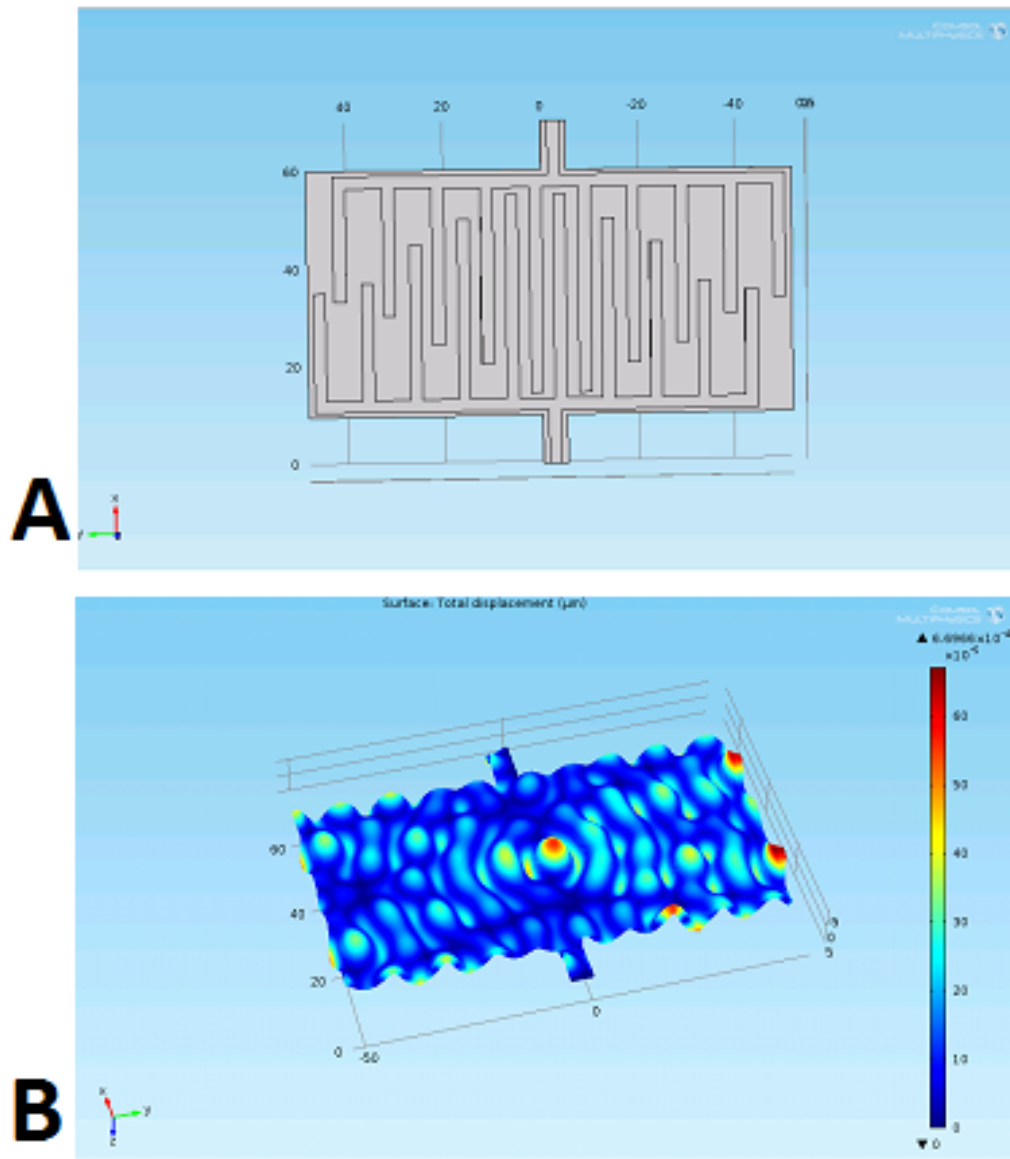
Figure 4.24: **Apodized Configuration**

# Chapter 5

# Process Flow

The construction of AlN MEMS resonators was accomplished through the development of a surface micromachined process. The devices being simulated as described in the design section above, where design in a mask editor IC station for comparison of theory with pragmatic results.

A top view is shown below in Figure 5.1 to orient the reader in regards to process flow pictures in the following pages. In CMOS the gate size is critical, however in piezo resonators the piezo film is critical, which necessitated a great deal of work on aluminum nitride deposition, which will be discussed below in the following section.
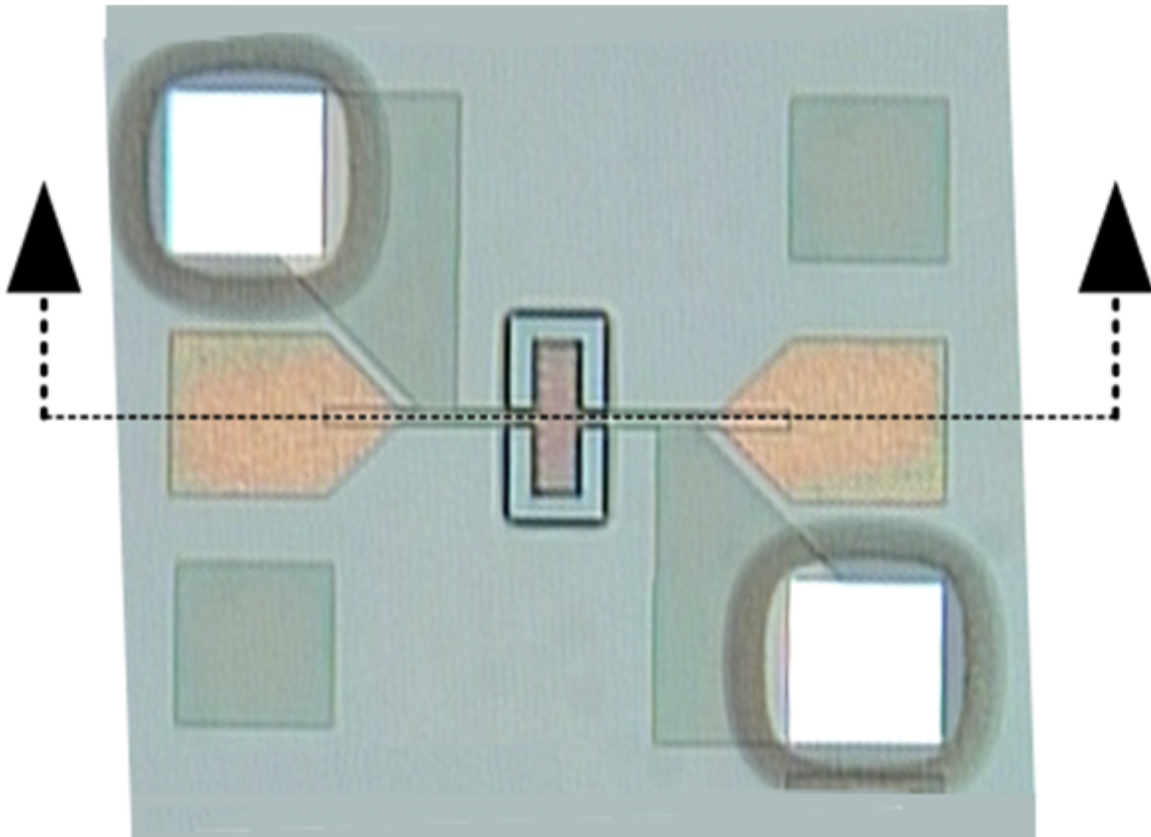


Figure 5.1: **RF MEMS Resonator Process Flow (Top View of Final Device)**
This top view is to orient the reader in regards to following process flow pictures drawn below

An RCA clean was done initially, followed by a layer of $2000\mathring{A}$ isolation oxide was grown to avoid shorting testing probes, or parasitic effects that may influence the results. A 250nm layer of molybdenum was deposited with a 601 CVC sputter at 1000W for 1000 seconds DC pulsed a 5 mTorr chamber pressure of Argon at 30sccm ,and masked with a photoresist, as shown in Figure 5.2.
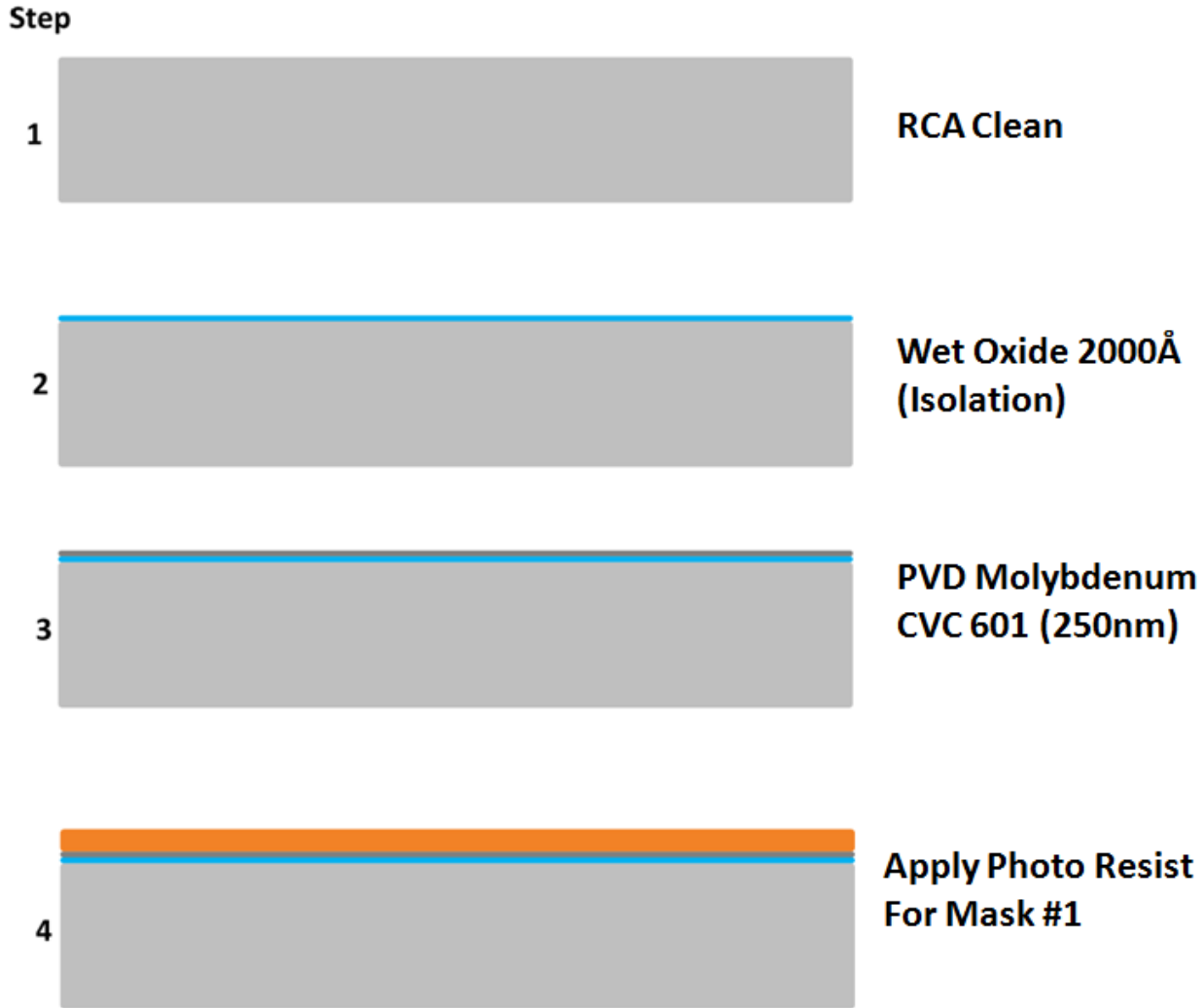


Figure 5.2: **Aluminum Nitride RF MEMS Resonator Process Flow 1**

The photoresist, mask level 1, was exposed and developed with an ASML 5500/200 Stepper, the bottom electrode, the exposed molybdenum was removed with a DryTek Quad RIE etch and resist stripped. The wafers were put into a Perkin Elmer 4400 and deposited with a 0.8 to 0.1 $\mu$m thick layer of polycrystalline aluminum nitride , as shown in Figure 5.3.
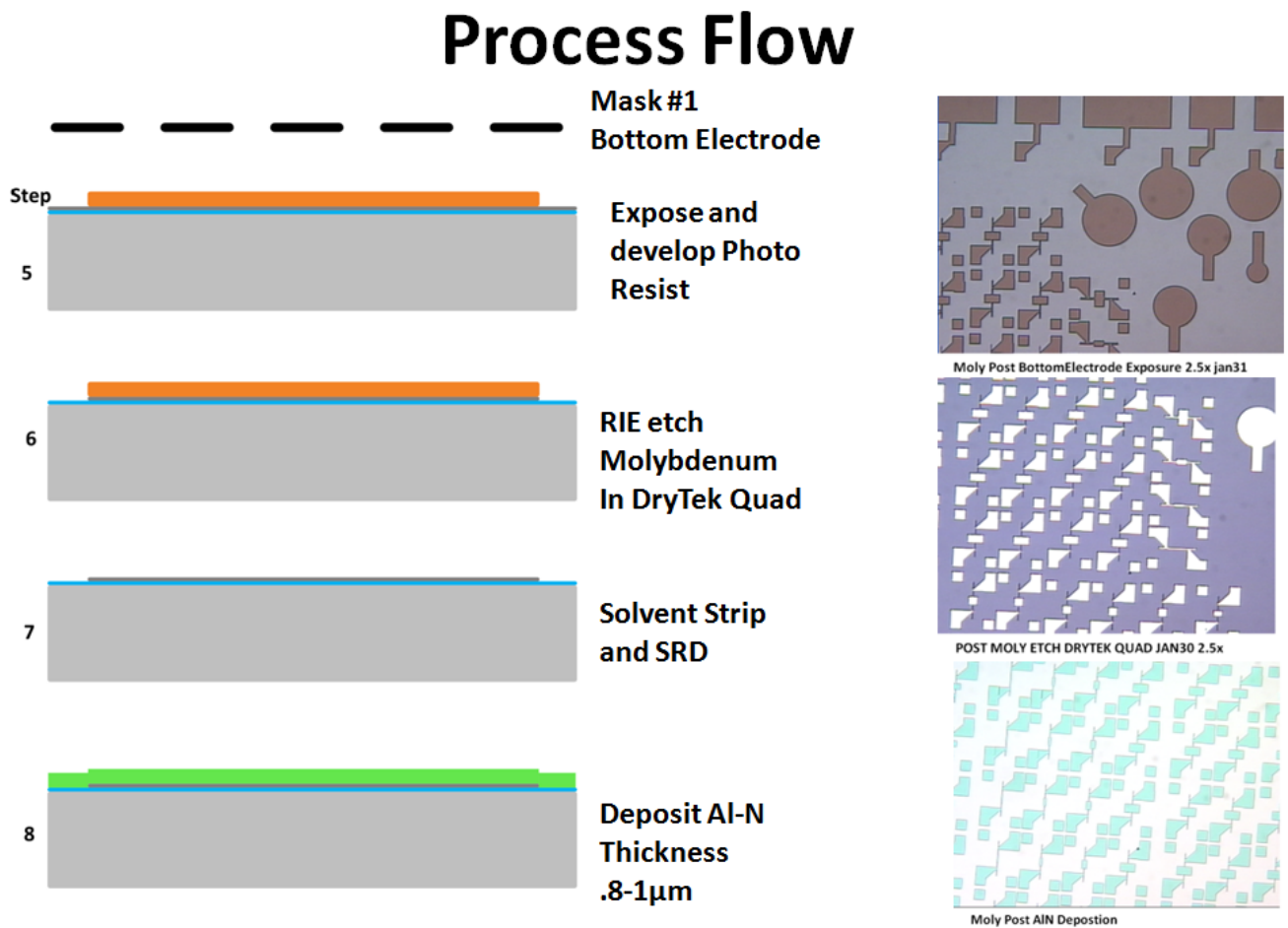


Figure 5.3:  **Aluminum Nitride RF MEMS Resonator Process Flow 2**

A resist is applied to the AlN, exposed with mask level 2, and etched in hot phosphoric acid at $90^{o}C$. The wet etch of phosphoric was over etched due to the high non uniformity of the AlN film. This was necessary in order to ensure all die's bottom electrode vias were fully cleared.The photo resist was stripped and the previous steps illustrated in Figure 5.4.
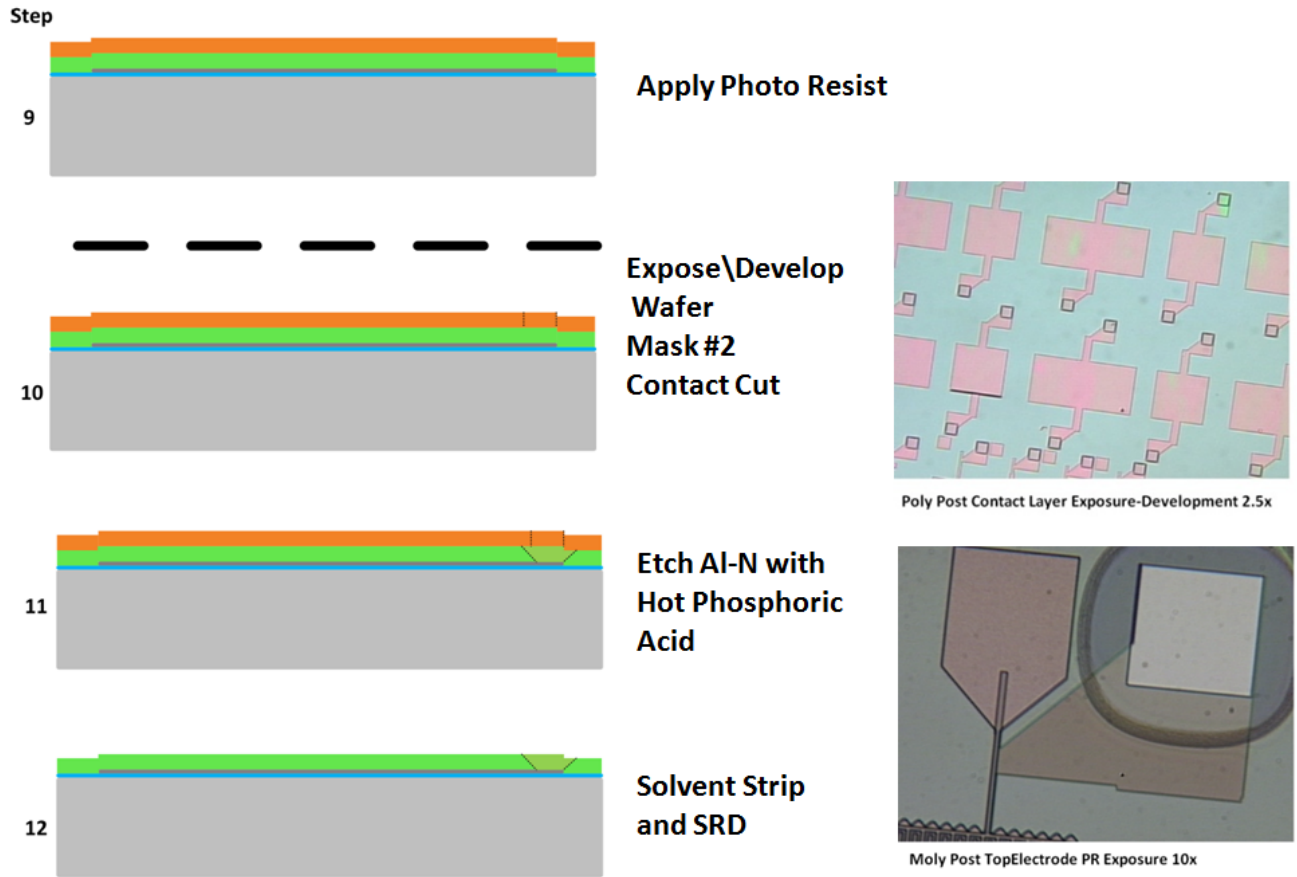


Figure 5.4: **Aluminum Nitride RF MEMS Resonator Process Flow 3**

Photoresist was applied for a lift off process, mask level 3 was exposed and a top 250nm aluminum layer was evaporated for the interdigitated fingers. The resist was stripped in an acetone bath, the steps are shown below in Figure 5.5.
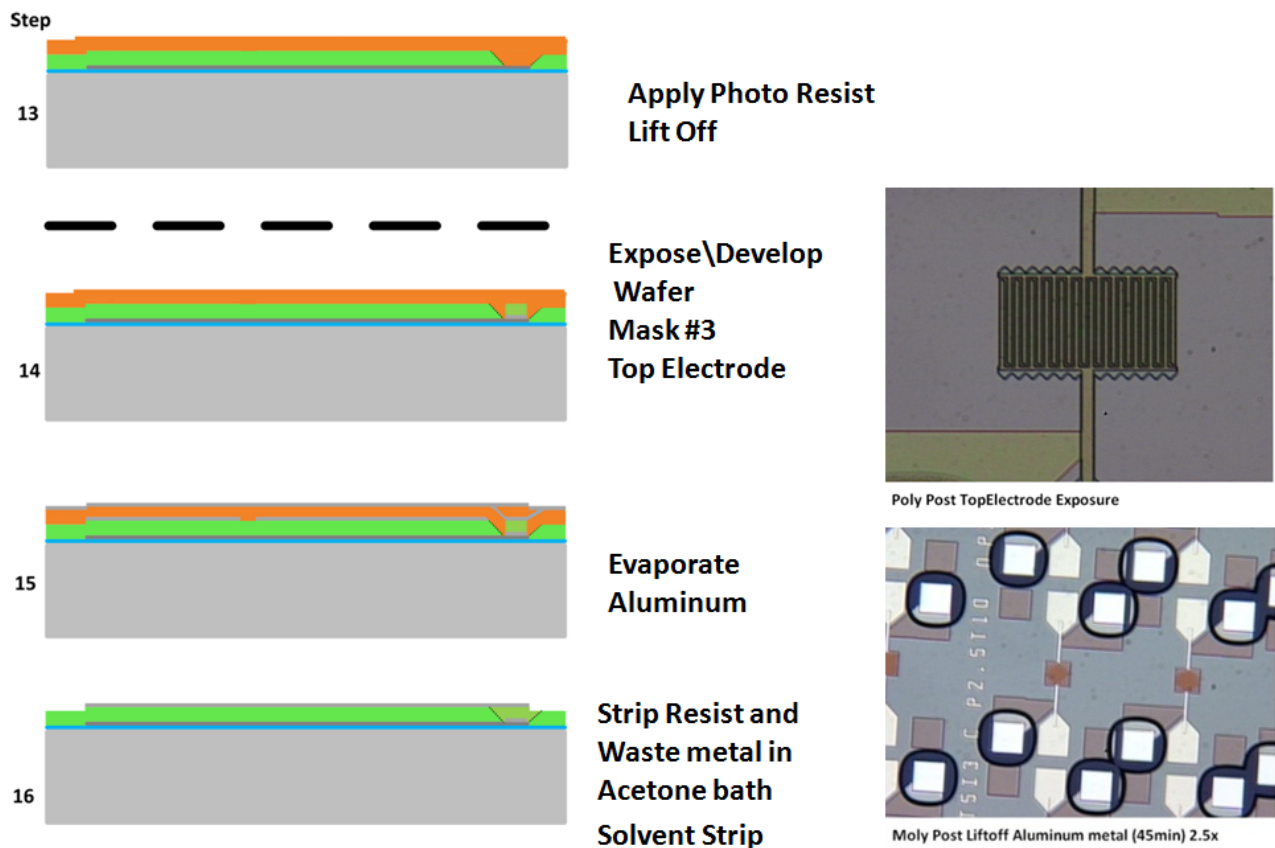


Figure 5.5: **Aluminum Nitride RF MEMS Resonator Process Flow 4**

Photoresist was applied and developed with mask 4 for the RF MEMS resonator boat, which is used later for the device release step. An aluminum RIE etch was used to etch the Aluminum nitride, but due to the faster etch rate of the photoresist relative to the aluminum nitride, this resulted in a repeating process were the mask level photo 4 photoresist was stripped, then reapplied exposed with mask level 4 and repeated until the aluminum nitride had been fully cleared, this is shown in Figure 5.6.
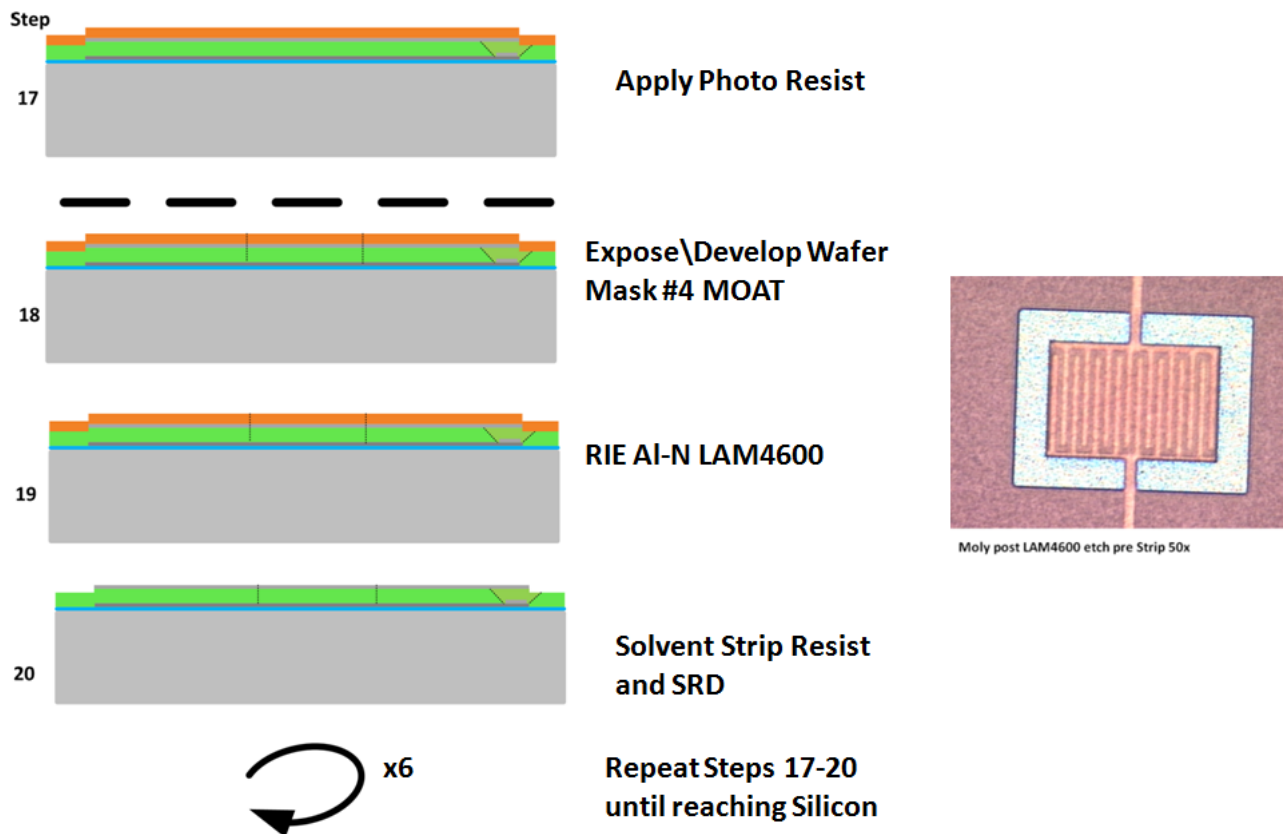


Figure 5.6:  **Aluminum Nitride RF MEMS Resonator Process Flow 5**

After the AlN was fully cleared the mask level 4 photoresist was again reapplied, to protect the devices during the wafer saw step and each individual die was released with $XeF_2$, which etched the substrate underneath the devices, following with the remaining resist ashed in Gasonics asher, Figure 5.7.

# Process Flow
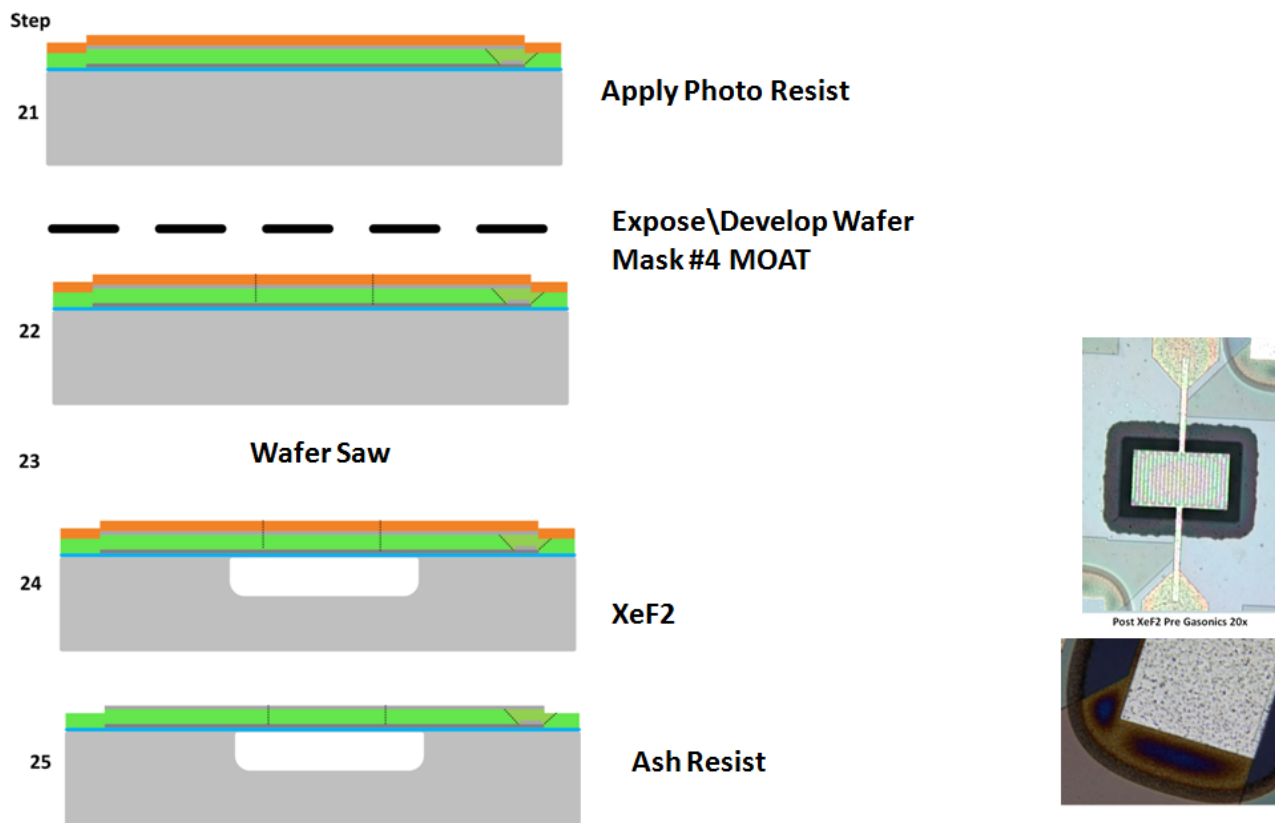


Figure 5.7: **Aluminum Nitride RF MEMS Resonator Process Flow 6**

# Chapter 6

# Experimental Results

Fabrication and testing of the AlN resonator was carried out in RIT's SMFL and Nanophotonics test facilities. Even though most process steps were readily available, as they are common to the baseline CMOS process of the facility, certain critical steps had to be developed. These include the deposition conditions of the piezolectric AlN film, the AlN etch, and resonator $XeF_2$ lift off via substrate etch, which required a series of experiments to determine the best means available to achieve the RF MEMS devices.

## 6.1 Aluminum Nitride Process Development

Aluminum nitride is the most critical step in piezo acoustic RF MEMS devices. In industry the films are controlled down to 10's of angstroms, as stated before in a baseline CMOS process the gate size is of critical importance, whereas in piezo acoustic MEMS, the thickness and crystal orientation of the film is of the utmost importance.

The first stage in development of the AlN resonators was the development of a process for aluminum nitride using RF Reactive Sputtering, to achieve the aluminum nitride film. The tool used was a Perkin Elmer 4400 sputtering system as shown in Figure 6.1. The chamber was pumped down overnight until reaching a minimum of 7.6E-7 Torr. The sputtering tool was fitted with an external RF power supply, with a maximum power capacity for 1000W, the RF used was 13.56 MHz.



Figure 6.1:  **Perkin Elmer 4400 Sputtering System**

The AlN process development was done iteratively to determine the most favorable conditions for the deposition of ⟨002⟩ oriented aluminum nitride. Over 50 experiments were done to determine the most optimal conditions. There were several parameters that could be manipulated in the tool. The pump-down chamber pressure, the flow rate of zrgon, the flow rate of nitrogen, the chamber pressure during the process, stationary or rotating wafer platen, power, and pre-sputter conditions.

## 6.2   Aluminum Nitride X ray Analysis Overview

X-ray 2-$\theta$ rocking curve analysis was done to test for the presence of aluminum nitride, to determine the film orientation and the type of film stress (compressive or tensile).

To understand the process development, an explanation of 2-$\theta$ rocking curve analysis is necessary.
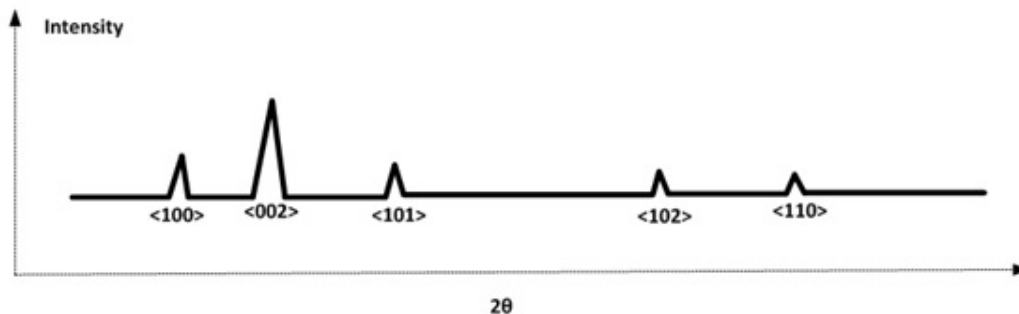


Figure 6.2:  **Major AlN peaks, in x-ray 2-$\theta$ rocking curve analysis there are a series of peaks that are associated with AlN**

X-ray 2-$\theta$ analysis was done on each sputtering run to determine the most favorable conditions for the deposition of ⟨002⟩ oriented AlN. X-ray 2-$\theta$ analysis is illustrated in Figure 6.3 where a sample is hit with an X-ray source and a detector sweeps the sample, the angles with the highest intensity can then be plotted against the detectors respective angle relative to the sample. Based on bragg diffraction due to parallel crystal planes, the materials, as well as the orientation of the crystals can be determined. Most material's crystal interplanar distance is known theoretically, if not experimentally, and a table of angles is used against the observed results to determine materials and orientation.
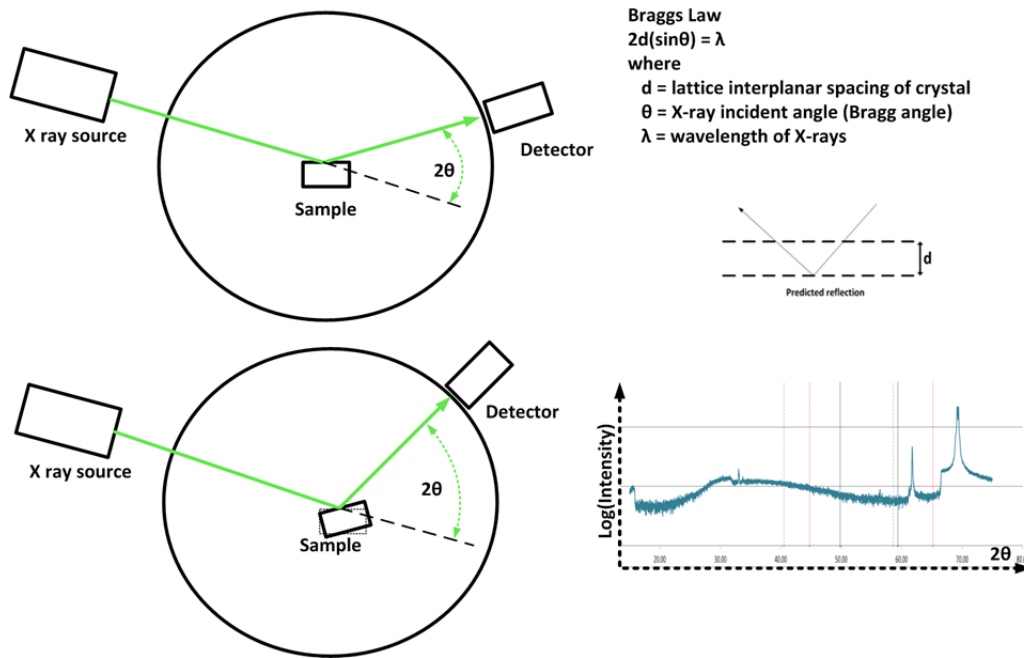
Figure 6.3: **X-ray 2-$\theta$ rocking curve system, in x-ray 2-$\theta$ analysis there are a series of peaks that are associated with AlN**

To begin the X-ray analysis several factors had to be consideed. The contribution of the silicon subtrate, of the glass slide, of the LOCTITE glue or the double sided tape all had to be individually analyzed to determine exactly what influence they had on the signal before testing any films. The first sample to be tested was bare silicon.
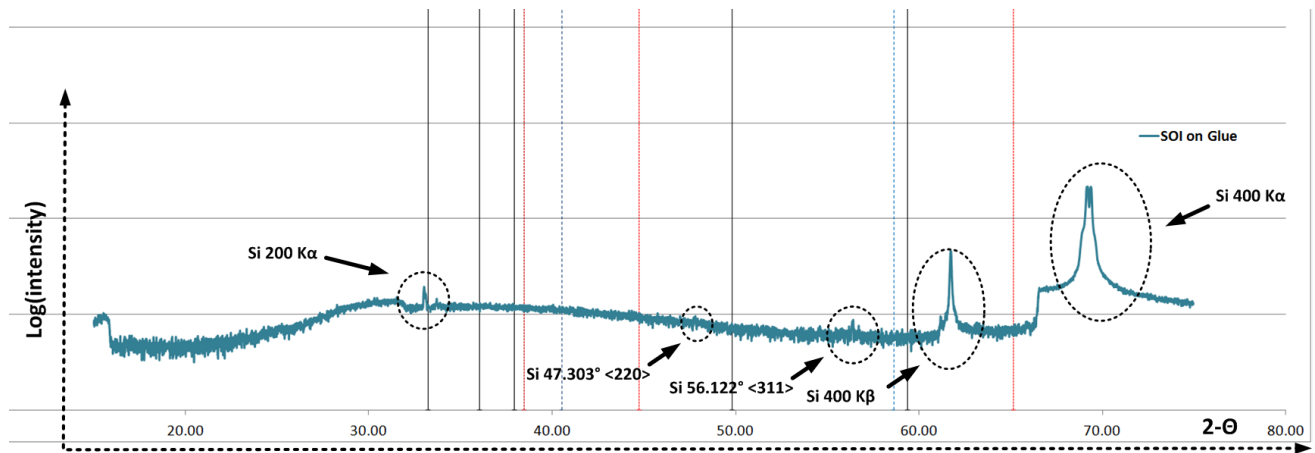


Figure 6.4: **Determining background signals inherent to the x-ray analysis silicon substrate**

The following are typical peaks associated with crystalline silicon, the silicon $200K\alpha$ is a special case that sometimes presents itself due to the distance between the planes of silicon and angle of the impinging X-ray. For the $200K\alpha$ the distance between the planes d becomes twice the 1.3577 $\dot{A}$ to become 2·d leading to $2.75154\dot{A}$ giving false positive plane distance d and a $2\theta$ angle of $32.96°$.
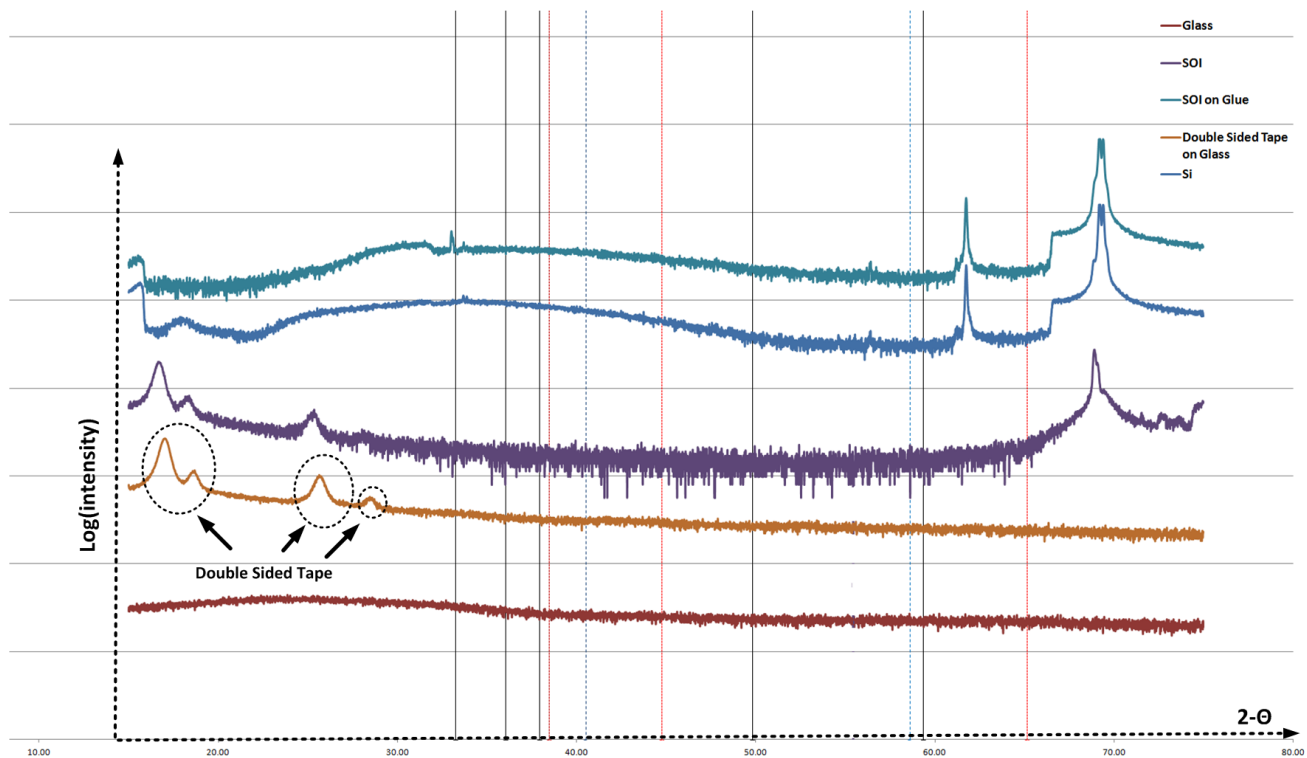


Figure 6.5: **Determining background signals inherent to the x-ray analysis glue, double sided tape, silicon on insulator and silicon substrate**

In Figure 6.6 the following are shown:(A)LOCTITE 495 glue used to stick sample to glass slide (B) VWR scientific glass slides used to hold the sample during X ray analysis (C) 3M scotch tape used to hold samples onto the glass slides (D) example of sample and glass slide
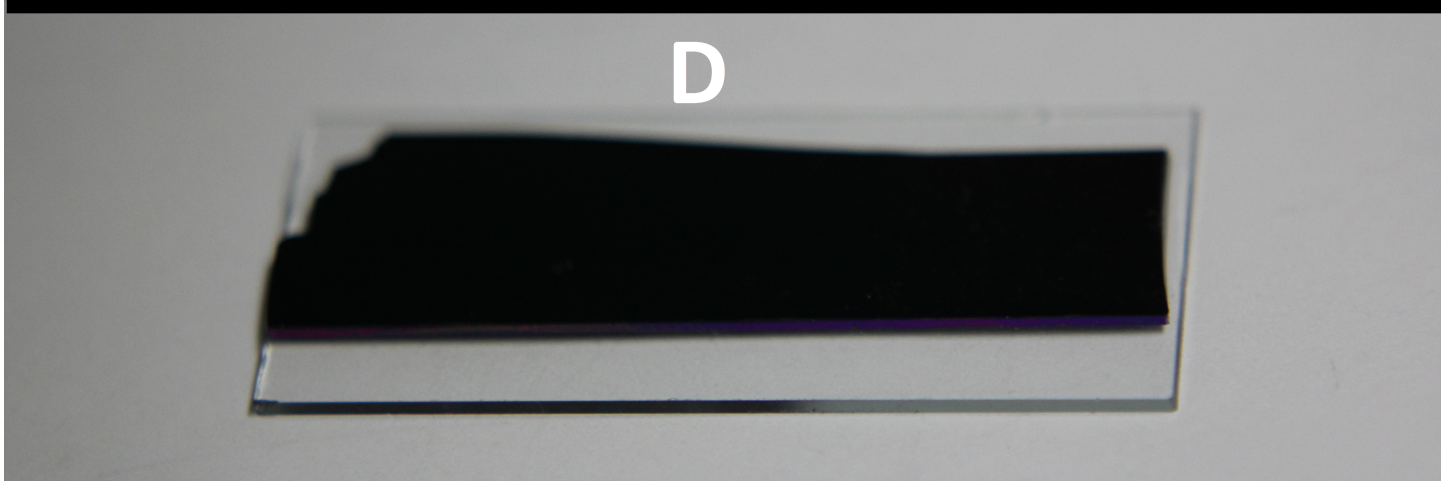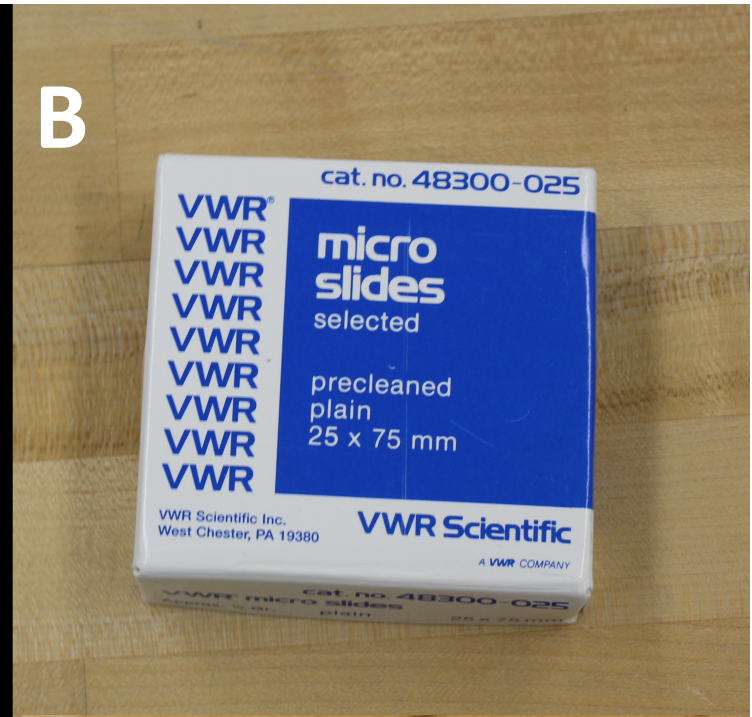
Figure 6.6: **Determining background signals due to sample materials**

## 6.3 Aluminum Nitride Process Development Experiment 1

During experiment 1 for determining the best deposition conditions, the aluminum target was poisoned. Poisoning is a result of a build up of product on the surface of the sputtering target resulting in a gradual increase in overall chamber or plasma impedance and if severe enough, it will lead to the inability to spark the chamber plasma [63, 64]. From Table 6.1 and Figure 6.7 there is no AlN peaks of any orientation for runs A through H. Table 6.1 show a series of depositions from A through H, where A-HF through F-HF represent an HF dip, which was used to remove any native oxide on the silicon substrate used for deposition, as this was thought to have some impact on the final AlN orientation. All future depositions have the 30 second HF dip. In experiment 1 the deposition duration, platen rotation, ratio of argon to nitrogen flow rate and chamber pressure were each changed to observe the effect on aluminum nitride deposition.

Following the discovery of target poisoning, a procedure was developed to clean the target after every AlN deposition with a half an hour run of the chamber with only argon, this was developed by performing a series of runs where a deposition of the aluminum target's sheet resistance, with a CDE Res Map, was measured after each argon only deposition (which is a kind of 'etch' of the target) until it returned to the baseline.

Table 6.1: **Aluminum Nitride Deposition Parameters For Experiment 1**

| Sample | Power [W] | Chamber Pressure [mT] | Argon Flow Rate [Sccm] | Nitrogen Flow Rate [Sccm] | Rotation [3 Rpm] | Deposition Duration [min] |
|---|---|---|---|---|---|---|
| A | 500 | 10 | 30 | 15 | Yes | 60 |
| A-HF | 500 | 10 | 30 | 15 | Yes | 60 |
| B | 500 | 10 | 30 | 15 | Yes | 60 |
| B-HF | 500 | 10 | 30 | 15 | Yes | 60 |
| C | 500 | 10 | 30 | 15 | No | 45 |
| C-HF | 500 | 10 | 30 | 15 | No | 45 |
| D | 500 | 10 | 30 | 15 | No | 30 |
| D-HF | 500 | 10 | 30 | 15 | No | 30 |
| E | 500 | 10 | 30 | 15 | No | 30 |
| E-HF | 500 | 10 | 30 | 20 | No | 30 |
| F-HF | 500 | 10 | 30 | 10 | No | 60 |
| G | 500 | 10 | 30 | 15 | No | 60 |
| H | 300 | 3 | 30 | 15 | No | 30 |
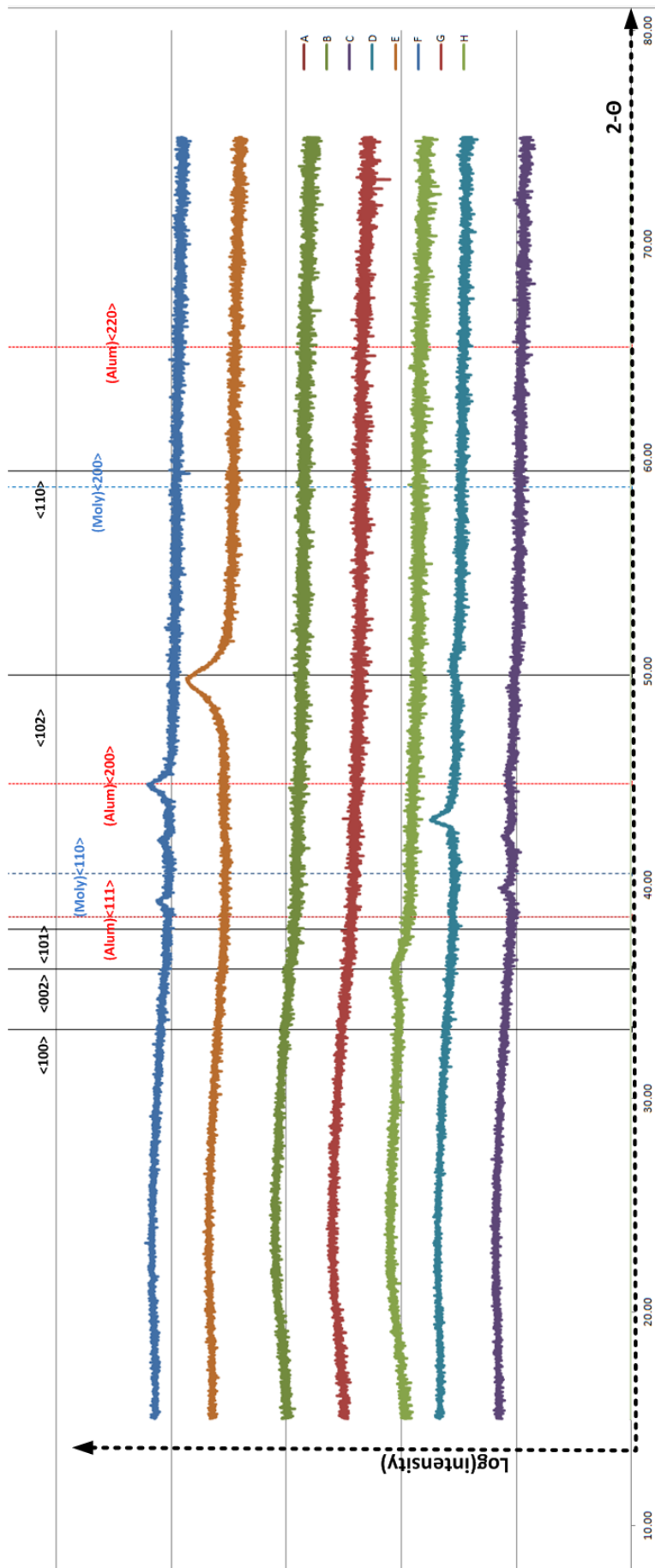
Figure 6.7: **Aluminum Nitride Process Development Experiment 1 Comparison**

## 6.4 Aluminum Nitride Process Development Experiment 2

A series of experiments, runs E through M2, were performed to determine the best parameters for RF reactive sputtering of aluminum nitride. The deposition parameters are listed in Table 6.2 and the X ray $2\theta$ rocking data in Figure 6.8. Due to the very slow deposition speeds found in experiment 1, all future runs were done stationary with an unavoidable non uniformity. The power was changed from in a stepwise fashion from 300 to 400 to 500 watts with experiments in the flow rate ratio of argon and nitrogen, as well as the chamber pressure. The results of this experiment did show several aluminum nitride peaks, however they were not the target. The strongest $\langle 101 \rangle$ peak was found in GHF2 and M.

Table 6.2: **Aluminum Nitride Deposition Parameters For Experiment 2**

| Sample | Power [W] | Chamber Pressure [mT] | Argon Flow Rate [Sccm] | Nitrogen Flow Rate [Sccm] | Rotation [3 RPM] | Deposition Duration [min] |
|--------|-----------|-----------------------|------------------------|---------------------------|------------------|---------------------------|
| E | 500 | 10 | 30 | 20 | No | 30 |
| F1 | 500 | 10 | 30 | 10 | No | 30 |
| F2 | 500 | 10 | 30 | 10 | No | 30 |
| GHF2 | 500 | 3 | 30 | 15 | No | 30 |
| GHF | 500 | 10 | 30 | 15 | No | 60 |
| HHF | 300 | 10 | 30 | 15 | No | 30 |
| I | 400 | 10 | 30 | 15 | No | 30 |
| J | 500 | 5 | 30 | 15 | No | 30 |
| K | 500 | 10 | 30 | 15 | No | 30 |
| L | 500 | 10 | 30 | 15 | No | 30 |
| M1 | 500 | 10 | 30 | 10 | No | 30 |
| M2 | 500 | 10 | 30 | 10 | No | 30 |
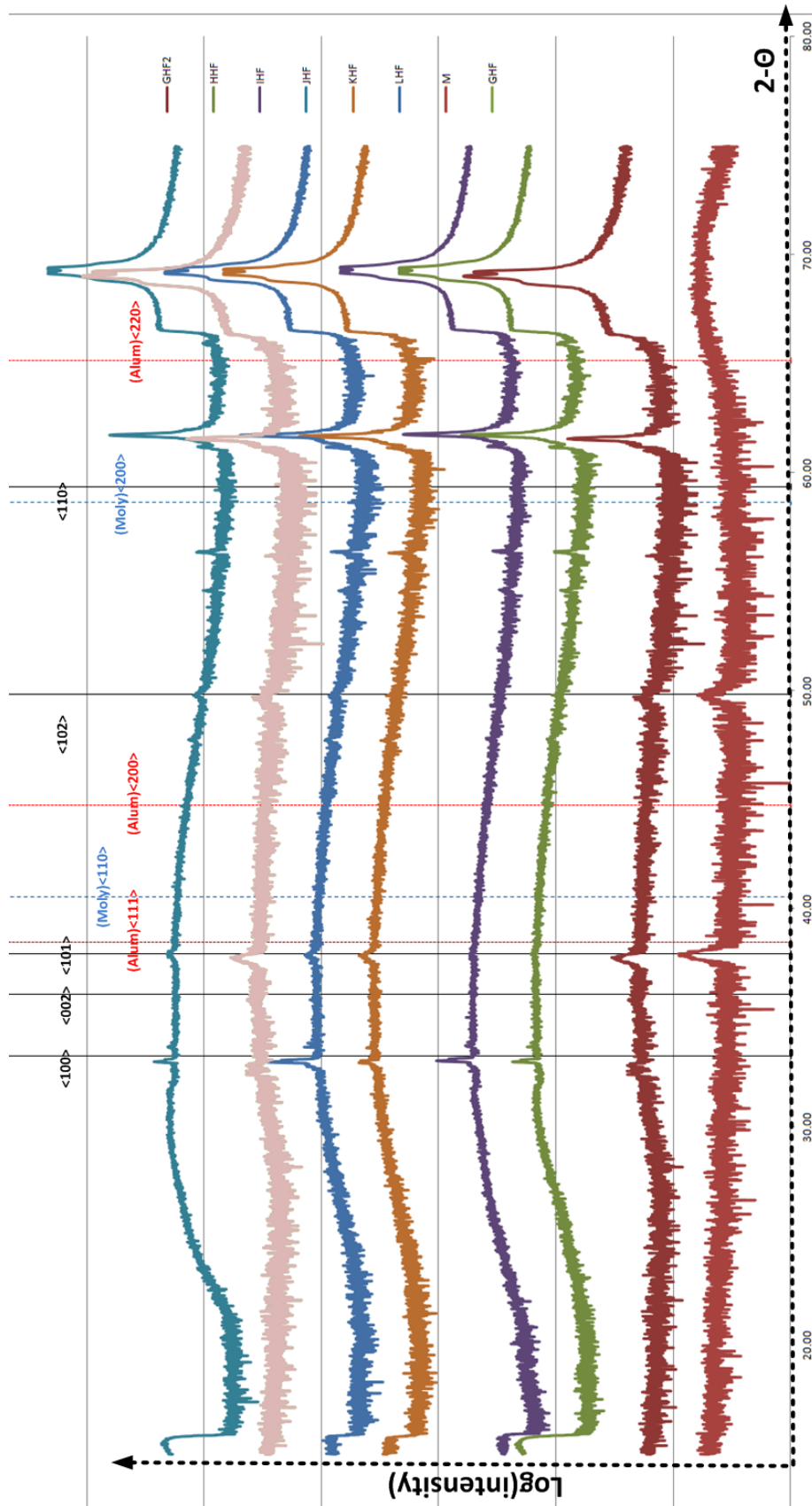
Figure 6.8: **Aluminum Nitride Process Development X ray Analysis of RF Reactive Sputtering Parameters For Experiment 2 Comparison 1**

Table 6.3: **Aluminum Nitride Deposition Experiment 3 X ray Intensity Ratios**

| Intensity Ratio | MM | R | T | V | W | X | Y | YY |
|---|---|---|---|---|---|---|---|---|
| $\langle 002 \rangle / \langle 101 \rangle$ | 3.04 | 1.17 | 1.27 | 1.35 | 1.10 | 2.61 | 0.85 | 2.14 |
| $\langle 002 \rangle / \langle 102 \rangle$ | 8.16 | 3.37 | 3.24 | 3.64 | 2.41 | 9.08 | 2.76 | 21.5 |
| $\langle 002 \rangle / \langle 110 \rangle$ | 19.44 | 7.26 | 6.78 | 8.17 | 9.00 | 23.08 | 5.59 | 64.5 |
| $\langle 002 \rangle / \langle 100 \rangle$ | 3.88 | 0.98 | 1.30 | 1.25 | 1.34 | 2.32 | 1.10 | 1.65 |
| Intensity Ratio | Z | AA | LL | O | S | SS | ZZ | |
| $\langle 002 \rangle / \langle 101 \rangle$ | 1.32 | 1.12 | 4.00 | 2.59 | 2.90 | 2.14 | 100.04 | |
| $\langle 002 \rangle / \langle 102 \rangle$ | 2.21 | 3.55 | 15.42 | 1.15 | 6.30 | 5.96 | 318.41 | |
| $\langle 002 \rangle / \langle 110 \rangle$ | 5.70 | 7.66 | 29.06 | 1.84 | 21.04 | 17.09 | 688.65 | |
| $\langle 002 \rangle / \langle 100 \rangle$ | 1.33 | 0.83 | 3.67 | 4.12 | 2.78 | 2.70 | 110.91 | |

## 6.5 Aluminum Nitride Process Development Experiment 3

A series of aluminum nitride depositions were run to determine the best parameters for $\langle 002 \rangle$ wurtzite orientation. Power, pressure, distance to the target and substrate were used as inputs for the experiment. Two metals were used as a surface layer for Al-N deposition, including molybdenum and aluminum. Each run was followed by a 30 minute post deposition clean to prevent target poisoning, by formation of Al-N buildup on the center of the aluminum target. The deposition was achieved by RF reactive ion sputtering, with a pre-deposition period of 10 minutes. The pre-sputter was done by starting with a high chamber pressure of 10mT then after 1 min to 5mT and finally the target pressure of 3mT. The power was gradually changed to the target power by starting at 1000W and gradually lowering the power over time to allow the power supply to automatically adjust to the impedance value of the plasma after it had settled. The parameters are listed in Table 6.4 and Figure 6.9 as well as the X ray intensity ratios which are used to compare settings for the most favorable conditions for the deposition of $\langle 002 \rangle$ Table 6.3.

Table 6.4: **Aluminum Nitride Deposition Parameters For Experiment 3**

| Sample | Power [W] | Chamber Pressure [mT] | Argon Flow Rate [Sccm] | Nitrogen Flow Rate [Sccm] | Rotation [3 RPM] | Deposition Duration [min] | 1cm path reduction | Metal Seed Layer [2000 $\mathring{A}$] |
|--------|-----------|----------|----------|----------|-----|-----|-----|------|
| MM | 1000 | 3 | 30 | 15 | No | 30 | Yes | Moly |
| LL | 1000 | 3 | 30 | 15 | No | 30 | No | Moly |
| NN | 500 | 1 | 30 | 15 | No | 30 | No | - |
| O | 1000 | 3 | 30 | 15 | No | 30 | Yes | - |
| R | 1000 | 3 | 30 | 15 | No | 30 | Yes | Alum |
| SS | 1000 | 3 | 30 | 15 | No | 30 | No | Alum |
| S | 500 | 5 | 30 | 15 | No | 30 | No | Moly |
| T | 500 | 3 | 30 | 15 | No | 30 | Yes | Moly |
| V | 500 | 3 | 30 | 15 | No | 30 | No | Moly |
| W | 500 | 3 | 30 | 15 | No | 30 | Yes | - |
| X | 500 | 3 | 30 | 15 | No | 30 | No | - |
| Y | 500 | 5 | 30 | 15 | No | 30 | Yes | Moly |
| Z | 1000 | 3 | 30 | 15 | No | 30 | No | - |
| AA | 500 | 3 | 30 | 15 | No | 30 | Yes | - |
| ZZ | 1000 | 3 | 30 | 15 | No | 30 | No | - |
| YY | 500 | 3 | 30 | 15 | No | 30 | No | None |
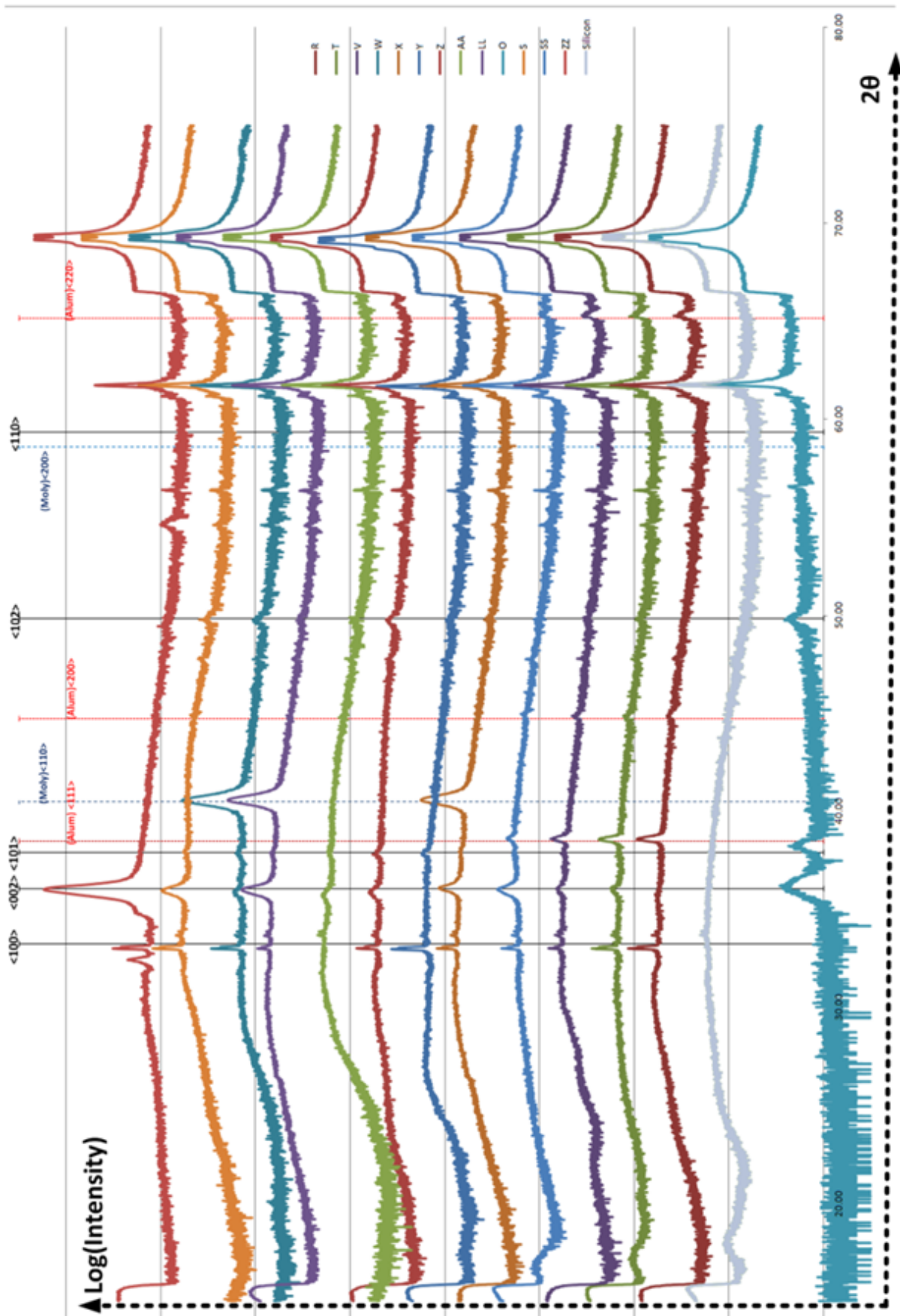
Figure 6.9: **Aluminum Nitride Process Development Full Comparison Experiment 3**

**Aluminum Seed Layer 2000 $\mathring{A}$**

The aluminum experiment in Figure 6.10, shows a $\langle 111 \rangle$, $\langle 200 \rangle$ and $\langle 220 \rangle$ aluminum crystal peak. Two powers (500W and 1000W) were run, a height experiment was also performed with a 1cm metal plate added below the substrate to decrease the height to the target during deposition. sample SS with a power of 1000W showed the strongest Al-N $\langle 002 \rangle$ peak relative to the $\langle 110 \rangle$ and $\langle 102 \rangle$ peaks, followed by Sample V (500W), R(500W -1cm) and T(500W +1cm) with the smallest response.
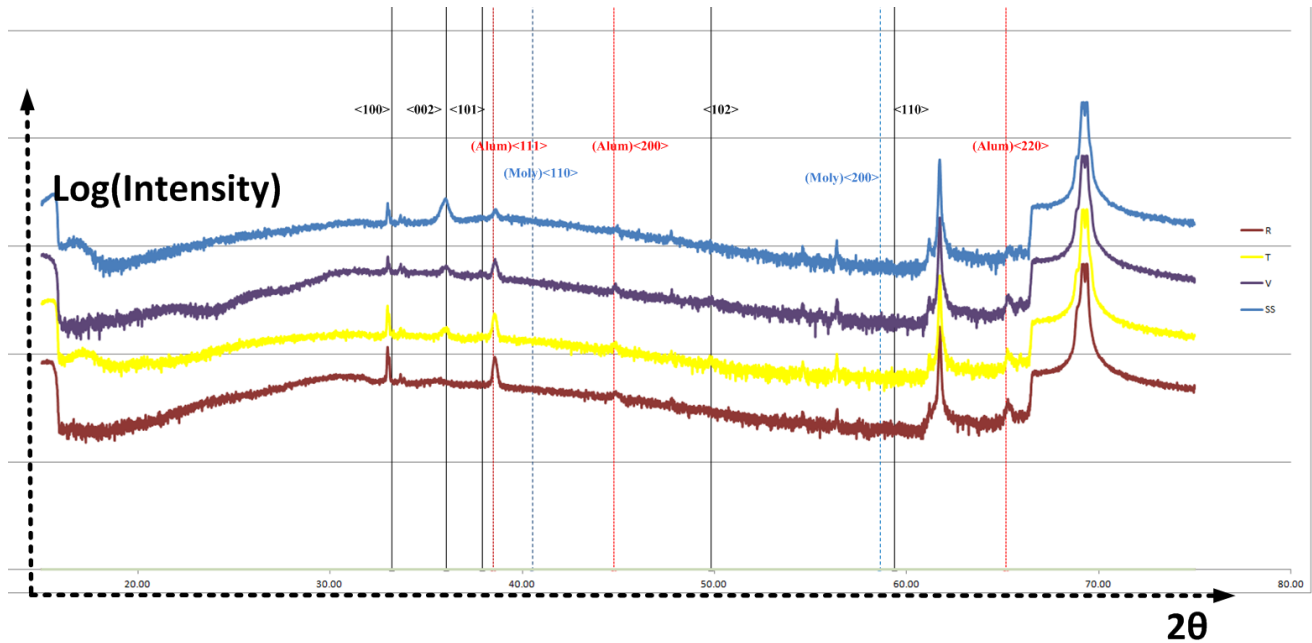


Figure 6.10: **Aluminum nitride process development aluminum bottom layer, the aluminum layer with a following AlN deposition sample SS shows the strongest $\langle 002 \rangle$ AlN, R(1000W +1cm), T(500W +1cm), V(500W ), SS(1000W)**

## Molybdenum Seed Layer 2000 $\mathring{A}$

The molybdenum experiment in Figure 6.11, shows a $\langle 110 \rangle$ peak. Two Powers (500W and 1000W) were done, a height experiment was also performed with a 1cm metal plate added below the substrate to decrease the height to the target during deposition. Sample LL with a power of 1000W showed the strongest Al-N $\langle 002 \rangle$ peak relative to the $\langle 110 \rangle$ and $\langle 102 \rangle$ peaks, followed by Sample X(500W), MM(0100W -1cm) and X(500W -1cm) with the smallest response.
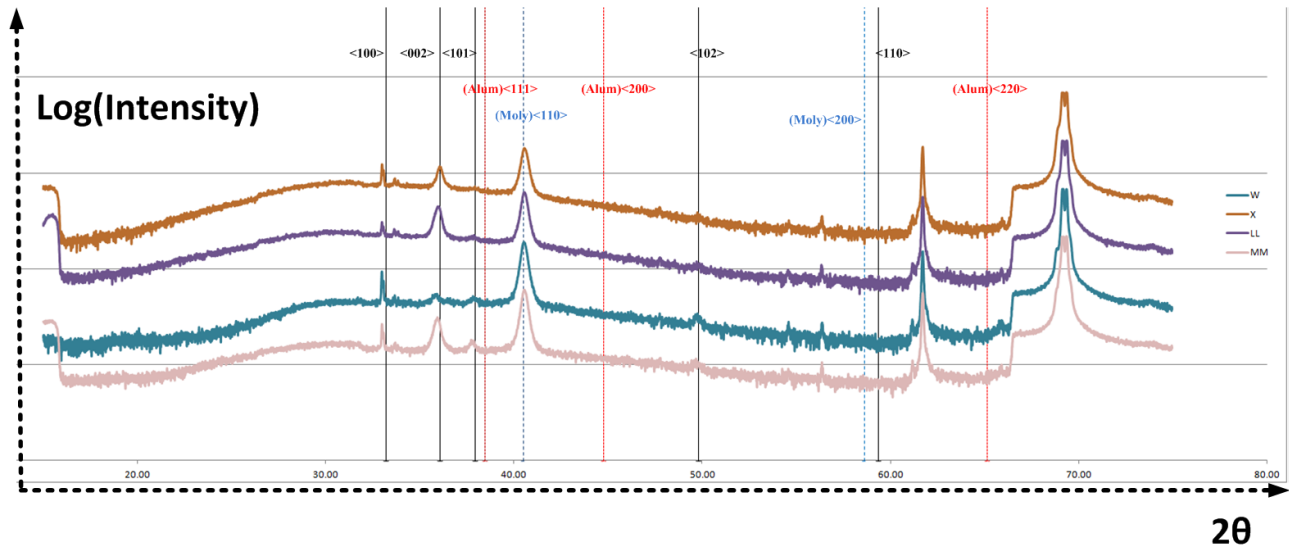


Figure 6.11: **Aluminum nitride process development molybdenum bottom seed layer, with the Al-N deposition sample SS shows the strongest $\langle 002 \rangle$ Al-N, R(1000W +1cm), T(500W +1cm), V(500W ), SS(1000W)**
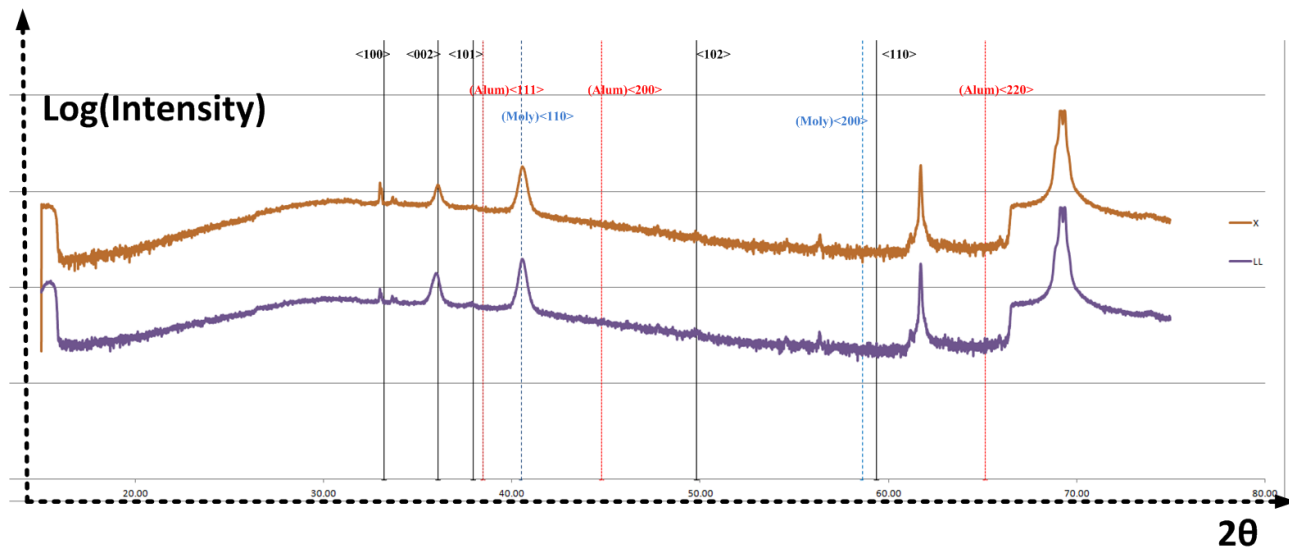


Figure 6.12: **Aluminum nitride process development molybdenum bottom layer, regular distance to target molybdenum layer 500W and 1000W**
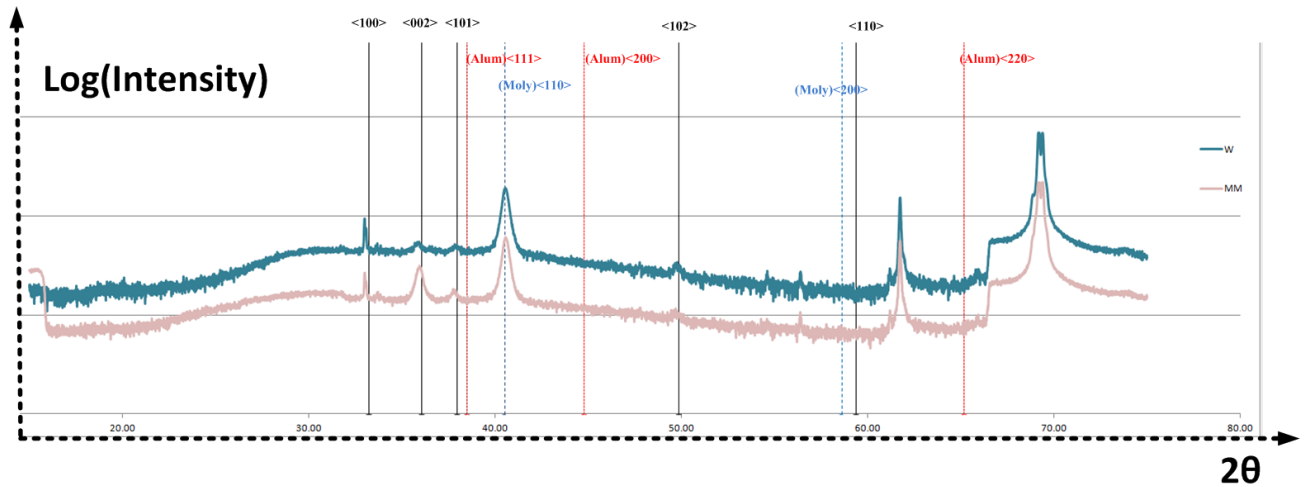
Figure 6.13: **Aluminum nitride process development molybdenum bottom layer target to wafer reduced distance (1cm), with a reduced distance to target molybdenum layer 500W and 1000W by -1cm**

In Figures 6.12 and 6.13 molybdenum as a deposition starting layer is compared. LL(1000W) has the largest ⟨002⟩ peak for the ⟨102⟩ and ⟨110⟩, followed by X(500W) and MM(1000W -1cm)

**1000W**

In Figure 6.14, all of the different runs, done at 1000W are compared. molybdenum, aluminum, bare silicon and a change in distance to target are all compared here. Sample ZZ (1000W Bare Silicon) showed the strongest Al-N $\langle 002 \rangle$ peak relative to the $\langle 110 \rangle$ and $\langle 102 \rangle$ peaks, followed by sample LL( 1000W Molybdenum) Sample MM(1000W -1cm) and SS(1000W Aluminum).
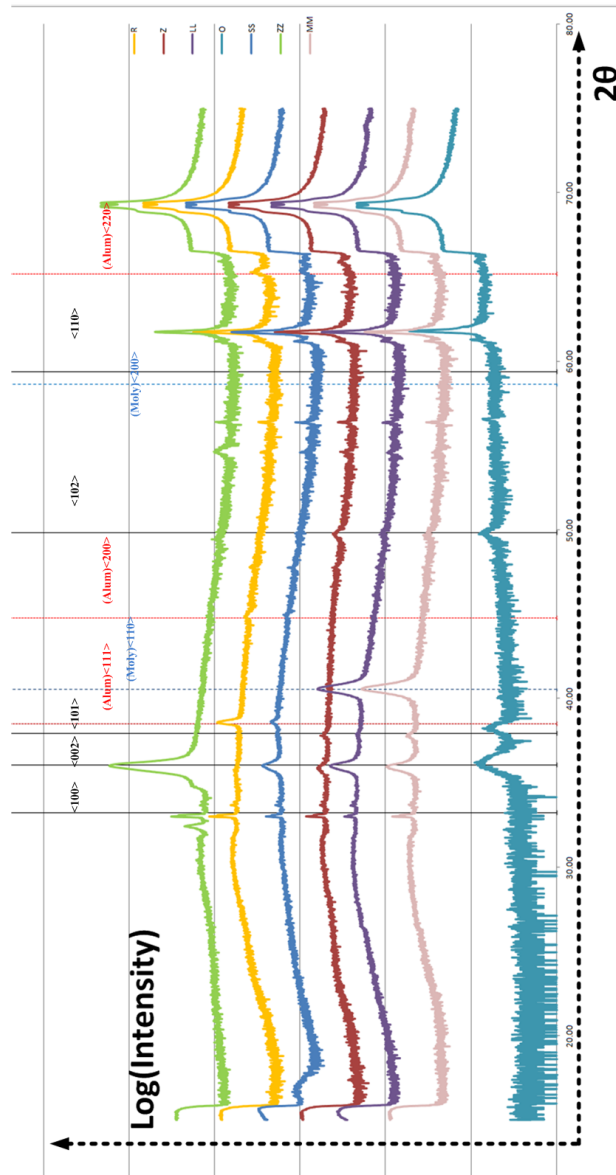


Figure 6.14: **Aluminum nitride process development 1000W, sample ZZ (1000W bare silicon )showed the strongest Al-N $\langle 002 \rangle$ peak relative to the $\langle 110 \rangle$ and $\langle 102 \rangle$ peaks, followed by sample LL(1000W Molybdenum), sample MM(1000W -1cm) and SS(1000W Aluminum).**

**500W**

In Figure 6.15 all of the different runs, done at 500W are compared. molybdenum, aluminum, bare silicon and a change in distance to target are all compared here. Sample YY (bare silicon) showed the strongest Al-N $\langle 002 \rangle$ peak relative to the $\langle 110 \rangle$ peak, however sample X (molybenum) had the best $\langle 002 \rangle$ ratio against the $\langle 102 \rangle$ peak.
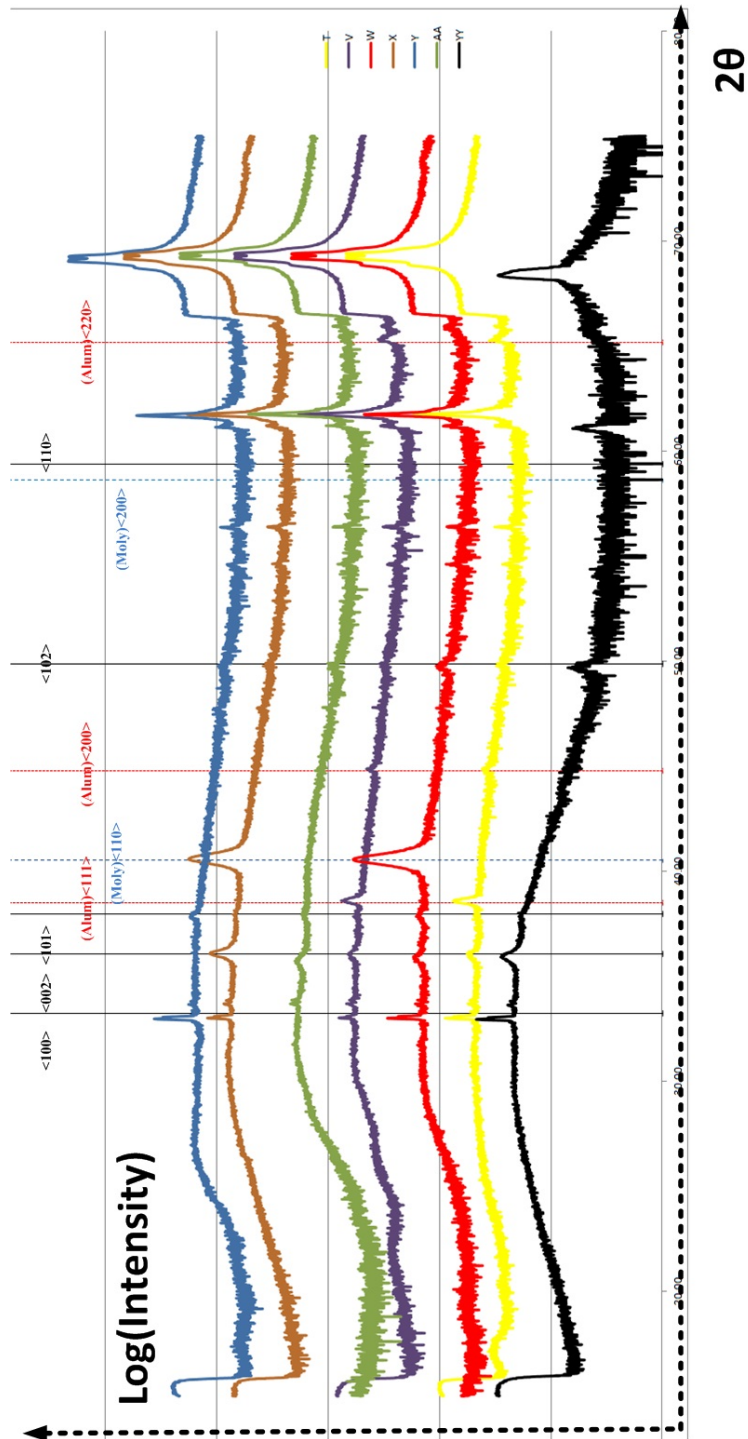
Figure 6.15: **Aluminum nitride process development 500W**

## Decreasing Height to Target

In this comparison, Figure 6.16, all of the runs done with an additional 1cm metal disk placed underneath the substrate are compared. molybdenum, aluminum, bare silicon and both 500W and 1000W are all compared here. Sample MM (1000W Bare Silicon -1cm) showed the strongest Al-N ⟨002⟩ peak relative to the ⟨110⟩ and ⟨102⟩ peak.
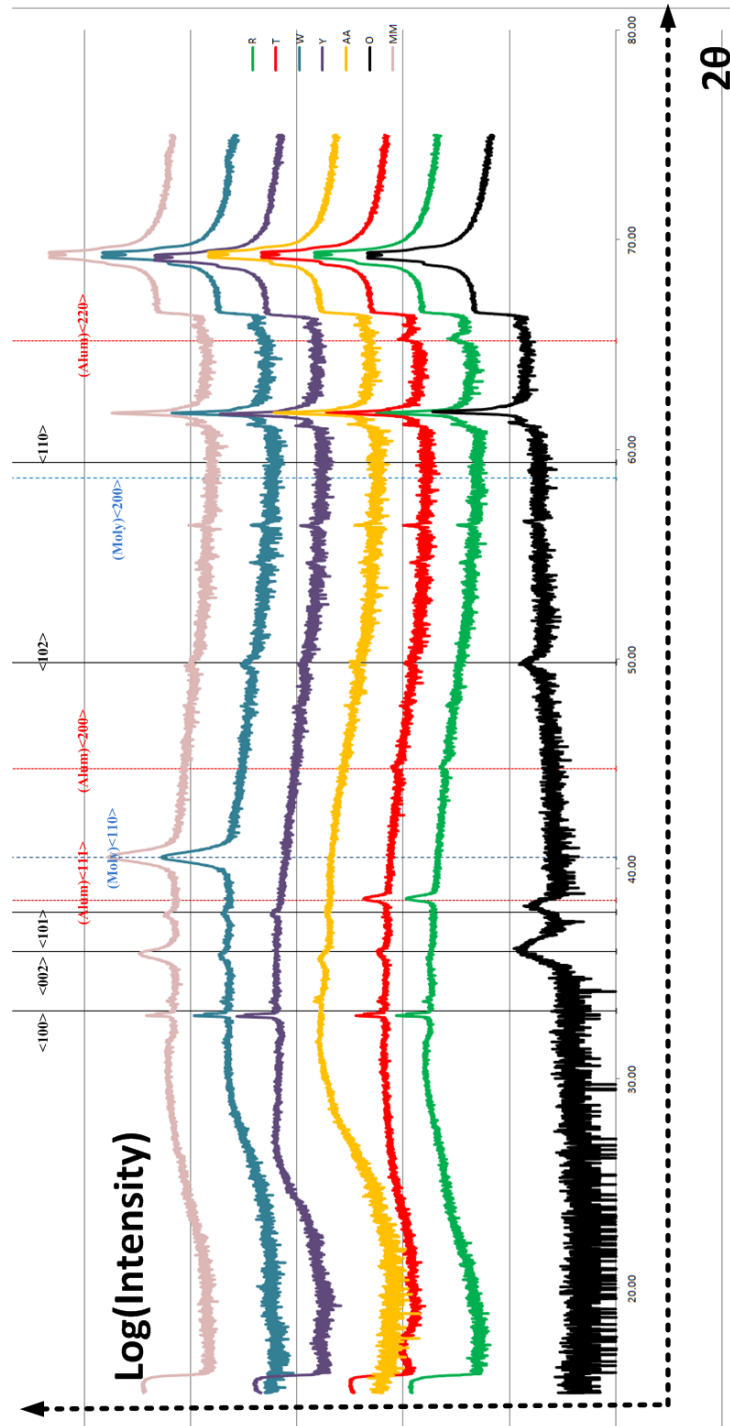


Figure 6.16: **Aluminum nitride process development 1000W**

**Regular Height**

In this comparison all of the runs done at the normal distance to the target are compared. molybdenum, aluminum, bare silicon and both 500W and 1000W are all compared here. Sample ZZ (1000W bare silicon) showed the strongest Al-N $\langle 002 \rangle$ peak relative to the $\langle 110 \rangle$ and $\langle 102 \rangle$ peak, followed by YY(500W) and LL (molybdenum 1000W).
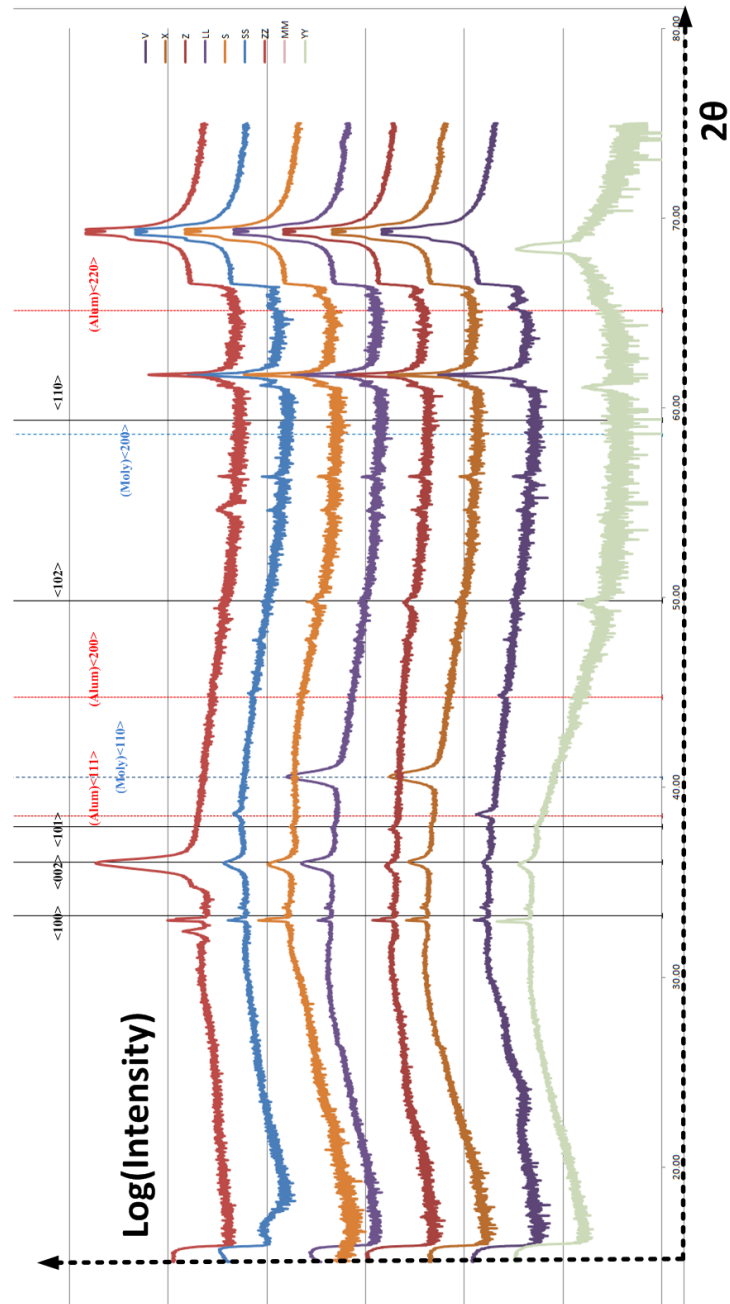


Figure 6.17: **Aluminum nitride process development 1000W**

**Power 500W-750W-1000W**

As shown in Figure 6.18, an experiment was down with three different power settings YY(500W), S(750W) and ZZ(1000). ZZ (1000W) has the strongest Intensity ratios followed by YY (750) and S(500W).
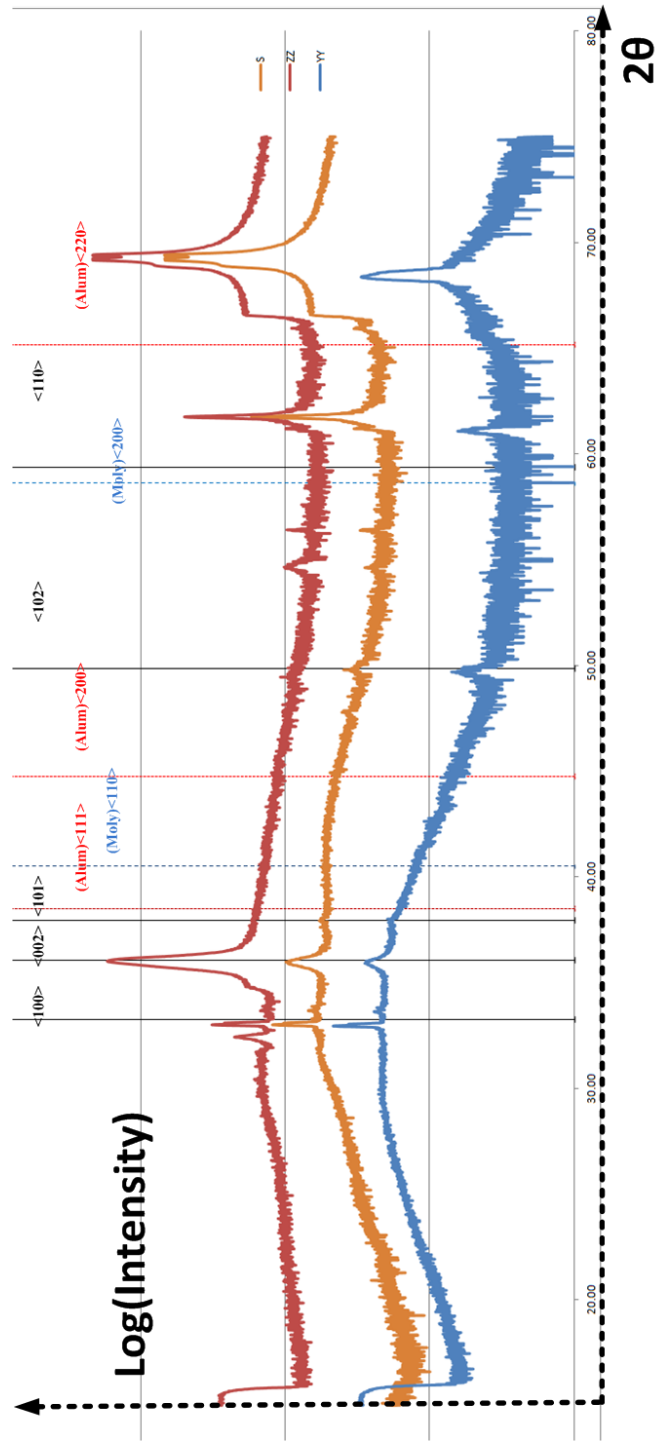


Figure 6.18: **Comparison of different power levels 500W-750W-1000W**

**Aluminum nitride process development fixed and rotated**

Figure 6.19 it is clear that the stationary deposition of aluminum nitride is not uniform. In Figure 6.19 a comparison of the platen rotated at 2 and 5 hours at 20 RPMs is compared with a stationary wafer. It was found that the stationary configuration is the most favorable to the growth of $\langle 002 \rangle$ orientated aluminum nitride. This is likely due to a change in the thermal effects of the deposition chamber, with the rotation of the platen the thermal profile changes which also changes which orientation of aluminum nitride is favored. Since aluminum nitride is transparent with a refractive index of 2.01 the resultant aluminum nitride thickness and uniformity were measured on a Prometrix SM300 SpectraMap and are listed below in Table 6.5.
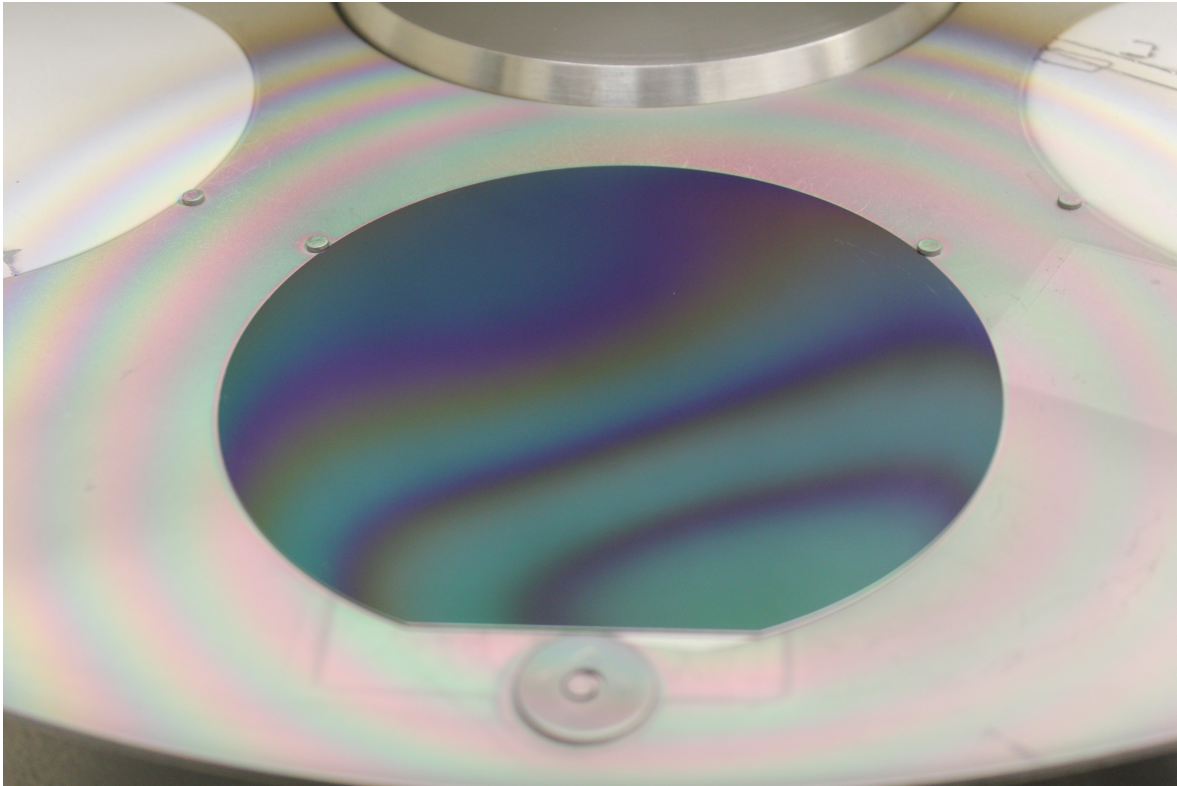


Figure 6.19: **Comparison of the stationary, and rotated platen condition on the $\langle 002 \rangle$ orientation**
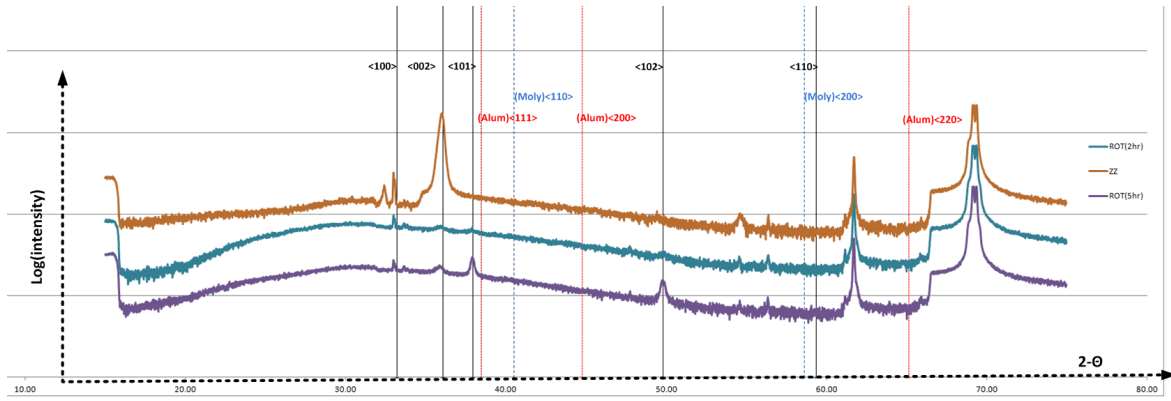
Figure 6.20: **Comparison of the stationary, and rotated platen condition on the $\langle 002 \rangle$ orientation**

Table 6.5: **Aluminum Nitride Deposition Comparison of The Stationary, and Rotated Platen**

| Wafer | Rotation [20 RPM] | Standard Deviation | Mean $\dot{A}$ | Range $\dot{A}$ |
|---|---|---|---|---|
| Stationary | No | 15% | 6406 | 3201 |
| Rotation 2hr | Yes | 2.5% | 6861 | 612.5 |
| Rotation 5hr | Yes | 7.2% | 18784 | 6878 |

## Aluminum Nitride Process Development Stress and Strain

Although, difficult to perceive in the following graphs, the angle of observation for Al-N films is not expected to precisely fall upon its expected 2-theta angle. This is due to compressive stress and strain. When a film is deposited on a silicon substrate this results in tensile stress in the film and compressive stress in the substrate. It was observed in nearly all samples a negative shift in the samples, with a positive shift in the silicon peaks. Silicon $K_{\alpha}$-400 was used as the standard of determination as it has a large single peak, that is easily measured and observed in all the samples. Due to the much larger thickness of the silicon substrate in relation to the Al-N film the shift in the silicon peaks should be lower than the Al-N, this is indeed the observation [65].
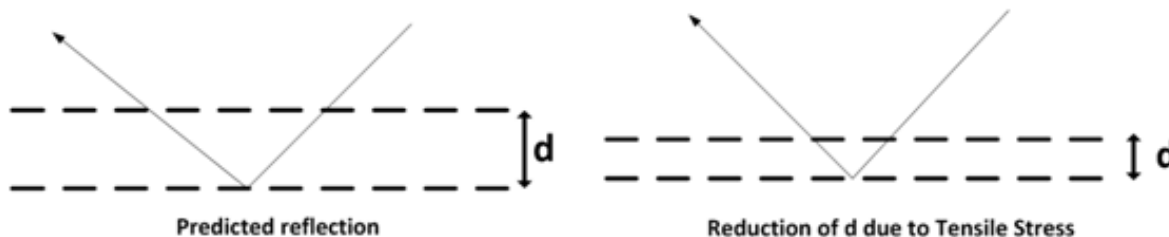


Figure 6.21: **Angle shift due to change in distance between planes d due to film stress**

The wavelength of reflection is a function of the distance between planes. The distance between planes d, can be altered due to tensile or compressive stress. As illustrated in Figure 6.21; Figure 6.22 gives the expected result in terms of intensity and $2\theta$.
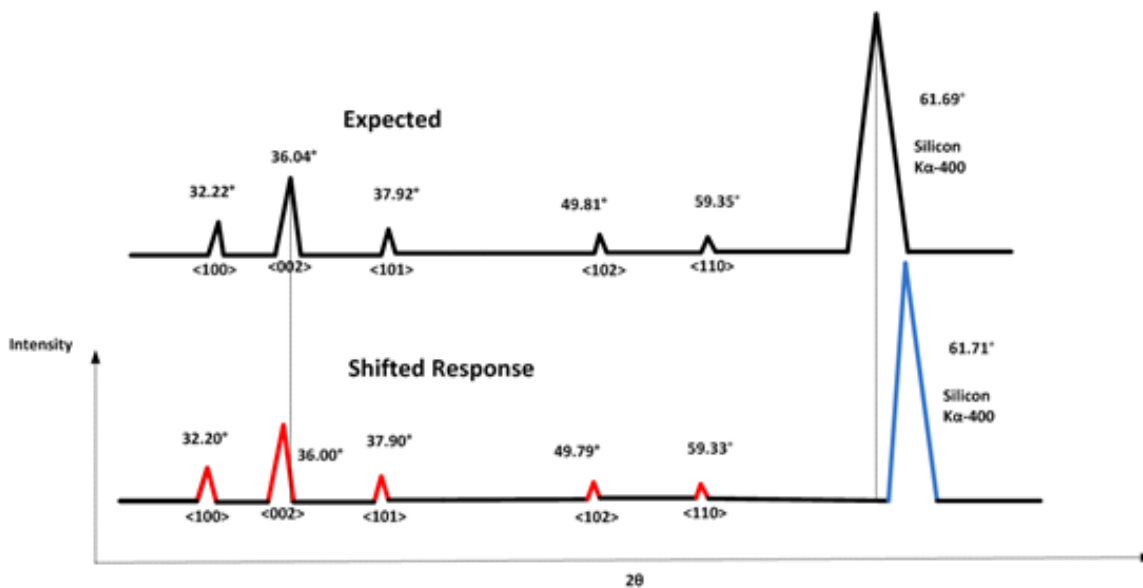


Figure 6.22: **angle shift due to change in distance between planes d due to film stress**

73

## 6.6 Aluminum Nitride Etch Rate Characterization

At RIT aluminum nitride was a new material and had not been characterized for processing. It was necessary to test a series of methods to determine what would be the best way to etch aluminum nitride after its deposition, in order to fabricate devices.

**Aluminum Nitride Etch Rate Hot Phosphoric Acid**

It was determined that phosphoric acid does not attack molybdenum. A single wafer was deposited with aluminum nitride and its thickness was measured with the a nanospec and a simple pattern of lines and spaces exposed and developed upon the film. The wafer was then quartered and each quarter was individually placed in a plate of hot phosphoric acid for 5 minutes. Upon completion of the etch each quarter's photoresist was removed with acetone and the step height measured with a P2 profilometer and nanospec. The etch results are displayed below in Figure 6.23 and the contact via results in Figure 6.24.The etch rate for three different temperatures was determined. at 85 $C°$ the etch rate was determined to be 198 $\frac{nm}{min}$; at 90 $C°$ the etch rate was determined to be 216 $\frac{nm}{min}$ and finally 95 $C°$ was determined to be 260 $\frac{nm}{min}$.
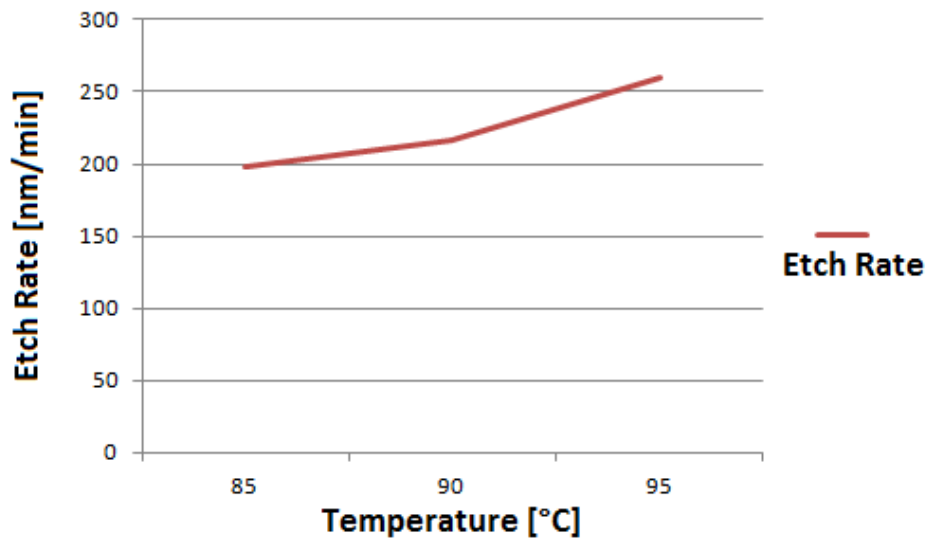


Figure 6.23: **Temperature Dependency of Aluminum Nitride Etch by Hot Phosphoric Acid**

The etch rate for three different temperatures was determined. at 85 $C°$ the etch rate was determined to be 198 $\frac{nm}{min}$; at 90 $C°$ the etch rate was determined to be 216 $\frac{nm}{min}$ and finally 95 $C°$ was determined to be 260 $\frac{nm}{min}$.

Micrographs of Molybdenum and Poly Silicon Bottom Electrode (A) Poly 50x (B) Moly 20x; both showing no change as a result of the phosphoric acid

**LAM 4600**

In addition to a wet etch, a dry etch was also necessary for an isotropic cut, due to the necessity of releasing and defining the devices. Aluminum nitride is a ceramic material and is quite hard, an etch similar to one used for aluminum was chosen as a starting point for the development of an aluminum nitride specific etch. A LAM 4600, shown below in Figure 6.25 was used to perform a dry etch of aluminum nitride using a modified aluminum etch recipe. The LAM 4600 is a reactive ion etcher
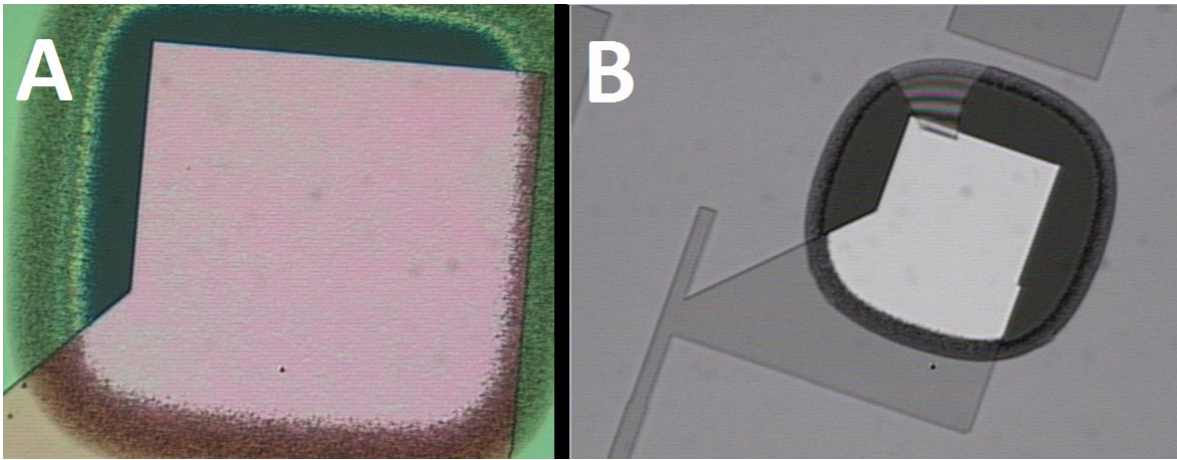
Figure 6.24:  **Micrographs of Molybdenum and Poly Silicon**

for aluminum films, The tool is capable of using Chlorine, boron trichloride, chloroform, oxygen, and nitrogen. Cl$_2$ reduces pure Aluminum, $BCl_3$ etches native aluminum oxide and increase the momentum of physical sputtering, N$_2$ dilutes and is a carrier for the chemistry, the process is shown in Table 6.6.

From Table 6.7 the recipe was modified by increasing the RF power, it was thought to increase the etch of aluminum nitride, however the etch was actually decreased.



Figure 6.25:  **LAM 4600**

The LAM 4600 is a reactive ion etcher for aluminum films, The tool is capable of using Chlorine, Boron Trichloride, Chloroform, Oxygen, and Nitrogen. The etch rate of Aluminum Nitride and the photoresist were measured using a P2 profilometer, the results are displayed below in Figure 6.26 and Figure 6.27.
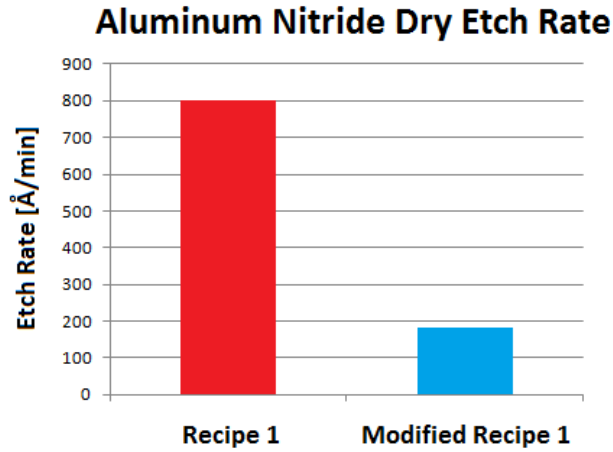
Figure 6.26: **LAM 4600 Aluminum Nitride Dry Etch Rate**
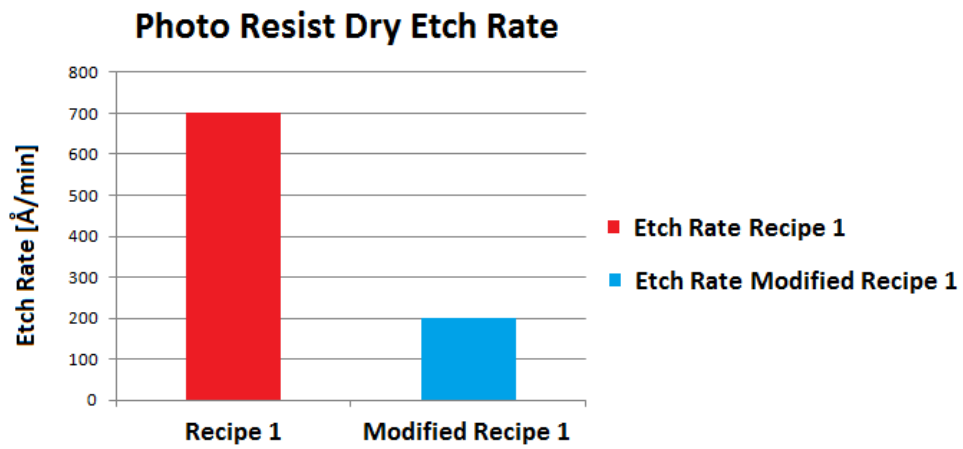


Figure 6.27: **LAM 4600 Photo Resist Dry Etch Rate**

Table 6.6: **SMFL LAM 4600 Recipe 1**

| Step | 1 | 2 | 3 | 4 | 5 | 6 |
|---|---|---|---|---|---|---|
| Pressure mT | 300 | 300 | 300 | 300 | 300 | 300 |
| RF Top | 0 | 0 | 0 | 0 | 0 | 0 |
| RF Bottom | 0 | 350 | 350 | 275 | 275 | 0 |
| Gap cm | 3.000 | 3.000 | 3.000 | 3.000 | 5.3000 | 5.3000 |
| $N_2$ ccm | 25 | 25 | 40 | 50 | 50 | 0 |
| $BCl$ ccm | 100 | 100 | 100 | 50 | 50 | 0 |
| $Cl_2$ ccm | 10 | 10 | 10 | 45 | 0 | 0 |
| Ar ccm | 0 | 0 | 0 | 0 | 0 | 0 |
| $CHCl_3$ ccm | 8 | 8 | 8 | 8 | 8 | 8 |
| Completion | Stabl | Time | Time | OEtch | Time | End |
| Time | 15s | 0s | 100s | 0% | 15s | s |

76

Table 6.7: **SMFL LAM 4600 Recipe 1 modified**

| Step | 1 | 2 | 3 | 4 | 5 | 6 |
|------|-----|------|------|------|--------|--------|
| Pressure mT | 300 | 300 | 300 | 300 | 300 | 300 |
| RF Top | 0 | 0 | 0 | 0 | 0 | 0 |
| RF Bottom | 0 | 350 | 350 | 350 | 275 | 0 |
| Gap cm | 3.000 | 3.000 | 3.000 | 3.000 | 5.3000 | 5.3000 |
| $N_2$ ccm | 25 | 25 | 25 | 50 | 50 | 0 |
| $BCl$ ccm | 100 | 100 | 100 | 100 | 50 | 0 |
| $Cl_2$ ccm | 10 | 10 | 10 | 45 | 0 | 0 |
| Ar ccm | 0 | 0 | 0 | 0 | 0 | 0 |
| $CHCl_3$ ccm | 8 | 8 | 8 | 8 | 8 | 8 |
| Completion | Stabl | Time | Time | OEtch | Time | End |
| Time | 15s | 0s | 100s | 0% | 15s | s |

**Aluminum Nitride Etched by Developer Ghost Image**

The SSI track developer solution etches aluminum nitride. The developer contains tetramethyl ammonium hydroxide (TMAH) which created a faint ghost image upon aluminum nitride. The image was so faint as to be imperceptible in a micrograph, but was visible with the eye using a Leica microscope. The step height of the etch was too small as to be measurable. This observations is confirmed by literature [66].

## 6.7 Aluminum Nitride Piezo Electric Characterization C-V Measurements

Two die from the wafer were selected for C-V testing, for the characterization of aluminum nitride. Below in Figure 6.28 is a 2.5x magnification of the testing structures. A series of circular plate capacitors. with 500, 400 and $200\mu$m diameter were built based on principles from [67].The design also incorporates a key which is displayed below in Figure 6.28. The capacitors were indicated with letters A through I each of the 9 capacitor variations. Die R and Z were used for the c-v measurement and their location can be found on Figure 6.38, the test results report from the metrology company Aixa Ct Gmbh and can be found in Appendix D. A CV test was used, which works on the principle of capacitance and the piezo electric effect, as the dc voltage applied to the capacitor plats is increased the thickness of the dielectric film will change, and an alternating current is applied, as the film thickness changes its impedance to alternating current also changes the rate of this change in impedance can then be used to determine the $d_{33}$ piezoelectric coefficient of the film. The $d_{33}$ measured using CV technique is -0.000108716 $\frac{nm}{V}$, which is -0.108716 $\frac{pm}{V}$ lower than 8pm/V typically reported.The lower piezo electric coefficient measured as compared with typical values, may be due to low film density a result of the high power used in the RF reactive sputtering that was used to heat the platen to a high enough temperature to promote the $\langle 002 \rangle$ oriented growth of AlN, this as well as low film quality due to a lack of temperature control and control of film thickness are possible reasons for low value of the piezoelectric film.
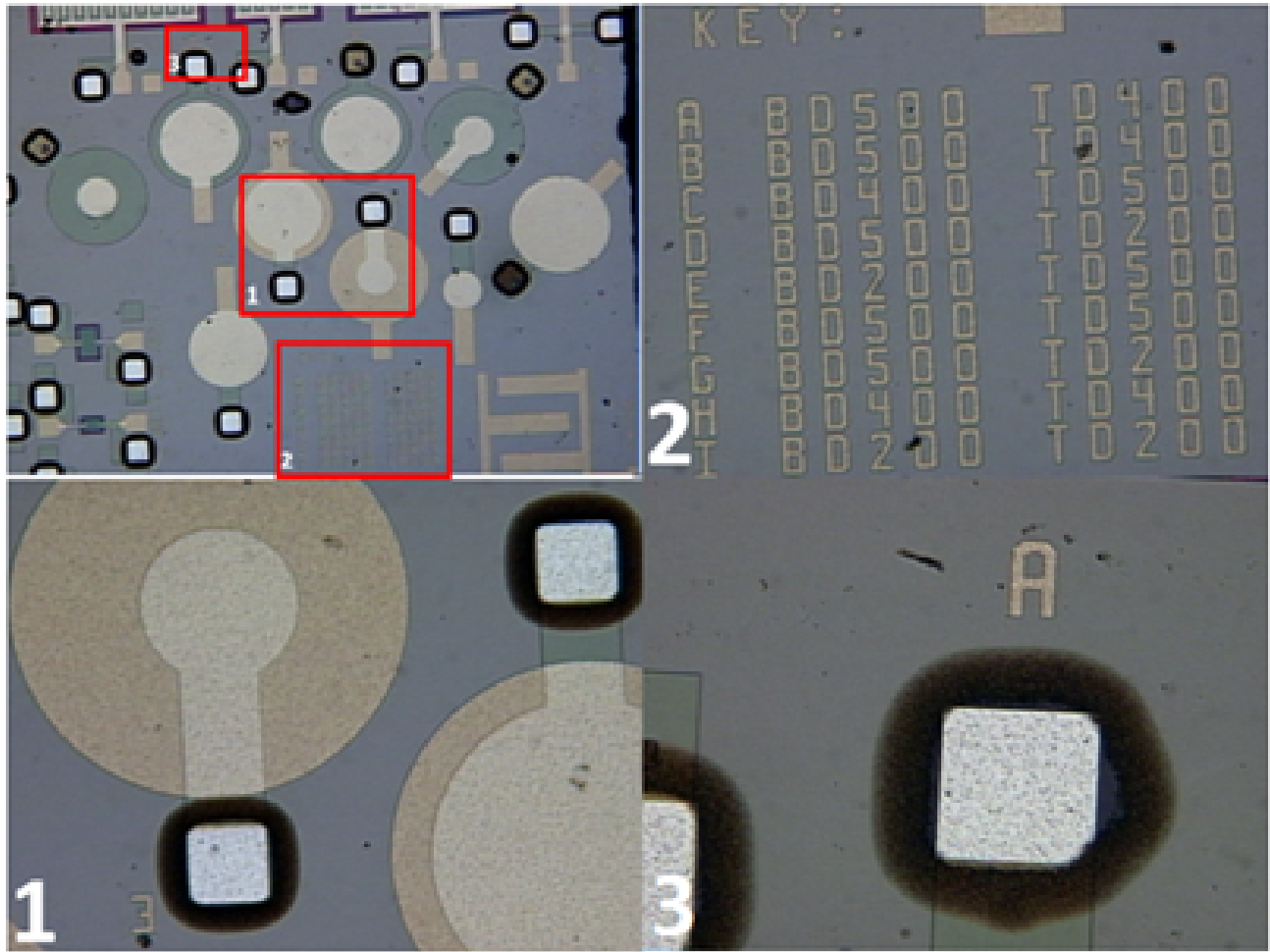
Figure 6.28: **Aluminum Nitride Capacitors**

## 6.8 Aluminum Nitride Process Development Conclusions

It appears in nearly all cases that 1000W is the most important factor contributing to the $\langle 002 \rangle$ orientation, the decreasing of the target distance may inhibit some reaction mechanism in the plasma resulting in a more amorphous deposition. Molybdenum tends to have a stronger $\langle 002 \rangle$ peak relative to aluminum, but the pump down time for the molybdenum was not typical for this clean room and was only on the order of several hours, this may have contributed to a poor film in terms of surface roughness.

Molybdenum is not consumed in a wet etch of KOH.Molybdenum is oxidized during photo resist ashing. A hard mask process should be investigated instead of the previous technique of applying and removing photoresist after each dry etch in the LAM4600 (step 17-20)x6. The contact vias were necessarily over retched in order to ensure complete removal of Al-N over the bottom electrode. If the current Al-N process is used in the future it may be preferable to decrease the size of the contact via, so that the over etch does not encroach on other devices.

In regards to the C-V measurements, the measured $d_{33}$ is -0.000108716 $\frac{nm}{V}$, which is -0.108716 $\frac{pm}{V}$ lower than 8pm/V typically reported.The lower piezo electric coefficient measured as compared with typical values, may be due to low film density a result of the high power used in the RF reactive sputtering that was used to heat the platen to a high enough temperature to promote the $\langle 002 \rangle$ oriented growth of AlN.

## 6.9   Aluminum Nitride Resonators RF Measurements

The design of the resonators followed a systematic methodology with resonators changing in terms of electrode pitch, anchor width, electrode overlap length and the number of electrodes; a basic layout of a section of the design is shown in Figures 6.29 and 6.30 . The iterations of the design resulted in over 200 unique devices per mask not including the Capacitors used for CV measurements to determine the $d_{33}$ aluminum nitride piezoelectric coefficients and the SAW resonators.
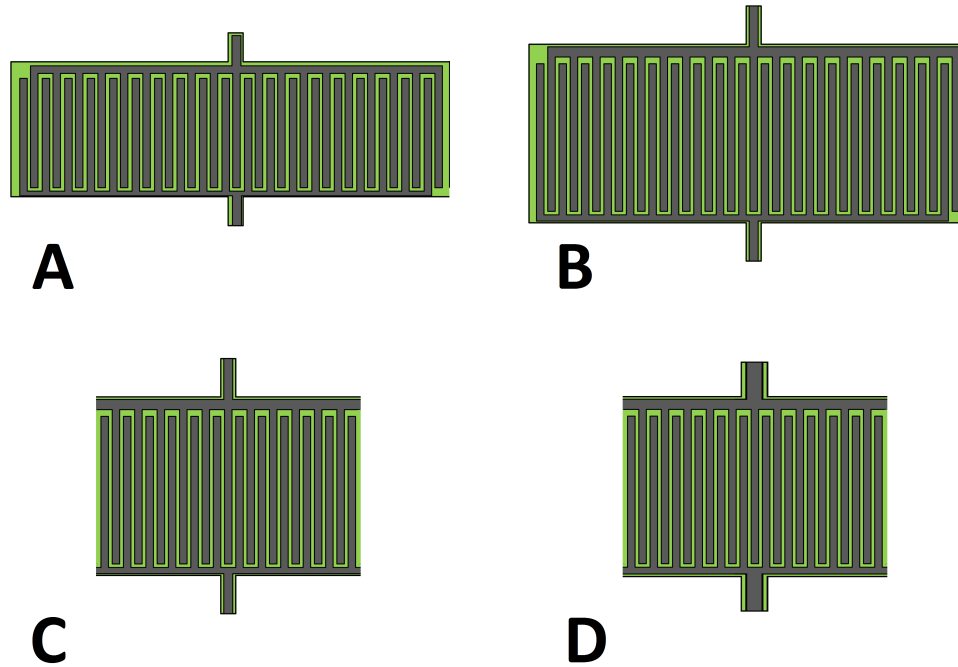


Figure 6.29:   **Design Methodology**

Figure 6.29 represents 4 major examples of a different resonator configurations; in A the electrode overlap is 25 $\mu$m while in B the electrode overlap is 50 $\mu$m in C the Anchor width is 3 $\mu$m in D the anchor width is 5 $\mu$m while the top electrode width is 3$\mu$m and so on.

### 6.9.1    Resonator Frequency Design Tests

The resonators were tested with an Agilent Network Analyzer. The devices were tested in the 1-port configuration, with the bottom electrode being grounded. The devices were initially swepted form 100 MHz to 20 Ghz with the frequency sweep gradually being narrowed down to focus on any resonant peaks. After the area of interest was found, in this case in the 4.7 Ghz range, a standard 3 to 6 Ghz range and 1dB/division was used to compare different device's response to the same stimuli. The results of the tests are shown below for a series of different tests, including electrode overlap, increasing the number of electrodes, changing the pitch from 5 to 6 $\mu$m, anchor width as well as the thickness of the piezo electric film.

**Increasing Number of Electrodes**
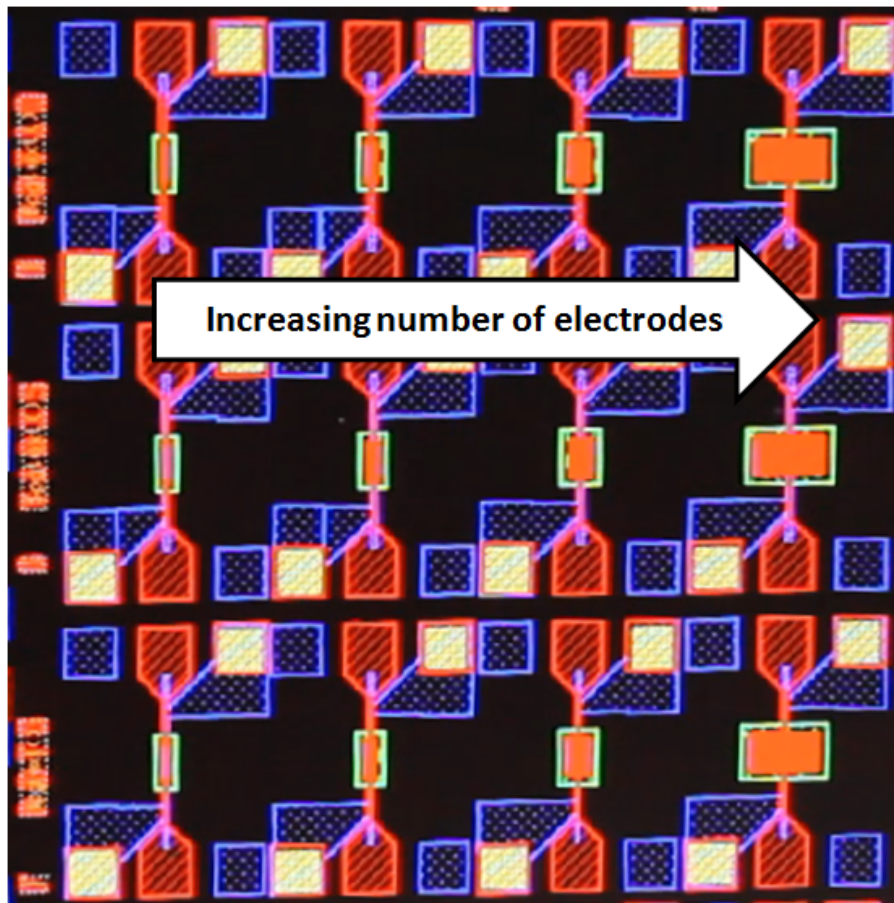


Figure 6.30:  **Increasing Number of Electrodes**

For the first configuration, shown in Figures 6.30 and 6.31, the resonant frequency remains constant, but the amplitude, increases for an increasing number of electrodes. In Figure 6.32 a linear relationship has been established between the number of electrodes and the relative resonator response, with more electrodes having a relatively larger response to stimuli.
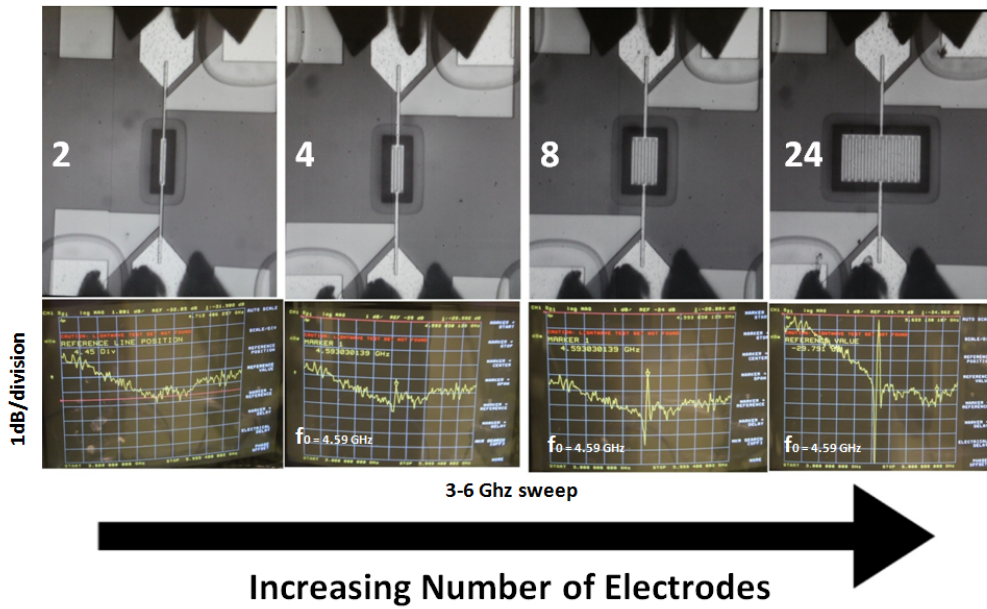
Figure 6.31: **Increasing Number of Electrodes**
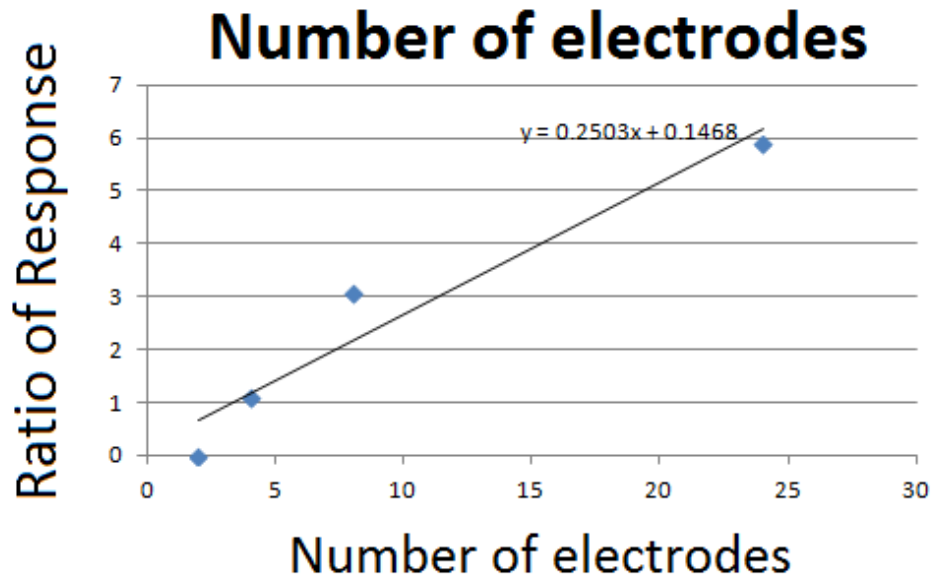


Figure 6.32: **Number of electrodes plot**

## Increasing Anchor Width

Increasing the anchor width from $5\mu$m to $10\mu$m to $20\mu$m lowers the amplitude of the response therefore lowering the Q of the resonator. It may be that the increasingly wide anchor, increases the mechanical resistances within the device and allows for greater ease of vibrations and a stronger response to stimuli. In Figure 6.34 a linear relationship has been established between the width of the anchors and the relative resonator response, with a thinner anchor the relative response increases.
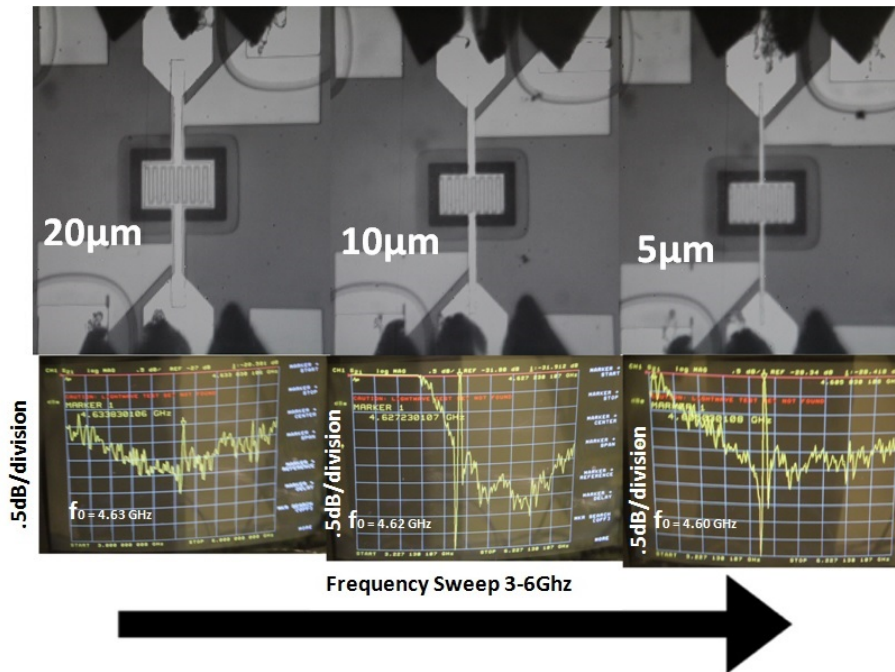


Figure 6.33: **Anchor width**
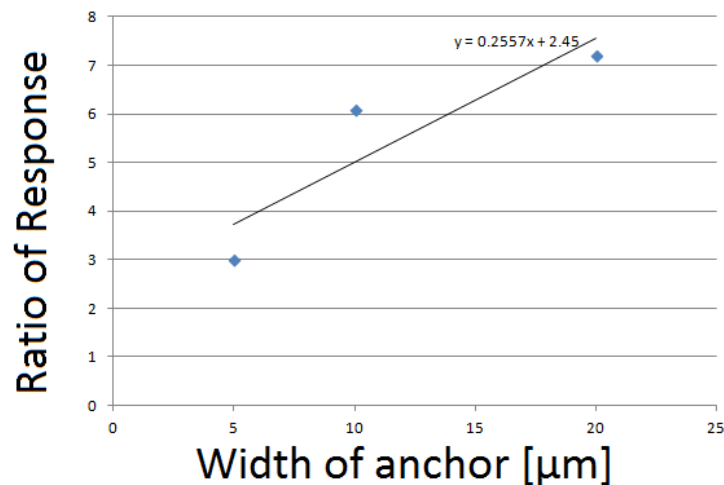


Figure 6.34: **Anchor width plot**

**Increasing Resonator Pitch**

Increasing pitch from $5\mu$m to $6\mu$m seems to have a small effect on the resonant frequency of the devices, shifting them from 4.57 to 4.59 GHz, in this particular die. Figure 6.35 shows the change in response for the two pitches designed, with a .54 percent difference in resonant frequency change for a $1$ $\mu$m change in pitch. This small change in pitch may be due to the grounding of the bottom electrode where the change in pitch necessitates a two port device whereas the devices were tested in the one port configuration.
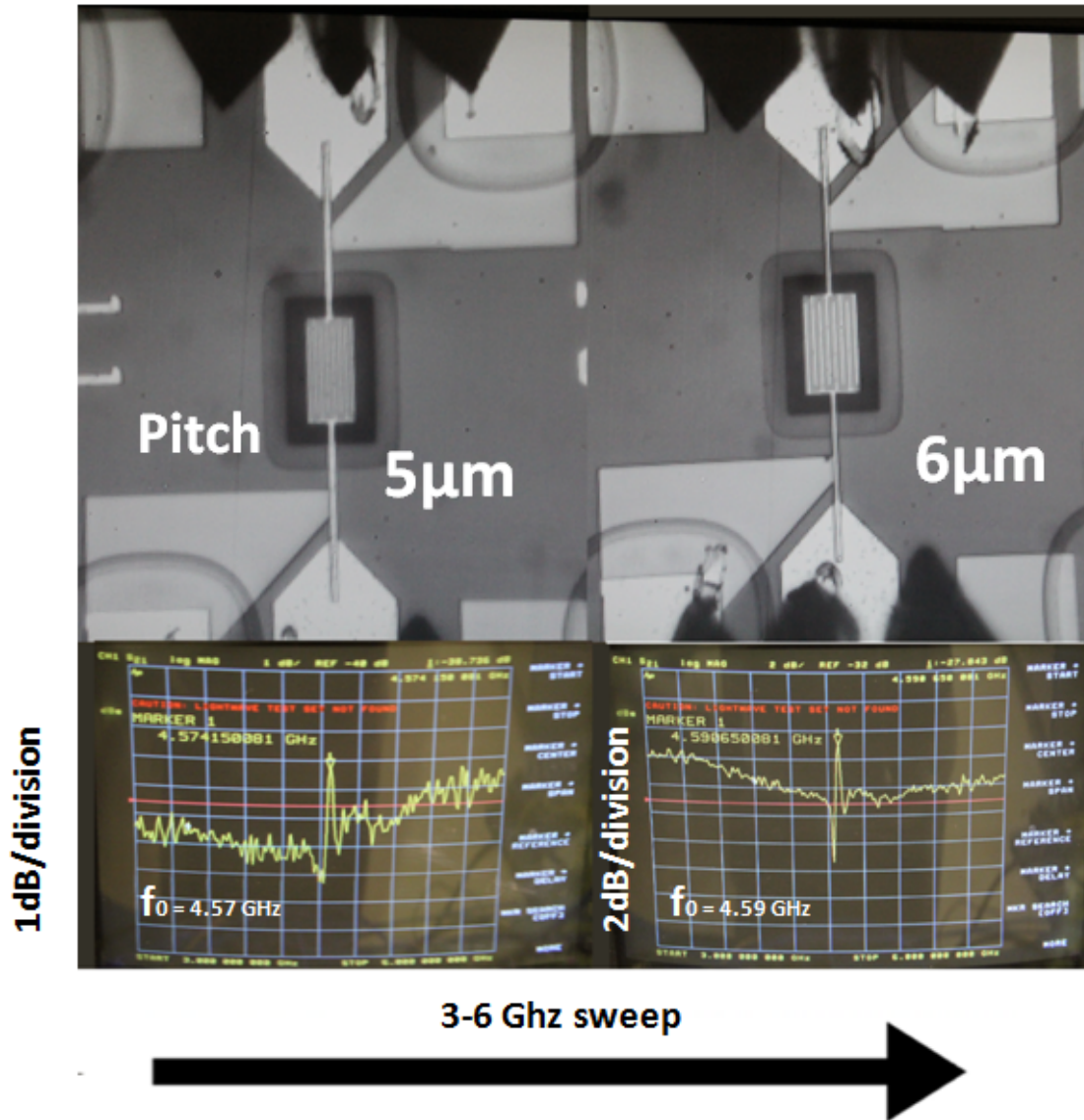


Figure 6.35: **Increasing pitch from $5\mu$m to $6\mu$m**

## Increasing Electrode Overlap

Increasing the electrode overlap, as shown in Figure 6.36, does not appear to have an effect on the resonant frequency, but does increase the amplitude of the response at that die's given frequency. The design shifts from 25 to 50 to 75 $\mu$m. In Figure 6.37 a linear relationship was established between the response of the resonator relative to the electrode overlap
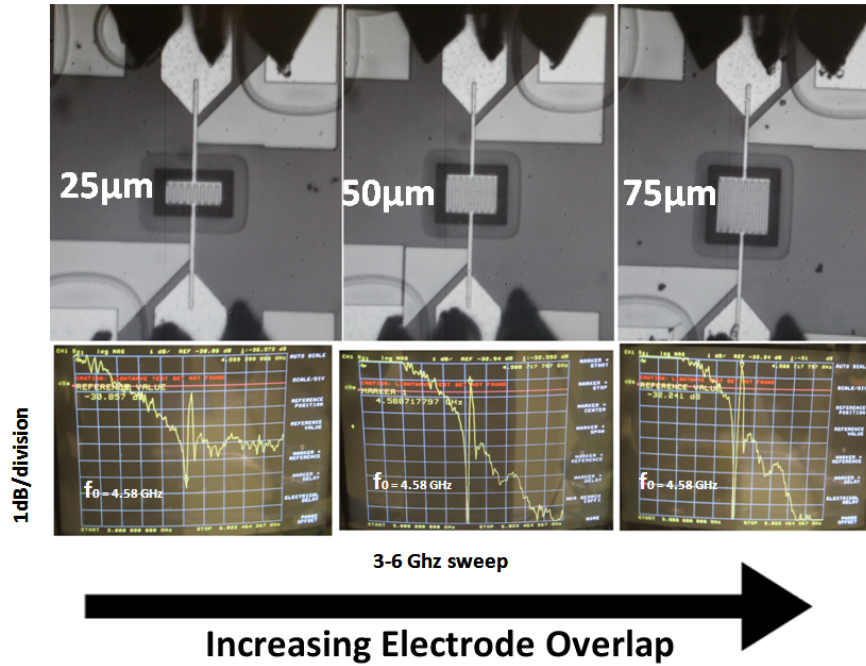


Figure 6.36:   **Increasing electrode overlap**
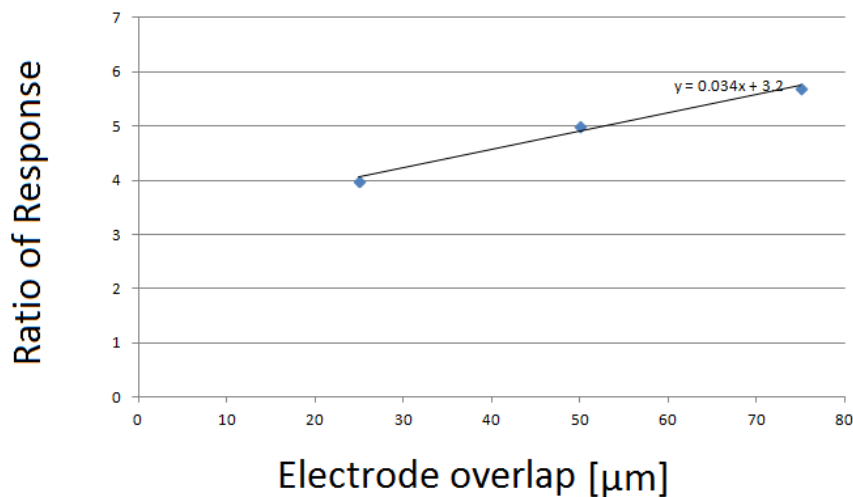


Figure 6.37:   **Increasing electrode overlap plot**

### 6.9.2    Thickness Dependence of Resonator Frequency

In the process of testing the resonators several die were used from differing sources on the wafer. The thickness of each die was measured with the P2 profilometer and the resonant frequency measured. It was observed that there was a change in frequency with a change in thickness for the devices. This is not in agreement with previously expected results as the thickness should not have an appreciable effect on the resonant frequency of the device for LAMB Mode devices, instead the pitch of the electrodes should have a greater overall effect on the resonator this data has been tabulated in 6.8 and a picture of the different die locations is given in Figure 6.38 and a photograph of the nonuniformity of the Aluminum Nitride deposition in Figure 6.19.
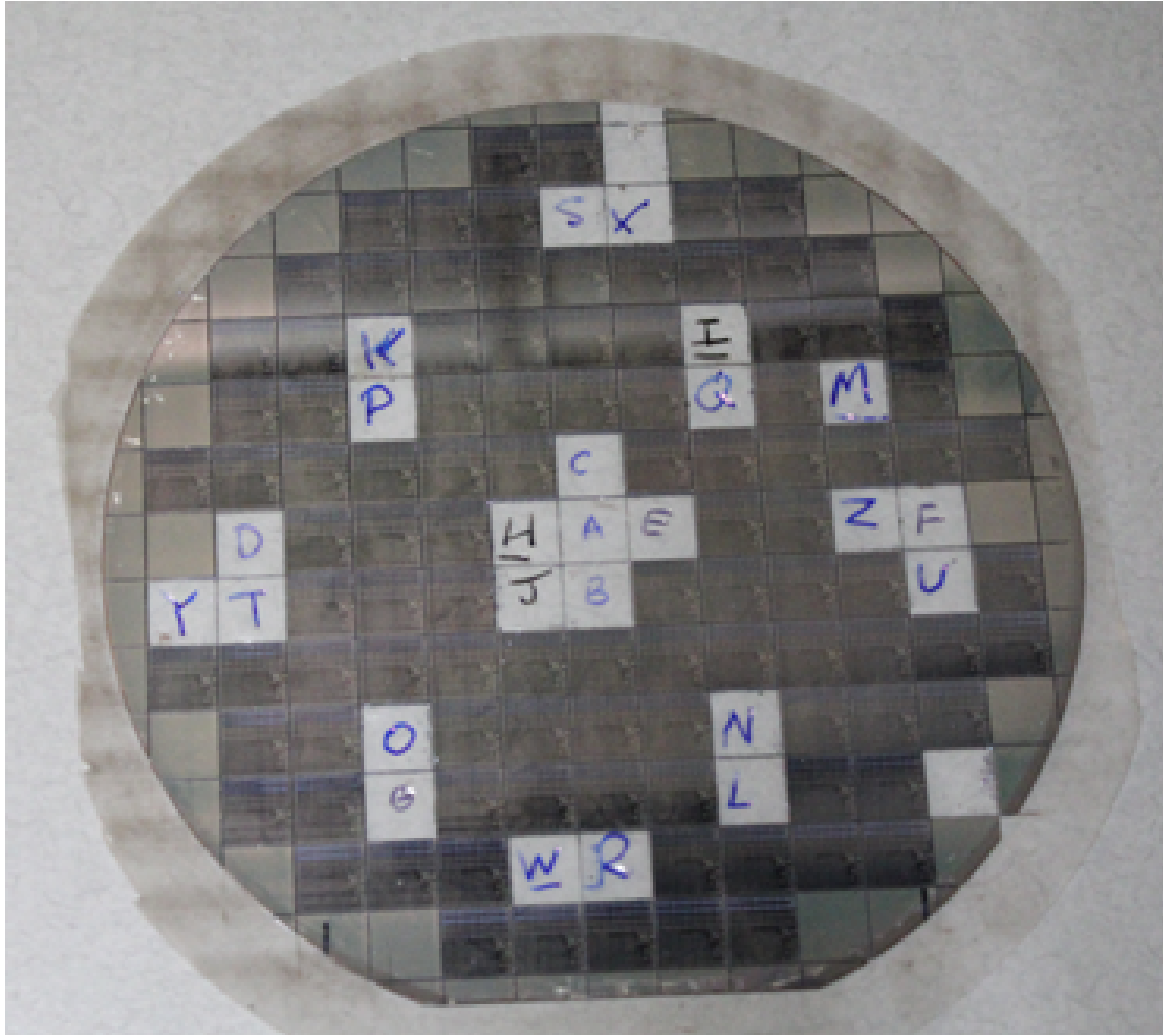


Figure 6.38:   **Die location on wafer**

From Figure 6.20 it can be seen that due to the stationary deposition, the AlN it highly non uniform, this can result in widely different Aluminum Nitride thicknesses for the designed resonators. From Table 6.8 and Figure 6.39 there is a linear relationship between the thickness and resonant frequency of the resonators.

Table 6.8:  **Comparison of Resonator Thickness and Observed Resonant Frequency**

| Die | Thickness nm | Resonant Frequency GHz |
|-----|--------------|------------------------|
| D | 737 | 3.13 |
| J | 870 | 4.68 |
| Z | 925 | 4.38 |
| A | 950 | 4.57 |
| I | 1030 | 4.76 |
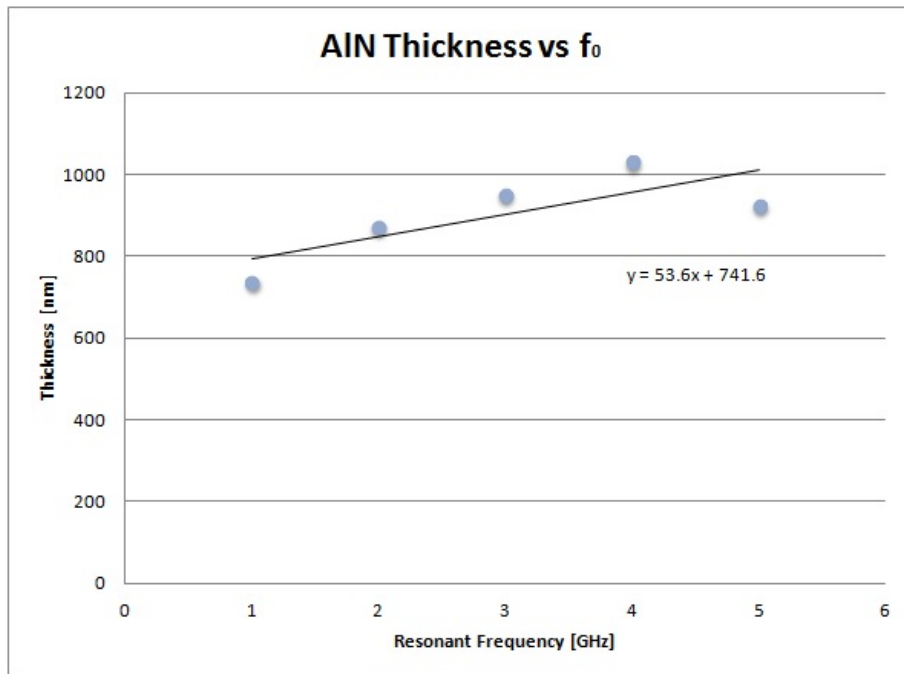


Figure 6.39:  **Thickness vs Resonant Frequency**

### 6.9.3   Resonator Q factor

Figure 6.40 and equation 6.1 are an example calculation showing that the resonators in chip A, with an anchor width of $5\mu m$, pitch of $5\mu m$, 24 electrodes and an electrode overlap of $75\mu m$ had a measured Q value of 98.8. This Q value can be considered lower than typical reported values, but even lower values have been reported [68] , this is likely due to the film quality which was already discussed in section 10.7 c-v measurements.

The resonators described were also independently confirmed at Carnegie Mellon with Dr. Piazza's group, using similar tools. The same devices were measured and confirmed to be resonating, thus giving a secondary confirmation by a peer.
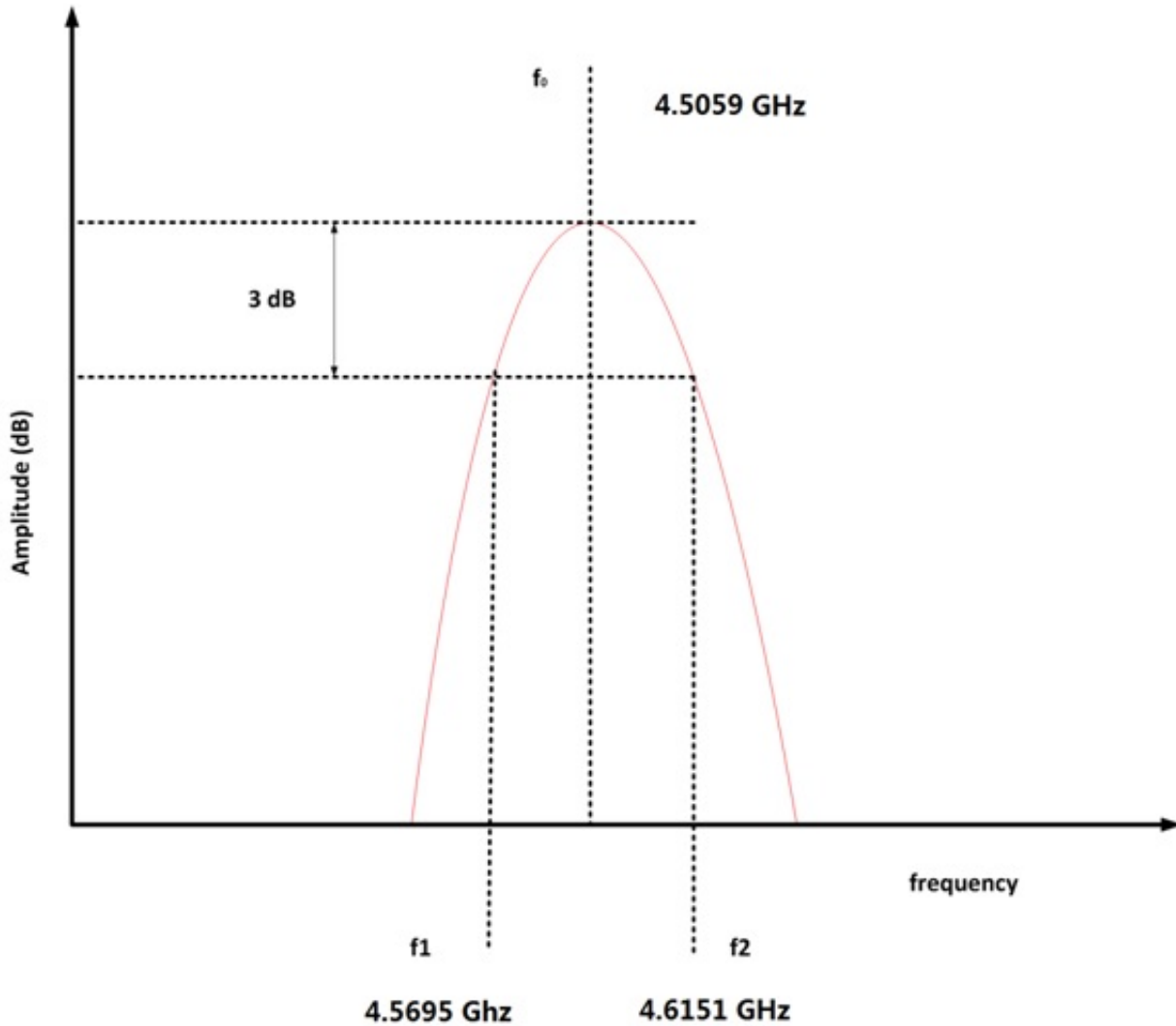


Figure 6.40:   **Q of resonator**

$$Q = \frac{f_0}{f_2 - f_1} = \frac{4.5059 GHz}{4.6151 GHz - 4.5059 GHz} = 98.8 \tag{6.1}$$

## 6.10 Aluminum Nitride Resonators RF Measurements Conclusions

This thesis was the first time that RF MEMS resonators have been successfully fabricated at RIT. This thesis demonstrates a successfully researched and developed aluminum nitride piezoelectric thin film process, design, processing, simulation and testing. Test results confirmed that the devices are working and Aluminum Nitride film is indeed piezoelectric.

Increasing the electrode overlap from 25 to 50 to 75 $\mu$m,it does not appear to have an effect on the resonant frequency, but does increase the amplitude of the response at that die's given frequency. Increasing the anchor width from $5\mu$m to $10\mu$m to $20\mu$m lowers the relative amplitude of the response therefore lowering the Q of the resonator. It may be that the increasingly wide anchor, increases the mechanical resistances within the device. Increasing the number of electrodes increases the relative amplitude of the response. Increasing pitch from $5\mu$m to $6\mu$m seems to have a small effect on the resonant frequency of the devices, shifting them from 4.57 to 4.59 GHz.

## 6.11    Aluminum Nitride Resonators RF Suggestions For Future Work

The AlN needs to be fully characterized such as: (piezo response, $\langle 002 \rangle$ inclined planes, effect of wet etch on surface morphology, etc. improve layout and design to accommodate test equipment with better grounding and contact placement, develop a hard mask process for the AlN Dry Etch. A huge possibility of new sensors and devices are possible, may be interesting to coordinate with CMOS process for a fully functioning chip, investigation of ladder networks and even ion beam trimming techniques could be possible.

# Appendix A

# Elastic Tensor Matrix

Typically, Young's Modulus and the Stiffness coefficient are not interchangeable. In Figure 3.4 (sigma and epsilon) there are nine $\sigma_{ij}$ and nine $\epsilon_{kl}$ so that the general form of the elasticity coefficient has eighty one $C_{ijkl}$ coefficients and eighty one $S_{ijkl}$ which are both fourth rank tensors.

$$
\begin{pmatrix} \sigma_{11} \\ \sigma_{22} \\ \sigma_{33} \\ \sigma_{23} \\ \sigma_{31} \\ \sigma_{12} \\ \sigma_{32} \\ \sigma_{13} \\ \sigma_{21} \end{pmatrix} = \begin{pmatrix} C_{1111} & C_{1122} & C_{1133} & C_{1123} & C_{1131} & C_{1112} & C_{1132} & C_{1113} & C_{1121} \\ C_{2211} & C_{2222} & C_{2233} & C_{2223} & C_{2231} & C_{2212} & C_{2232} & C_{2213} & C_{2221} \\ C_{3311} & C_{3322} & C_{3333} & C_{3323} & C_{3331} & C_{3312} & C_{3332} & C_{3313} & C_{3321} \\ C_{2311} & C_{2322} & C_{2333} & C_{2323} & C_{2331} & C_{2312} & C_{2332} & C_{2313} & C_{2321} \\ C_{3111} & C_{3122} & C_{3133} & C_{3123} & C_{3131} & C_{3112} & C_{3132} & C_{3113} & C_{3121} \\ C_{1211} & C_{1222} & C_{1233} & C_{1223} & C_{1231} & C_{1212} & C_{1232} & C_{1213} & C_{1221} \\ C_{3211} & C_{3222} & C_{3233} & C_{3223} & C_{3231} & C_{3212} & C_{3232} & C_{3213} & C_{3221} \\ C_{1311} & C_{1322} & C_{1333} & C_{1323} & C_{1331} & C_{1312} & C_{1332} & C_{1313} & C_{1321} \\ C_{2111} & C_{2122} & C_{2133} & C_{2123} & C_{2131} & C_{2112} & C_{2132} & C_{2113} & C_{2121} \end{pmatrix} \begin{pmatrix} \epsilon_{11} \\ \epsilon_{22} \\ \epsilon_{33} \\ \epsilon_{23} \\ \epsilon_{31} \\ \epsilon_{12} \\ \epsilon_{32} \\ \epsilon_{13} \\ \epsilon_{21} \end{pmatrix} \tag{A.1}
$$

$$
\begin{pmatrix} \epsilon_{11} \\ \epsilon_{22} \\ \epsilon_{33} \\ \epsilon_{23} \\ \epsilon_{31} \\ \epsilon_{12} \\ \epsilon_{32} \\ \epsilon_{13} \\ \epsilon_{21} \end{pmatrix} = \begin{pmatrix} S_{1111} & S_{1122} & S_{1133} & S_{1123} & S_{1131} & S_{1112} & S_{1132} & S_{1113} & S_{1121} \\ S_{2211} & S_{2222} & S_{2233} & S_{2223} & S_{2231} & S_{2212} & S_{2232} & S_{2213} & S_{2221} \\ S_{3311} & S_{3322} & S_{3333} & S_{3323} & S_{3331} & S_{3312} & S_{3332} & S_{3313} & S_{3321} \\ S_{2311} & S_{2322} & S_{2333} & S_{2323} & S_{2331} & S_{2312} & S_{2332} & S_{2313} & S_{2321} \\ S_{3111} & S_{3122} & S_{3133} & S_{3123} & S_{3131} & S_{3112} & S_{3132} & S_{3113} & S_{3121} \\ S_{1211} & S_{1222} & S_{1233} & S_{1223} & S_{1231} & S_{1212} & S_{1232} & S_{1213} & S_{1221} \\ S_{3211} & S_{3222} & S_{3233} & S_{3223} & S_{3231} & S_{3212} & S_{3232} & S_{3213} & S_{3221} \\ S_{1311} & S_{1322} & S_{1333} & S_{1323} & S_{1331} & S_{1312} & S_{1332} & S_{1313} & S_{1321} \\ S_{2111} & S_{2122} & S_{2133} & S_{2123} & S_{2131} & S_{2112} & S_{2132} & S_{2113} & C_{2121} \end{pmatrix} \begin{pmatrix} \sigma_{11} \\ \sigma_{22} \\ \sigma_{33} \\ \sigma_{23} \\ \sigma_{31} \\ \sigma_{12} \\ \sigma_{32} \\ \sigma_{13} \\ \sigma_{21} \end{pmatrix} \tag{A.2}
$$

Upon examination it can be seen that there are redundant indices in the full matrix form. In the case of the strain tensor $\sigma_{12} = \sigma_{21}; \sigma_{13} = \sigma_{31}; \sigma_{23} = \sigma_{32}$; in the stress tensor $\epsilon_{12} = \epsilon_{21}; \epsilon_{13} = \epsilon_{31}; \epsilon_{23} = \epsilon_{32}$; This symmetry was seen by Voigt and since his contracted matrix notation has been used since. Where a pair of indices are expressed as a single number.

$$
\begin{array}{ccccccc}
ij\ or\ kl & 11 & 22 & 33 & 23,32 & 31,13 & 12,21 \\
& \downarrow & \downarrow & \downarrow & \downarrow & \downarrow & \downarrow \\
m\ or\ n & 1 & 2 & 3 & 4 & 5 & 6
\end{array} \tag{A.3}
$$

This alone can reduce the above matrix from a 9x9 to a 6x6 In addition the stress and strain may be contracted as well, and the tensile strain may be written as in angular form with $\gamma$. Where

$$\gamma_{23} = \epsilon_{23} + \epsilon_{32} \tag{A.4}$$

$$\gamma_{31} = \epsilon_{31} + \epsilon_{13} \tag{A.5}$$

$$\gamma_{12} = \epsilon_{12} + \epsilon_{11} \tag{A.6}$$

Contracted tensor notation

$$
\begin{pmatrix}
\epsilon_1 \\
\epsilon_2 \\
\epsilon_3 \\
\frac{\gamma_4}{2} \\
\frac{\gamma_5}{2} \\
\frac{\gamma_6}{2} \\
\frac{\gamma_4}{2} \\
\frac{\gamma_5}{2} \\
\frac{\gamma_6}{2}
\end{pmatrix}
=
\begin{pmatrix}
S_{11} & S_{12} & S_{13} & S_{14} & S_{15} & S_{16} & S_{14} & S_{15} & S_{16} \\
S_{12} & S_{22} & S_{23} & S_{24} & S_{25} & S_{26} & S_{24} & S_{25} & S_{26} \\
S_{13} & S_{23} & S_{33} & S_{34} & S_{35} & S_{36} & S_{34} & S_{35} & S_{36} \\
S_{14} & S_{24} & S_{34} & S_{44} & S_{45} & S_{46} & S_{44} & S_{45} & S_{46} \\
S_{15} & S_{25} & S_{35} & S_{45} & S_{55} & S_{56} & S_{45} & S_{55} & S_{56} \\
S_{16} & S_{26} & S_{36} & S_{46} & S_{56} & S_{66} & S_{46} & S_{56} & S_{66} \\
S_{14} & S_{24} & S_{34} & S_{44} & S_{45} & S_{46} & S_{44} & S_{45} & S_{46} \\
S_{15} & S_{25} & S_{35} & S_{45} & S_{55} & S_{56} & S_{45} & S_{55} & S_{56} \\
S_{16} & S_{26} & S_{36} & S_{46} & S_{56} & S_{66} & S_{46} & S_{56} & S_{66}
\end{pmatrix}
\begin{pmatrix}
\sigma_1 \\
\sigma_2 \\
\sigma_3 \\
\sigma_4 \\
\sigma_5 \\
\sigma_6 \\
\sigma_4 \\
\sigma_5 \\
\sigma_6
\end{pmatrix}
\tag{A.7}
$$

Contracted tensor notation

$$
\begin{pmatrix}
\sigma_1 \\
\sigma_2 \\
\sigma_3 \\
\sigma_4 \\
\sigma_5 \\
\sigma_6 \\
\sigma_4 \\
\sigma_5 \\
\sigma_6
\end{pmatrix}
=
\begin{pmatrix}
C_{11} & C_{12} & C_{13} & C_{14} & C_{15} & C_{16} & C_{14} & C_{15} & C_{16} \\
C_{12} & C_{22} & C_{23} & C_{24} & C_{25} & C_{26} & C_{24} & C_{25} & C_{26} \\
C_{13} & C_{23} & C_{33} & C_{34} & C_{35} & C_{36} & C_{34} & C_{35} & C_{36} \\
C_{14} & C_{24} & C_{34} & C_{44} & C_{45} & C_{46} & C_{44} & C_{45} & C_{46} \\
C_{15} & C_{25} & C_{35} & C_{45} & C_{55} & C_{56} & C_{45} & C_{55} & C_{56} \\
C_{16} & C_{26} & C_{36} & C_{46} & C_{56} & C_{66} & C_{46} & C_{56} & C_{66} \\
C_{14} & C_{24} & C_{34} & C_{44} & C_{45} & C_{46} & C_{44} & C_{45} & C_{46} \\
C_{15} & C_{25} & C_{35} & C_{45} & C_{55} & C_{56} & C_{45} & C_{55} & C_{56} \\
C_{16} & C_{26} & C_{36} & C_{46} & C_{56} & C_{66} & C_{46} & C_{56} & C_{66}
\end{pmatrix}
\begin{pmatrix}
\epsilon_1 \\
\epsilon_2 \\
\epsilon_3 \\
\frac{\gamma_4}{2} \\
\frac{\gamma_5}{2} \\
\frac{\gamma_6}{2} \\
\frac{\gamma_4}{2} \\
\frac{\gamma_5}{2} \\
\frac{\gamma_6}{2}
\end{pmatrix}
\tag{A.8}
$$

After summing all of the tensors in equations 14 and 15 it becomes clear that the matrices can be represented in 6x6 form.

C-Matrix

$$
\begin{pmatrix}
\sigma_1 \\
\sigma_2 \\
\sigma_3 \\
\sigma_4 \\
\sigma_5 \\
\sigma_6
\end{pmatrix}
=
\begin{pmatrix}
C_{11} & C_{12} & C_{13} & C_{14} & C_{15} & C_{16} \\
C_{12} & C_{22} & C_{23} & C_{24} & C_{25} & C_{26} \\
C_{13} & C_{23} & C_{33} & C_{34} & C_{35} & C_{36} \\
C_{14} & C_{24} & C_{34} & C_{44} & C_{45} & C_{46} \\
C_{15} & C_{25} & C_{35} & C_{45} & C_{55} & C_{56} \\
C_{16} & C_{26} & C_{36} & C_{46} & C_{56} & C_{66}
\end{pmatrix}
\begin{pmatrix}
\epsilon_1 \\
\epsilon_2 \\
\epsilon_3 \\
\gamma_4 \\
\gamma_5 \\
\gamma_6
\end{pmatrix}
\tag{A.9}
$$

S-Matrix

$$
\begin{pmatrix}
\epsilon_1 \\
\epsilon_2 \\
\epsilon_3 \\
\gamma_4 \\
\gamma_5 \\
\gamma_6
\end{pmatrix}
=
\begin{pmatrix}
S_{11} & S_{12} & S_{13} & 2S_{14} & 2S_{15} & 2S_{16} \\
S_{12} & S_{22} & S_{23} & 2S_{24} & 2S_{25} & 2S_{26} \\
S_{13} & S_{23} & S_{33} & 2S_{34} & 2S_{35} & 2S_{36} \\
2S_{14} & 2S_{24} & 2S_{34} & 4S_{44} & 4S_{45} & 4S_{46} \\
2S_{15} & 2S_{25} & 2S_{35} & 4S_{45} & 4S_{55} & 4S_{56} \\
2S_{16} & 2S_{26} & 2S_{36} & 4S_{46} & 4S_{56} & 4S_{66}
\end{pmatrix}
\begin{pmatrix}
\sigma_1 \\
\sigma_2 \\
\sigma_3 \\
\sigma_4 \\
\sigma_5 \\
\sigma_6
\end{pmatrix}
\tag{A.10}
$$

Standard notation in voigt and nye is then used multiplied by factor $\phi$ to further simplify the matrices [31, 69–71].

93

$$
\begin{pmatrix} \epsilon_1 \\ \epsilon_2 \\ \epsilon_3 \\ \gamma_4 \\ \gamma_5 \\ \gamma_6 \end{pmatrix} = \begin{pmatrix} S_{11} & S_{12} & S_{13} & S_{14} & S_{15} & S_{16} \\ S_{12} & S_{22} & S_{23} & S_{24} & S_{25} & S_{26} \\ S_{13} & S_{23} & S_{33} & S_{34} & S_{35} & S_{36} \\ S_{14} & S_{24} & S_{34} & S_{44} & S_{45} & S_{46} \\ S_{15} & S_{25} & S_{35} & S_{45} & S_{55} & S_{56} \\ S_{16} & S_{26} & S_{36} & S_{46} & S_{56} & S_{66} \end{pmatrix} \begin{pmatrix} \sigma_1 \\ \sigma_2 \\ \sigma_3 \\ \sigma_4 \\ \sigma_5 \\ \sigma_6 \end{pmatrix}
\tag{A.11}
$$

Due to centers of symmetry, from things such as inversions and rotations the coefficients in equations 17 and 18 can be further reduced from 36 down to 12.

$$
\begin{pmatrix} \epsilon_1 \\ \epsilon_2 \\ \epsilon_3 \\ \gamma_4 \\ \gamma_5 \\ \gamma_6 \end{pmatrix} = \begin{pmatrix} S_{11} & S_{12} & S_{13} & \bullet & \bullet & \bullet \\ S_{12} & S_{22} & S_{23} & \bullet & \bullet & \bullet \\ S_{13} & S_{23} & S_{33} & \bullet & \bullet & \bullet \\ \bullet & \bullet & \bullet & S_{44} & \bullet & \bullet \\ \bullet & \bullet & \bullet & \bullet & S_{55} & \bullet \\ \bullet & \bullet & \bullet & \bullet & \bullet & S_{66} \end{pmatrix} \begin{pmatrix} \sigma_1 \\ \sigma_2 \\ \sigma_3 \\ \sigma_4 \\ \sigma_5 \\ \sigma_6 \end{pmatrix}
\tag{A.12}
$$

$$
\begin{pmatrix} \sigma_1 \\ \sigma_2 \\ \sigma_3 \\ \sigma_4 \\ \sigma_5 \\ \sigma_6 \end{pmatrix} = \begin{pmatrix} C_{11} & C_{12} & C_{13} & \bullet & \bullet & \bullet \\ C_{12} & C_{22} & C_{23} & \bullet & \bullet & \bullet \\ C_{13} & C_{23} & C_{33} & \bullet & \bullet & \bullet \\ \bullet & \bullet & \bullet & C_{44} & \bullet & \bullet \\ \bullet & \bullet & \bullet & \bullet & C_{55} & \bullet \\ \bullet & \bullet & \bullet & \bullet & \bullet & C_{66} \end{pmatrix} \begin{pmatrix} \epsilon_1 \\ \epsilon_2 \\ \epsilon_3 \\ \gamma_4 \\ \gamma_5 \\ \gamma_6 \end{pmatrix}
\tag{A.13}
$$

# Appendix B

# Piezo Electric matrix expression

Continuing from the peizoelectric section, the matrices can be multiplied out fully to give the following expressions:

$$
\begin{pmatrix} T_1 \\ T_2 \\ T_3 \\ T_4 \\ T_5 \\ T_6 \end{pmatrix} = \begin{pmatrix} c_{11} & c_{12} & c_{13} & c_{14} & c_{15} & c_{16} \\ & c_{22} & c_{23} & c_{24} & c_{25} & c_{26} \\ & & c_{33} & c_{34} & c_{35} & c_{36} \\ & & & c_{44} & c_{45} & c_{46} \\ & & & & c_{55} & c_{56} \\ & & & & & c_{66} \end{pmatrix} \begin{pmatrix} S_1 \\ S_2 \\ S3 \\ S_4 \\ S_5 \\ S_6 \end{pmatrix} - \begin{pmatrix} e_{11} & e_{21} & e_{31} \\ e_{12} & e_{22} & e_{32} \\ e_{13} & e_{23} & e_{33} \\ e_{14} & e_{24} & e_{34} \\ e_{15} & e_{25} & e_{35} \\ e_{16} & e_{26} & e_{36} \end{pmatrix} \begin{pmatrix} E_1 \\ E_2 \\ E_3 \end{pmatrix}
\tag{B.1}
$$

$$
\begin{pmatrix} D_1 \\ D_2 \\ D_3 \end{pmatrix} = \begin{pmatrix} \epsilon_1 & \epsilon_6 & \epsilon_5 \\ & \epsilon_2 & \epsilon_4 \\ & & \epsilon_3 \end{pmatrix} \begin{pmatrix} E_1 \\ E_2 \\ E_3 \end{pmatrix} + \begin{pmatrix} e_{11} & e_{12} & e_{13} & e_{14} & e_{15} & e_{16} \\ e_{21} & e_{22} & e_{23} & e_{24} & e_{25} & e_{26} \\ e_{31} & e_{32} & e_{33} & e_{34} & e_{35} & e_{36} \end{pmatrix} \begin{pmatrix} S_1 \\ S_2 \\ S3 \\ S_4 \\ S_5 \\ S_6 \end{pmatrix}
\tag{B.2}
$$

Due to the hexagonal, Wurtzite form of Aluminum Nitride the matrix form can be dramatically reduced as shown previously in the elastic section.

$$
\begin{pmatrix} T_1 \\ T_2 \\ T_3 \\ T_4 \\ T_5 \\ T_6 \end{pmatrix} = \begin{pmatrix} c_{11} & c_{12} & c_{13} & 0 & 0 & 0 \\ & c_{11} & c_{12} & 0 & 0 & 0 \\ & & c_{33} & 0 & 0 & 0 \\ & & & c_{44} & 0 & 0 \\ & & & & c_{55} & 0 \\ & & & & & c_{66} \end{pmatrix} \begin{pmatrix} S_1 \\ S_2 \\ S_3 \\ S_4 \\ S_5 \\ S_6 \end{pmatrix} - \begin{pmatrix} 0 & 0 & e_{31} \\ 0 & 0 & e_{31} \\ 0 & 0 & e_{31} \\ 0 & e_{15} & 0 \\ e_{15} & 0 & 0 \\ 0 & 0 & 0 \end{pmatrix} \begin{pmatrix} E_1 \\ E_2 \\ E3 \end{pmatrix}
\tag{B.3}
$$

$$
\begin{pmatrix} D_1 \\ D_2 \\ D_3 \end{pmatrix} = \begin{pmatrix} \epsilon_1 & 0 & 0 \\ & \epsilon_2 & 0 \\ & & \epsilon_3 \end{pmatrix} \begin{pmatrix} E_1 \\ E_2 \\ E_3 \end{pmatrix} + \begin{pmatrix} 0 & 0 & 0 & 0 & e_{15} & 0 \\ 0 & 0 & 0 & e_{24} & 0 & 0 \\ e_{31} & e_{32} & e_{33} & 0 & 0 & 0 \end{pmatrix} \begin{pmatrix} S_1 \\ S_2 \\ S_3 \\ S_4 \\ S_5 \\ S_6 \end{pmatrix}
\tag{B.4}
$$

Table B.1: **Material properties of Aluminum Nitride [9]**

| Elastic Matrix in Stiffness Form (x $10^{11}$ Pa) | | Piezoelectric Matrix at Constant Stain ($\frac{C}{m^2}$) | | Permittivity Matrix at Constant Strain (x$10^{-11}$ $\frac{F}{m}$) | |
|---|---|---|---|---|---|
| $C_{11}$ | 3.45 | $e_{l5}$ | -0.48 | $\epsilon_{11}$ | 8 |
| $C_{12}$ | 1.25 | $e_{31}$ | -0.58 | $\epsilon_{33}$ | 9.5 |
| $C_{13}$ | 1.2 | $e_{33}$ | 1.55 | | |
| $C_{33}$ | 3.95 | | | | |
| $C_{44}$ | 1.18 | | | | |
| $C_{66}$ | $\frac{c_{11}-c_{12}}{2} = 1.1$ | | | | |

| Property | Units | AlN |
|---|---|---|
| Density | $\frac{kg}{m^3}$ | 3230 |
| Piezoelectric Constant | $\frac{C}{m^2}$ | $e_{31} = $ -0.58 |
| | | $e_{33} = 1.55$ |
| Thermal conductivity | $\frac{W}{cm \cdot {}^oC}$ | 2.85 |
| Thermal expansion | $\frac{1}{{}^oC}$ | $\alpha_a = 4.2 \cdot 10^{-6}$ |
| | | $\alpha_c = 5.3 \cdot 10^{-6}$ |
| Young's modulus | | 308 |
| Acoustic velocity | $\frac{m}{s}$ | 10,127 |
| Index of refraction | $\frac{m}{s}$ | 2.08 |
| Band gap | (eV) $\frac{m}{s}$ | 6.2 |
| Resistivity | ($\Omega$·cm) | $1 \cdot 10^{11}$ |

Table B.2: **Properties of Aluminum Nitride [10]**

Tables B.1 and B.2 are the elastic, piezoelectric and dielectric material properties of Aluminum Nitride.

Stiffness Matrix of Aluminum Nitride

$$c = \begin{pmatrix} 3.45 & 1.25 & 1.2 & 0 & 0 & 0 \\ 1.25 & 3.45 & 1.2 & 0 & 0 & 0 \\ 1.2 & 1.2 & 3.95 & 0 & 0 & 0 \\ 0 & 0 & 0 & 1.18 & 0 & 0 \\ 0 & 0 & 0 & 0 & 1.18 & 0 \\ 0 & 0 & 0 & 0 & 0 & 1.1 \end{pmatrix} \tag{B.5}$$

Piezoelectric Matrix of Aluminum Nitride

$$e = \begin{pmatrix} 0 & 0 & 0 & 0 & -0.48 & 0 \\ 0 & 0 & 0 & -0.48 & 0 & 0 \\ -0.58 & -0.58 & 1.55 & 0 & 0 & 0 \end{pmatrix} \tag{B.6}$$

Dielectric stress matrix of Aluminum Nitride

$$\epsilon = \begin{pmatrix} 8.0 & 0 & 0 \\ 0 & 8.0 & 0 \\ 0 & 0 & 9.5 \end{pmatrix} \tag{B.7}$$

The above three matrices are used in the following finite element analysis simulations which are used to inform this thesis' device design.

# Appendix C

# External Links

The following links are videos, that have been created by the author of this thesis to aid in understanding of the simulation work.

**Contour Mode Resonator Simulations**
www.youtube.com/watch?v=O_sNTAZFEIg

**Microelectronics by Josh Melnick**
www.youtube.com/watch?v=BdLMs_ucpAo

**SAW BAW CMR Time Dependent Simulations**
www.youtube.com/watch?v=eQZsMNjSKcg

**Bulk Acoustic Wave BAW COMSOL Simulation Training Video**
www.youtube.com/watch?v=AQ-oRgGIGdc

[Contour Mode Resonator Simulations](#)

[Microelectronics by Josh Melnick](#)

[SAW BAW CMR Time Dependent Simulations](#)

[Bulk Acoustic Wave BAW COMSOL Simulation Training Video](#)

# Appendix D

# CV Test Measurement



Measurement Report
R.I.T
IHT 2014-014, May 19th, 2014

# Sample parameters

- 2 Samples
- C-V testing
- Area [mm²] : 0.1257
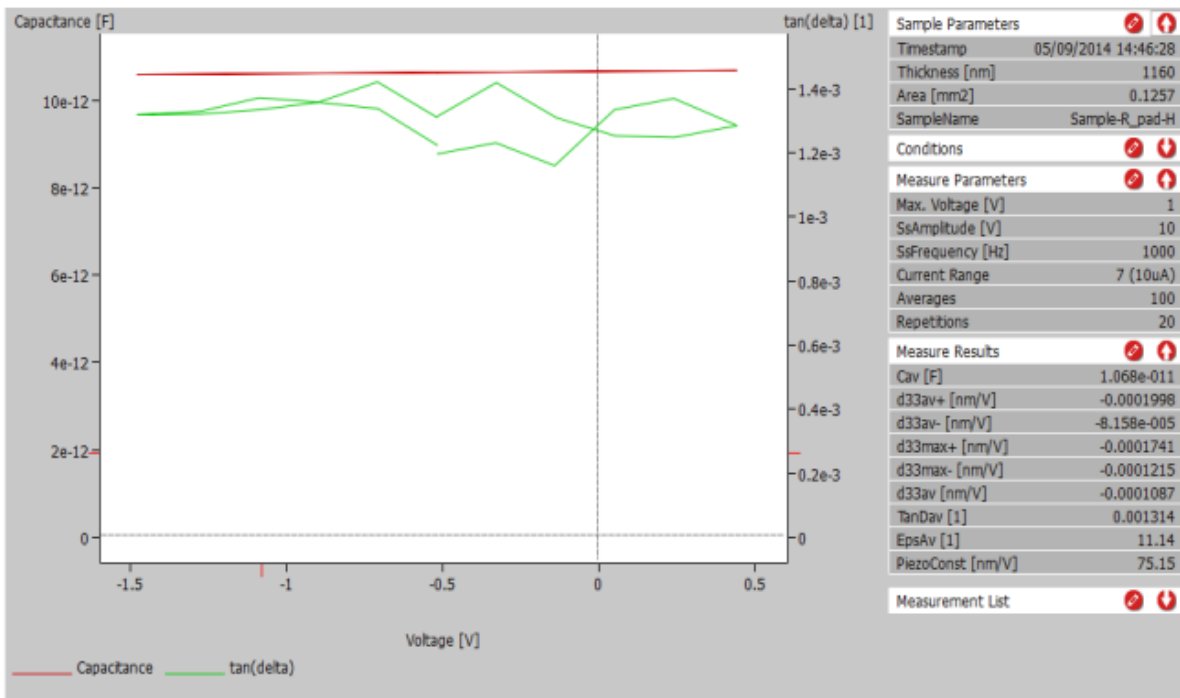- Capacitor: H
- Diameter: 400um

| Die | Thickness [μm] |
|-----|----------------|
| R | 1.16 |
| Z | 1.125 |

# C-V coefficient measurements

| | Sample-R_pad-H | Sample-Z_pad-H |
|---|---|---|
| PiezoConst [nm/V] | 75.1507 | 75.1507 |
| DBLIDevpp [1] | 0.0199964 | 0.0171794 |
| DBLIDev [1] | 0.270945 | 0.270649 |
| Cav [F] | 1.06828e-011 | 1.08481e-011 |
| EpsAv [1] | 11.1374 | 10.9685 |
| TanDmax [1] | 0.00142695 | 0.000274621 |
| TanDav [1] | 0.00131397 | -0.000160189 |
| d33av [nm/V] | -0.000108716 | -0.000115563 |
| d33av+0 [nm/V] | -0.000246259 | -0.000119149 |
| d33av+ [nm/V] | -0.000199779 | -0.000142901 |
| Md33av+ [nm/V2] | 0.000160815 | 4.5402e-005 |
| d33av-0 [nm/V] | -0.000212259 | 0.000209379 |
| d33av- [nm/V] | -8.15816e-005 | -9.50212e-005 |
| Md33av- [nm/V2] | -6.10518e-005 | 0.000268251 |
| C0+ [F] | 1.07097e-011 | 1.0849e-011 |
| Cmax+ [F] | 1.07307e-011 | 1.08488e-011 |
| Cmax- [F] | 1.06325e-011 | 1.08463e-011 |
| d33max+ [nm/V] | -0.000174051 | -9.87094e-005 |
| d33max- [nm/V] | -0.000121532 | -0.000188588 |

# Die R    pad H



Capacitance [F] / tan(delta) [1] vs Voltage [V]

| Sample Parameters | |
|---|---|
| Timestamp | 05/09/2014 14:46:28 |
| Thickness [nm] | 1160 |
| Area [mm2] | 0.1257 |
| SampleName | Sample-R_pad-H |

| Conditions | |
|---|---|

| Measure Parameters | |
|---|---|
| Max. Voltage [V] | 1 |
| SsAmplitude [V] | 10 |
| SsFrequency [Hz] | 1000 |
| Current Range | 7 (10uA) |
| Averages | 100 |
| Repetitions | 20 |

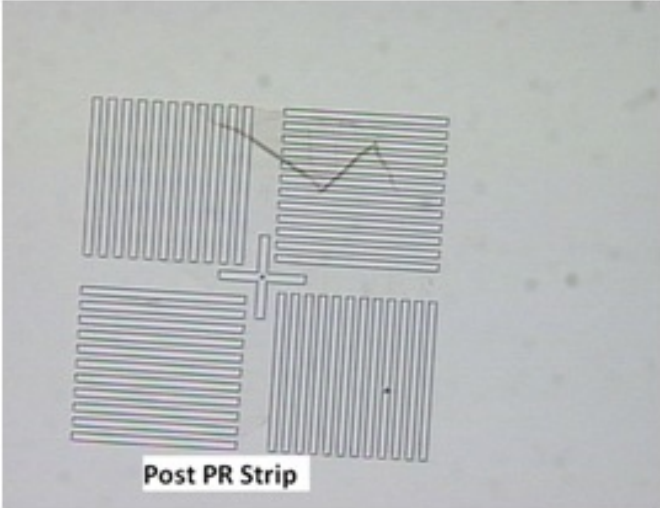| Measure Results | |
|---|---|
| Cav [F] | 1.068e-011 |
| d33av+ [nm/V] | -0.0001998 |
| d33av- [nm/V] | -8.158e-005 |
| d33max+ [nm/V] | -0.0001741 |
| d33max- [nm/V] | -0.0001215 |
| d33av [nm/V] | -0.0001087 |
| TanDav [1] | 0.001314 |
| EpsAv [1] | 11.14 |
| PiezoConst [nm/V] | 75.15 |

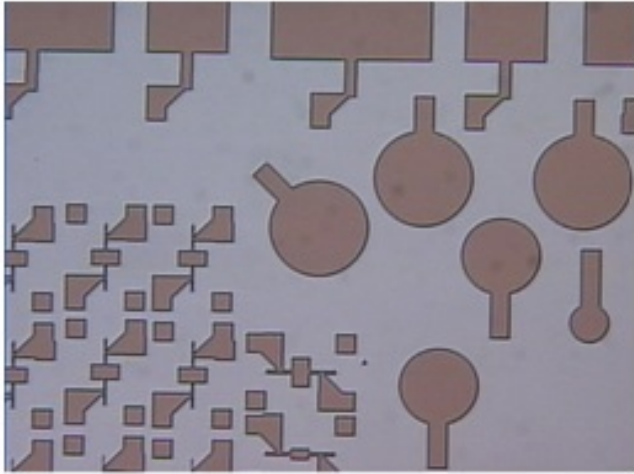| Measurement List | |
|---|---|

4

ADVANCED CUSTOMIZED CHARACTERIZATION TECHNOLOGIES

# Appendix E

# AlN Resonators Process Flow
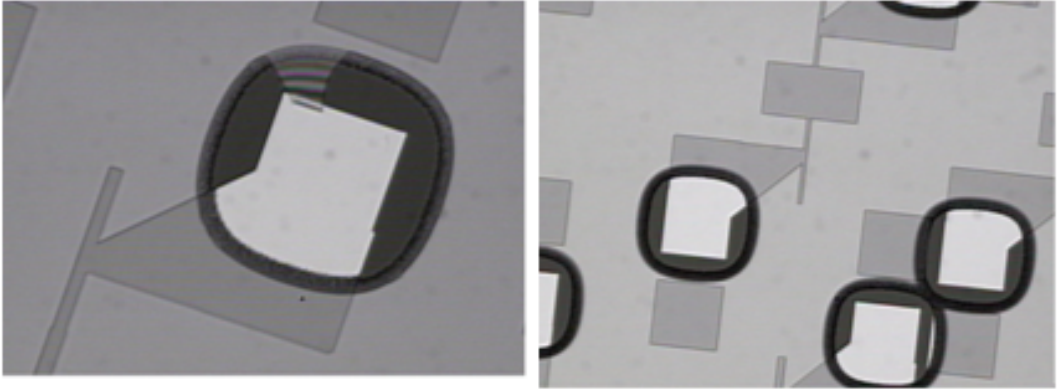
| Process Flow ALN Resonators and IRD | |
| --- | --- |
| By Josh Melnick | |
| Advisor Dr. Puchades | |

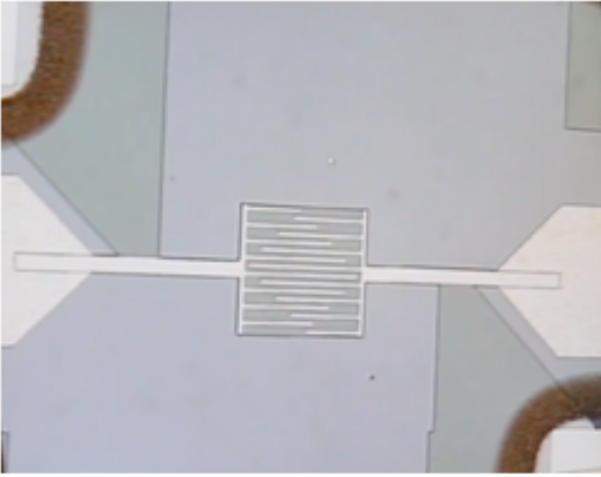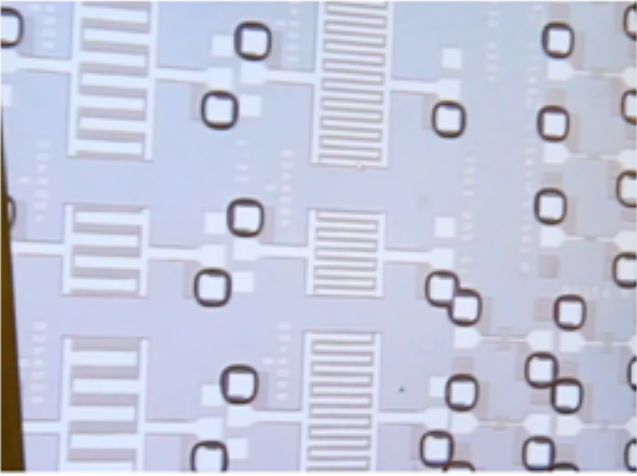| Step | ALN Resonators |
| --- | --- |
| 1 | 1. Standard Coat SSI Track<br>2. Expose (0-Layer Mask)<br>3. Develop<br><br>Alignment Marks 0-Layer |
| 2 | Etch in Drytek<br>ZeroEtch<br>100mT, 200W<br>$CF_4 = 25$, $C_3F =50$, $0_2 =10$ |

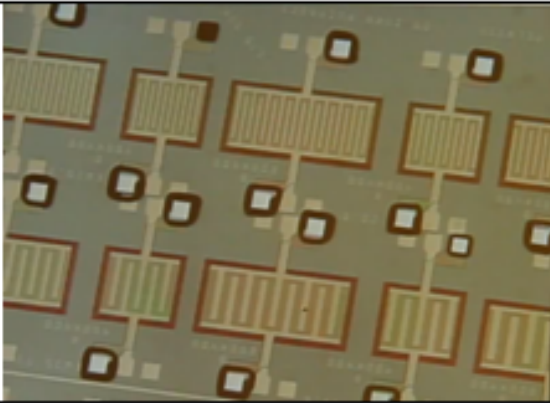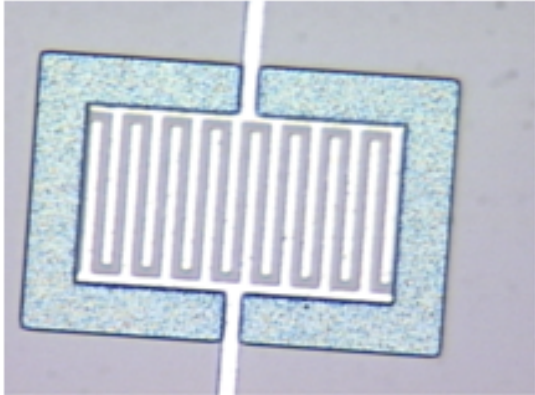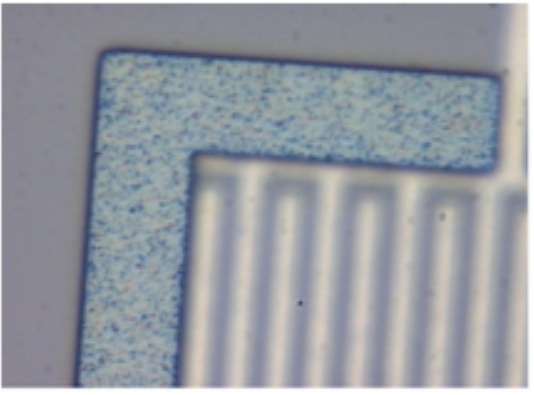| | |
|---|---|
| | Post ZeroEtch |
| 3 | Solvent Strip<br>5min + 5min +5min |
| 4 | SRD<br>Post PR Strip |
| 5 | RCA Standard Clean |

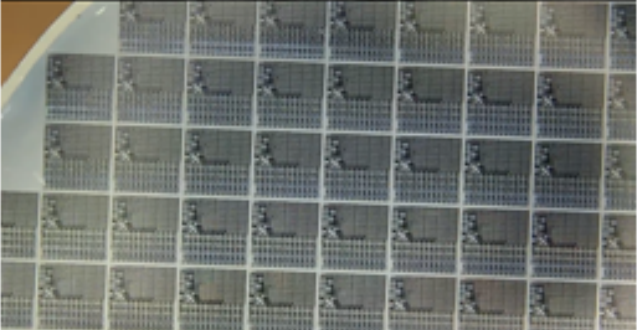| | |
|---|---|
| 6 | SRD |
| 7 | Bruce Tube<br>Grow 2000Å of Oxide |
| 8 | CVC 601<br>Deposit Molybdenum<br>1000 seconds, 1000 Watts, 5mTorr Chamber Pressure<br>Argon 30 Sccm |
| 9 | 1. Standard Coat SSI Track<br>2.Expose BOTTOM ELECTRODE (Clear Field)<br>Standard Exposure<br>Job: Puchades<br>Level 1<br>3. Develop<br><br>Moly Post BottomElectrode Exposure 2.5x jan31 |
| 10 | Etch Molybdenum In DryTek Quad<br>Moly Etch Recipe??? |

| | |
|---|---|
| 11 | **Solvent Strip**<br>**5min + 5min +5min**<br><br>Moly Post Solvent Strip Bottom Electrode 2.5x     Post MOLY ETCH DRYTEK QUAD RECIPE MOLY 20x |
| 12 | **AlN Deposition**<br>**1000 Watts, 15 Sccm N, 15 Sccm Ar, 3mTorr**<br>**45min = ~1um** |
| 13 | <br>Moly post AlN deposition 10x     Moly Post AlN Depostion |
| 14 | **1. Standard Coat SSI Track**<br>**2.Expose (CONTACT layer Dark Field)** |

| | |
|---|---|
| | Standard Exposure<br>Job: Puchades<br>Level 2<br>3. Develop<br><br><br><br>Moly Post Contact Layer Exposure/Development 2.5x    Moly Post Contact Layer Exposure/Development 20x |
| 15 | AlN Wet Etch<br>Etch in Phosphoric Acid 90°C<br>2000A/min<br>~35min<br>Rinse in DI 5min |
| 16 | SRD |

Moly post Phosphoric Etch 30min 85C 20x

Moly Post Phos Etch and Contact Cut PR Strip 10x

| | | |
|---|---|---|
| | 1. Standard Coat SSI Track<br>2. Expose TOP ELECTRODE (Clear Field)<br>Standard Exposure<br>Job: Puchades<br>Level 3<br>3. Develop | |
| 17 | Evaporate Aluminum CVC601<br>A single pellet of Aluminum was used to deposit upon two wafers one of Molybdenum bottom electrode and one of a poly bottom electrode | |
| 18 | Remove Metal with bath of Acetone | |
| 19 | Solvent Strip<br>5min + 5min +5min | |
| 20 | SRD | |

| | | |
|---|---|---|
| |  | |
| 21 | 1. Standard Coat SSI Track<br>2. Expose (MOAT layer Dark Field)<br>Job: Puchades<br>Level 4<br>3. Develop | |

| | |
|---|---|
| |  |
| 22 | Etch Native Oxide on Silicon |
| 23 | LAM4600  Moly post LAM4600 etch#4 50x (4)    Moly post LAM4600 etch#4 100x (5) |
| 24 | 1. Standard Coat SSI Track<br>2. Expose (MOAT layer Dark Field)<br>Job: Puchades<br>Level 4<br>3. Develop |
| 26 | Wafer Saw<br>The die were cut into individual chips with the |

| | |
|---|---|
| 27 | Etch in Drytek Quad<br>ZeroEtch<br>100mT, 200W<br>$CF_4 = 25$, $C_3F = 50$, $O_2 = 10$ |
| 28 | Xactic<br>Ething Si in $XeF_2$<br>The Xactic Tool was used to release the structures from the Silicon wafer. A series of cycles of $XeF_2$ was used with a cycle time of 60seconds each, the Nitrogen Carrier gas was at 4mT, and Argon at 3.3mT. Between 8 to 12 cycles were performed to release the structures from the wafer. 8 cycles was found to be ineffective so it was increased to 12 cycles with the tool. It may be the result of a large open area on the mask that was exposed Silicon, which may have reacted with a large part of the $XeF_2$. |
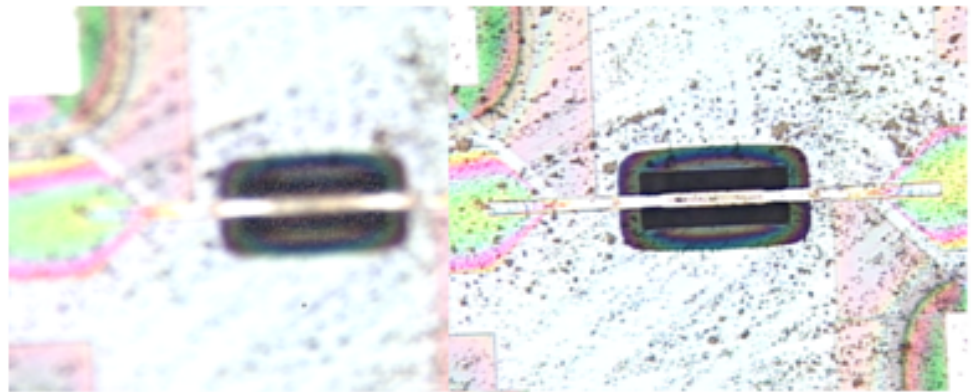
Moly post XeF2 etch 50x (Die A) (Pic 3 of 5)



Moly post XeF2 etch 10x (Die A) (Pic 4 of 5)



Moly post XeF2 etch 20x (Die A) (Pic 5 of 5)

| 29 | Gasonics Aura 1000 Asher<br>Ash Recipe was used to remove the resist, due to the structure already being Released it wasn't possible to use the solvent strip. Recipe 111 was used which is 180 seconds of a Oxygen and Nitrogen plasma which is a highly reactive plasma that reacts strongly to hydrocarbon compounds such as photo resist; which effectively burns the photo resist.Molybdenum was found to be oxidized by the Gasonics, it was found however that theAluminum Top Electrode also covering the Molybdenum was effective in prevent the Moly underneath it from being oxidized and provided a protection. Later DC measurements confirmed that the resistance was still well within an acceptable |
|---|---|
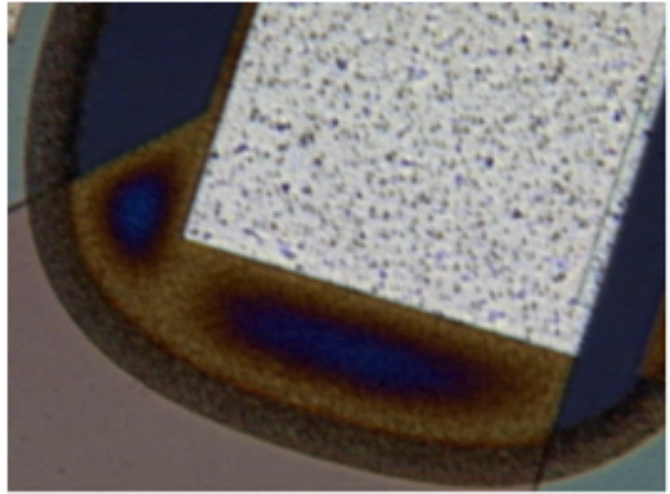
range being as low as 14Ω.

# Appendix F

# Aluminum Nitride Resonators Breakdown voltage

## AlN Breakdown Test

- AlN theoretical BV 1.6-1.8 MV/cm
- Capacitors of various sizes
- Moly or Polvsilicon bottom electrode
- Top electrode is aluminum
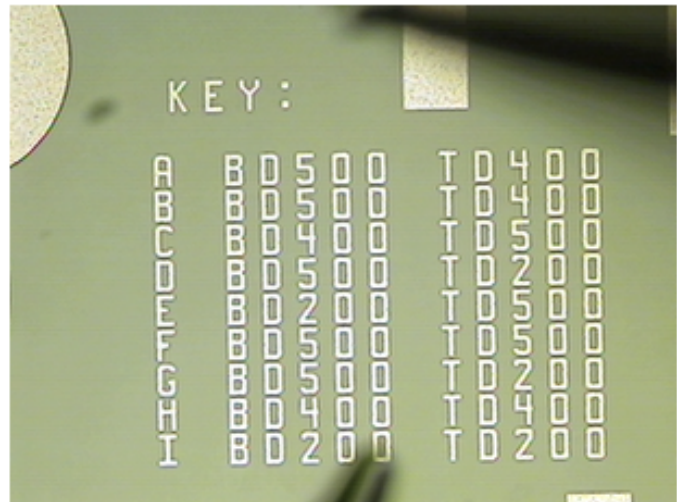
# AlN capacitor – C
# BD 400un, TD 500um
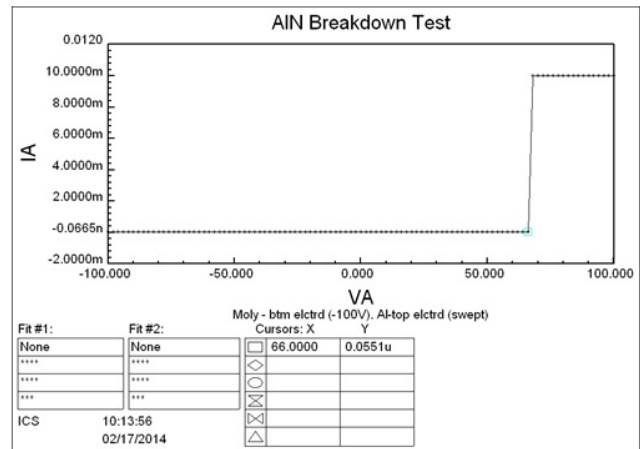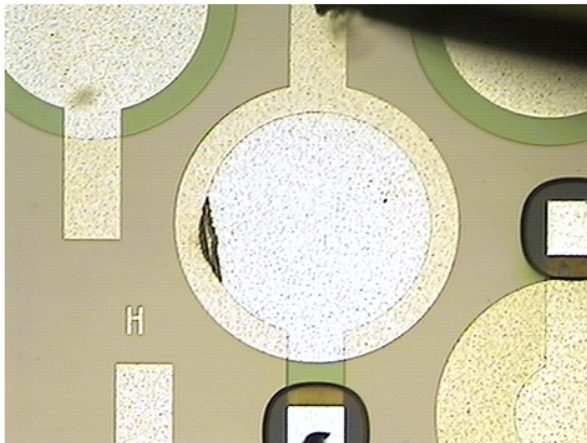


# AlN capacitor – A
# BD 500un, TD 400um
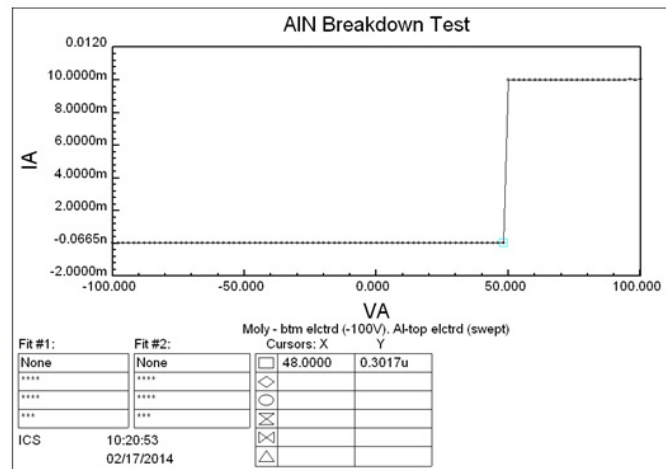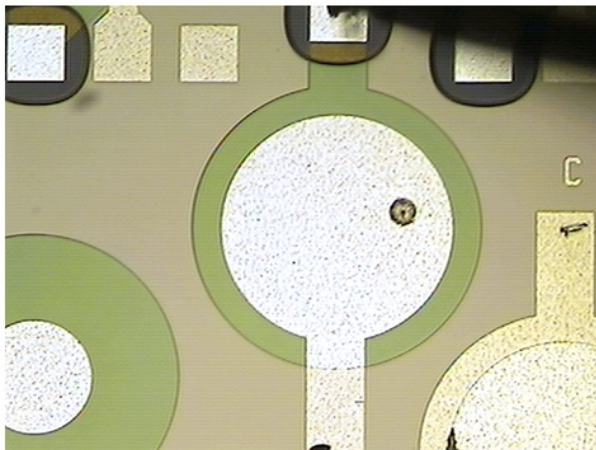
# AlN capacitor – C Poly
# BD 400un, TD 500um
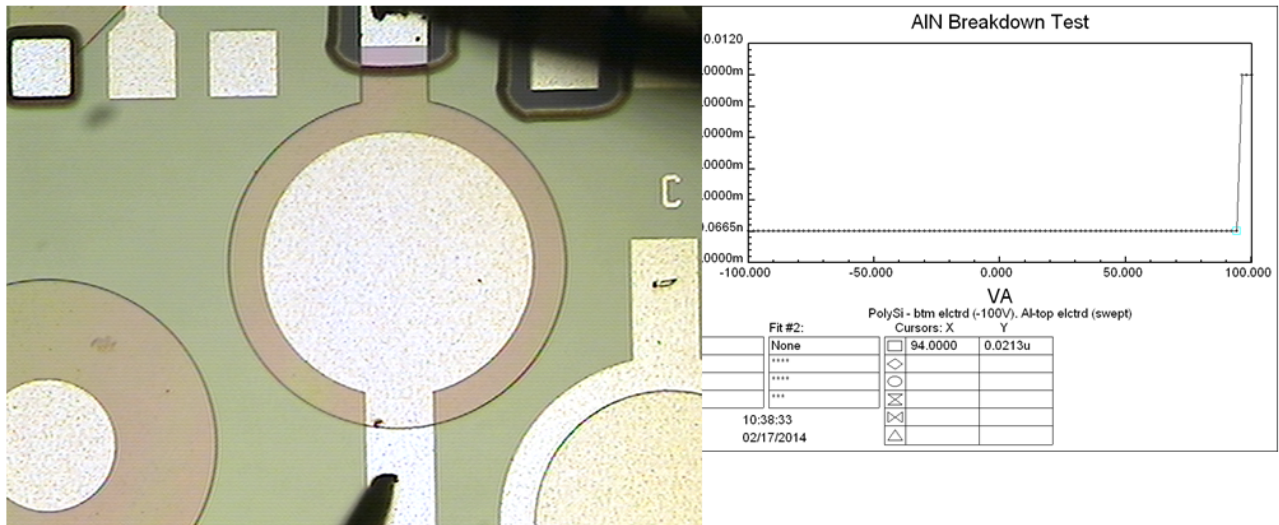
# Appendix G

# Aluminum Nitride Resonators SEM Micrographs

Figure G.1:  **SEM Micrographs of Resonator at 424 magnification**
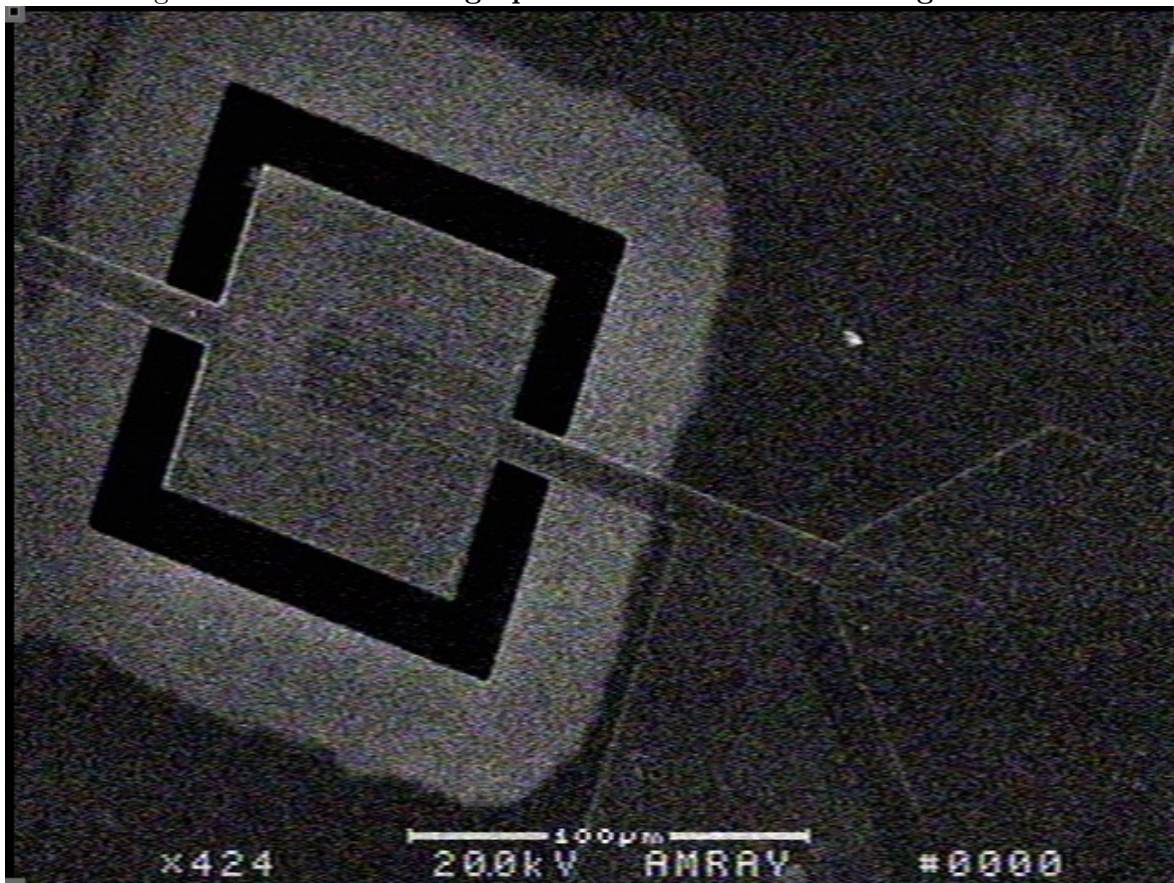


Micrographs of Interdigitated fingers of a RF MEMS resonator

Figure G.2:  **SEM Micrographs of Resonator at 5250 magnification**
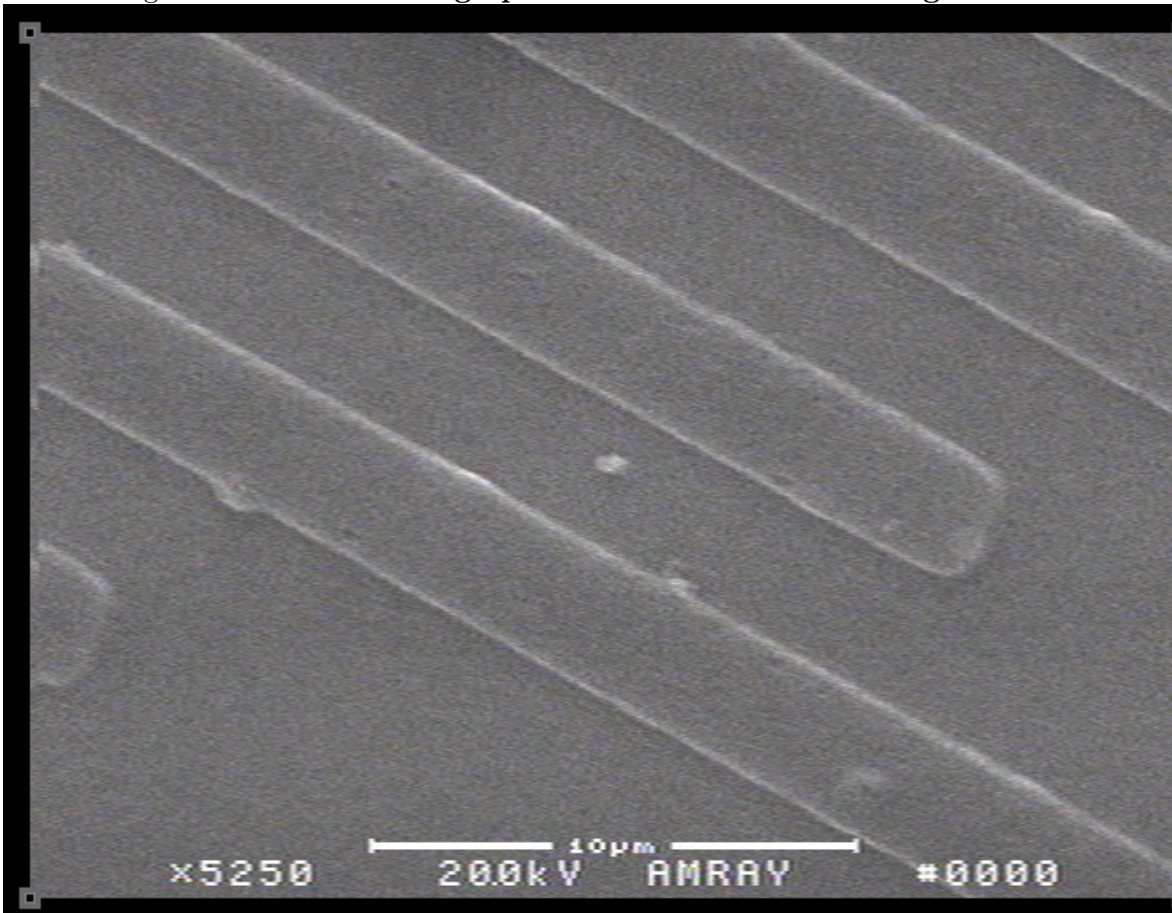


SEM Micrographs of Resonator

Figure G.3: **SEM Micrographs of Resonator at 4840 magnification**
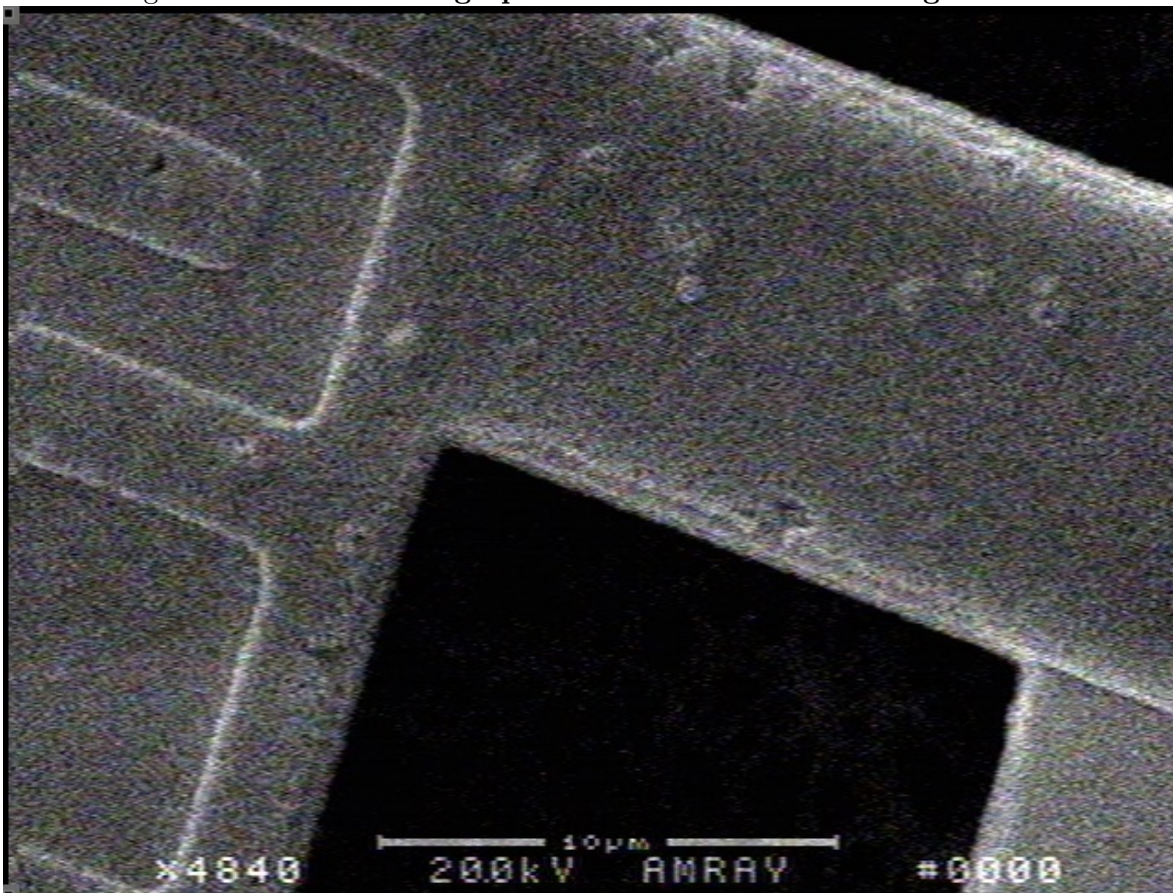


Micrographs of RF MEMS resonator tether

# Bibliography

[1] Yole Développement Press Release. MEMS will continue to see steady, sustainable double digit growth for the next six years. market, July 2012.

[2] Ching-Liang Dai, Jin-Yu Hong, and Mao-Chen Liu. High Q-factor CMOS-MEMS inductor. In *Design, Test, Integration and Packaging of MEMS/MOEMS, 2008. MEMS/MOEMS 2008. Symposium on*, pages 138–141. IEEE, April 2008.

[3] Thomas M. Adams and Richard A. Layton. *Introductory MEMS: Fabrication and Applications.* Springer, 2010 edition, December 2009.

[4] James H. Edgar. *Properties of group III nitrides.* INSPEC, Institution of Electrical Engineers, 1994.

[5] Piazza. One and Two Port Piezoelectric Higher Order Contour-Mode MEMS Resonators for Mechanical Signal Processing. *Solid-State Electronics*, 51:1596–1608, 2007. design14.

[6] Zoher Z. Karu. *Signals and Systems Made Ridiculously Simple.* Zizi Pr, 1 edition. apod9.

[7] Understanding FFT Windows. lds-group.com, 2003. apod15.

[8] Janine Conde. *High coupling materials for thin film bulk acoustic wave resonators.* PhD thesis, STI, Lausanne, 2009. acoustic4.

[9] Mohamed M. El Gowini and Walied A. Moussa. A Reduced Three Dimensional Model for SAW Sensors Using Finite Element Analysis. *Sensors (Basel, Switzerland)*, 9(12):9945–9964, 2009.

[10] Seth E. Boeshore. *Aluminum Nitride Thin Films on Titanium: Piezoelectric Transduction on a Metal Substrate.* PhD thesis, University of California Santa Barbara, 300 North Zeeb Road P.O. Box 1346 Ann Arbor, MI 48106-1346, 2006. COMSOLabab.

[11] Oswald Spengler. *Man and technics : a contribution to a philosophy of life.* University Press of the Pacific, June 2002.

[12] Oswald Spengler. *The Decline of the West: Volume I, Form and Actuality, and Volume II, Perspectives of World-History [Two Volume Set].* Alfred A. Knopf.

[13] Ernst Junger. *The Glass Bees (New York Review Books Classics).* NYRB Classics, September 2000.

[14] Gianluca Piazza. MEMS Resonators for Frequency Control and Sensing Applications.

[15] C. T. C. Nguyen. Vibrating RF MEMS for next generation wireless applications. In *Proceedings of the IEEE 2004 Custom Integrated Circuits Conference (IEEE Cat. No.04CH37571)*, pages 257–264. IEEE, 2004.

[16] George C. King. *Vibrations and waves*. Wiley, 2009.

[17] S. N. Sen. *Acoustics Waves and Oscillations*. New Academic Science, August 2013.

[18] David P. Morgan. History of SAW devices. In *Frequency Control Symposium, 1998. Proceedings of the 1998 IEEE International*, pages 439–460. IEEE, May 1998.

[19] Jun Kondoh and Showko Shiokawa. A liquid sensor based on a shear horizontal saw device. *Electron. Comm. Jpn. Pt. II*, 76(2):69–82, January 1993.

[20] Kerstin Länge, Bastian E. Rapp, and Michael Rapp. Surface acoustic wave biosensors: a review. *Analytical and bioanalytical chemistry*, 391(5):1509–1519, July 2008.

[21] *Advances in Surface Acoustic Wave Technology, Systems and Applications Volume 2*. World Scientific Pub Co Inc, 1st edition, January 2001.

[22] S. Saib and N. Bouarissa. Electronic properties and elastic constants of wurtzite, zinc-blende and rocksalt AlN. *Journal of Physics and Chemistry of Solids*, 67(8):1888–1892, August 2006. aln2.

[23] Hadis Morkoç. General Properties of Nitrides. pages 1–129, 2009.

[24] Anurag Srivastava and Neha Tyagi. Pressure induced zincblende to rocksalt phase transition in AlN nanocrystal. *Journal of Physics: Conference Series*, 377(1):012066+, July 2012.

[25] J. Li, K. B. Nam, M. L. Nakarmi, J. Y. Lin, H. X. Jiang, Pierre Carrier, and Su H. Wei. Band structure and fundamental optical transitions in wurtzite AlN. *Applied Physics Letters*, 83(25):5163–5165, 2003.

[26] C. T. Foxon, T. S. Cheng, S. V. Novikov, D. E. Lacklison, L. C. Jenkins, D. Johnston, J. W. Orton, S. E. Hooper, N. Baba-Ali, T. L. Tansley, and V. V. Tret'yakov. The growth and properties of group III nitrides. *Journal of Crystal Growth*, 150(Part 2):892–896, May 1995.

[27] R. Felício Fuck and I. Tsvankin. Analysis of the symmetry of a stressed medium using nonlinear elasticity. *GEOPHYSICS*, 74(5):WB79–WB87, September 2009.

[28] Martin H. Sadd. *Elasticity: Theory, Applications, and Numerics*. Academic Press, 1 edition, September 2004.

[29] Gustav Gautschi. *Piezoelectric Sensorics*. Springer, 1st ed. 2002. corr. 2nd printing 2006 edition, September 2010.

[30] Aluminium nitride. alumstruc123.

[31] *Piezoelectric Materials: Structure, Properties and Applications (Materials Science and Technologies)*. Nova Science Pub Inc.

[32] Mark E. Brezinski. *Optical Coherence Tomography: Principles and Applications*. Academic Press, 1 edition, September 2006. matrix55.

[33] Jiashi Yang. *The Mechanics of Piezoelectric Structures*. World Scientific Publishing Company, March 2006.

[34] Humberto Campanella. *Acoustic Wave and Electromechanical Resonators: Concept to Key Applications (Integrated Microsystems)*. Artech House, January 2010. design13.

[35] Jan Tichý, Jirí Erhart, Erwin Kittinger, and Jana Prívratská. *Fundamentals of Piezoelectric Sensorics: Mechanical, Dielectric, and Thermodynamical Properties of Piezoelectric Materials.* Springer, 2010 edition, August 2010.

[36] R. Weigel, D. P. Morgan, J. M. Owens, A. Ballato, K. M. Lakin, K. Hashimoto, and C. C. W. Ruppel. Microwave acoustic materials, devices, and applications. *IEEE Transactions on Microwave Theory and Techniques*, 50(3):738–749, March 2002. acoustic3.

[37] John D. Anderson. *A History of Aerodynamics: And Its Impact on Flying Machines (Cambridge Aerospace Series).* Cambridge University Press, January 1999.

[38] David T. Blackstock. *Fundamentals of Physical Acoustics.* Wiley-Interscience, 1 edition, February 2000.

[39] Bhushan P. Bharat. *Fundamentals of Soil Dynamics and Earthquake Engineering.* PHI Learning, December 2009.

[40] Ting-Ta Yen, Chih-Ming Lin, Yun-Ju Lai, Damien Wittwer, Matthew A. Hopcroft, and Albert P. Pisano. Fine frequency selection techniques for aluminum nitride Lamb wave resonators. In *2010 IEEE International Frequency Control Symposium*, pages 9–13. IEEE, June 2010.

[41] Renyuan Wang, Sunil A. Bhave, and Kushal Bhattacharjee. High k¡inf¿t¡/inf¿¡sup¿2¡/sup¿&#x00D7;Q, multi-frequency lithium niobate resonators. In *2013 IEEE 26th International Conference on Micro Electro Mechanical Systems (MEMS)*, pages 165–168. IEEE, January 2013.

[42] Gianluca Piazza, Philip J. Stephanou, and Albert P. Pisano. Piezoelectric Aluminum Nitride Vibrating Contour-Mode MEMS Resonators. *Journal of Microelectromechanical Systems*, 15(6):1406–1418, December 2006. design2.

[43] Chih-Ming Lin, Yung-Yu Chen, Valery V. Felmetsger, Gabriele Vigevani, Debbie G. Senesky, and Albert P. Pisano. Micromachined aluminum nitride acoustic resonators with an epitaxial silicon carbide layer utilizing high-order Lamb wave modes. In *2012 IEEE 25th International Conference on Micro Electro Mechanical Systems (MEMS)*, pages 733–736. IEEE, January 2012.

[44] B. Antkowiak, J. P. Gorman, M. Varghese, D. J. D. Carter, and A. E. Duwel. Design of a high-Q, low-impedance, GHz-range piezoelectric mems resonator. In *TRANSDUCERS '03. 12th International Conference on Solid-State Sensors, Actuators and Microsystems. Digest of Technical Papers (Cat. No.03TH8664)*, pages 841–846. IEEE, 2003.

[45] Ting-Ta Yen, Chih-Ming Lin, Matthew A. Hopcroft, Jan H. Kuypers, Debbie G. Senesky, and Albert P. Pisano. Synthesis of narrowband AlN Lamb wave ladder-type filters based on overhang adjustment. In *2010 IEEE International Ultrasonics Symposium*, pages 970–973. IEEE, October 2010.

[46] Ventsislav Yantchev and Ilia Katardjiev. Thin film Lamb wave resonators in frequency control and sensing applications: a review. *Journal of Micromechanics and Microengineering*, 23(4):043001+, April 2013.

[47] Lori A. Callaghan. *Design, Fabrication, and Characterization of Beam - Supported Aluminum Nitride Thin Film Bulk Acoustic Resonators.* PhD thesis, UNIVERSITY OF CALIFORNIA Santa Barbara, September 2005.

[48] P. J. Stephanou and A. P. Pisano. PS-4 GHZ Contour Extensional Mode Aluminum Nitride MEMS Resonators. In *2006 IEEE Ultrasonics Symposium*, pages 2401–2404. IEEE, October 2006.

[49] David Morgan. *Surface Acoustic Wave Filters, Second Edition: With Applications to Electronic Communications and Signal Processing (Studies in Electrical and Electronic Engineering)*. Academic Press, 2 edition, August 2007. design12.

[50] Rao K. R. Yarlagadda. *Analog and Digital Signals and Systems*. Springer, 2010 edition, December 2009. apod5.

[51] A. Nagoor Kani. *Signals & Systems*. 1. McGraw-Hill Education, 1995. apod7.

[52] F. J. Harris. On the use of windows for harmonic analysis with the discrete Fourier transform. *Proceedings of the IEEE*, 66(1):51–83, January 1978. apod6.

[53] Ronald L. Allen and Duncan Mills. *Signal Analysis: Time, Frequency, Scale, and Structure*. Wiley-IEEE Press, 1 edition, January 2004. apod8.

[54] D. C. Malocha and C. D. Bishop. The Classical Truncated Cosine Series Functions with Applications to SAW Filters. *IEEE Transactions on Ultrasonics, Ferroelectrics and Frequency Control*, 34(1):75–85, January 1987. apod10.

[55] Steven W. Smith. *The Scientist & Engineer's Guide to Digital Signal Processing*. California Technical Pub, 1st edition, 1997.

[56] C. K. Campbell. Applications of surface acoustic and shallow bulk acoustic wave devices. *Proceedings of the IEEE*, 77(10):1453–1484, October 1989. apod4.

[57] A. R. Reddy. Design of SAW bandpass filters using new window functions. *IEEE Transactions on Ultrasonics, Ferroelectrics and Frequency Control*, 35(1):50–56, January 1988. apod3.

[58] H. Nakamura, T. Yamada, T. Igaki, K. Nishimura, T. Ishizaki, and K. Ogawa. A practical SPUDT design for SAW filters with different-width split-finger interdigital transducers. In *2000 IEEE Ultrasonics Symposium. Proceedings. An International Symposium (Cat. No.00CH37121)*, pages 105–108. IEEE, 2000. apod11.

[59] Colin Campbell. *Surface Acoustic Wave Devices and Their Signal Processing Applications*. Academic Pr. apod12.

[60] R. H. Tancrell and M. G. Holland. Acoustic surface wave filters. *Proceedings of the IEEE*, 59(3):393–409, 1971. apod14.

[61] Venkataramani. Digital Signal Processors. pages 16–18, 2011. apod16.

[62] Stanley Reisman, Arthur B. Ritter, Vikki Hazelwood, Bozena B. Michniak, Antonio Valdevit, and Alfred N. Ascione. *Biomedical Engineering Principles*. CRC Press, 1 edition, June 2005.

[63] D. Güttler, B. Abendroth, R. Grötzschel, W. Möller, and D. Depla. Mechanisms of target poisoning during magnetron sputtering as investigated by real-time in situ analysis and collisional computer simulation. *Applied Physics Letters*, 85(25):6134–6136, December 2004. targetpoison1.

[64] D. Depla, S. Heirwegh, S. Mahieu, and R. De Gryse. Towards a more complete model for reactive magnetron sputtering. *Journal of Physics D: Applied Physics*, 40(7):1957–1965, April 2007.

[65] C. E. Murray, I. C. Noyan, B. Lai, and Z. Cai. Strain effects in thin film/Si substrates revealed by X-ray microdiffraction. *Powder Diffraction*, 19:56–59, March 2004.

[66] Joseph C. Doll, Bryan C. Petzold, Biju Ninan, Ravi Mullapudi, and Beth L. Pruitt. Aluminum nitride on titanium for CMOS compatible piezoelectric transducers. *Journal of micromechanics and microengineering : structures, devices, and systems*, 20(2):25008–25015, 2010.

[67] T. van Hemert, D. Sarakiotis, S. Jose, R. J. E. Hueting, and J. Schmitz. Exploring capacitance-voltage measurements to find the piezoelectric coefficient of aluminum nitride. In *Microelectronic Test Structures (ICMTS), 2011 IEEE International Conference on*, pages 69–73. IEEE, April 2011.

[68] Ji Liang, Hongxiang Zhang, Daihua Zhang, Xuexin Duan, Hao Zhang, and Wei Pang. Design and fabrication of aluminum nitride Lamb wave resonators towards high figure of merit for intermediate frequency filter applications. *Journal of Micromechanics and Microengineering*, 25(3):035016, 2015. qfactor222.

[69] Chris Chapman. *Fundamentals of Seismic Wave Propagation*. Cambridge University Press, August 2004.

[70] *Advanced Piezoelectric Materials: Science and Technology (Woodhead Publishing Series in Electronic and Optical Materials)*. Woodhead Publishing, 1 edition, October 2010.

[71] A. Preumont. *Mechatronics: Dynamics of Electromechanical and Piezoelectric Systems (Solid Mechanics and Its Applications)*. Springer, 2006 edition, September 2006.